Report No. CDOT-DTD-R-2005-01

Final Report

EVALUATION OF THE FRP-RETROFITTED ARCHES IN THE CASTLEWOOD CANYON BRIDGE

Delchi Fafach and Benson Shing

Sunyoung Chang and Yunping Xi

December 2004

COLORADO DEPARTMENT OF TRANSPORTATION

RESEARCH BRANCH

The contents of this report reflect the views of the authors, who are responsible for the facts and accuracy of the data presented herein. The contents do not necessarily reflect the official views of the Colorado Department of Transportation or the Federal Highway Administration. This report does not constitute a standard, specification, or regulation.

Technical Report Documentation Page

1. Report No. CDOT-DTD-R-2005-01	2. Government Accession No.	3. Recipient's Catalog No.
4. Title and Subtitle EVALUATION OF THE FRP-RETROFITTED ARCHES IN THE CASTLEWOOD CANYON BRIDGE		5. Report Date December 2004 6. Performing Organization Code
7. Author(s) Delchi Fafach and Benson Shing; Sunyoung Chang, and Yunping Xi		8. Performing Organization Report No. CDOT-DTD-R-2005-01
9. Performing Organization Name and Address University of Colorado – Boulder Campus Box 561 Boulder, CO 80309		10. Work Unit No. (TRAIS) 11. Contract or Grant No. 87.50
12. Sponsoring Agency Name and Address Colorado Department of Transportation - Research 4201 E. Arkansas Ave. Denver, CO 80222		13. Type of Report and Period Covered 14. Sponsoring Agency Code

15. Supplementary Notes
Prepared in cooperation with the U.S. Department of Transportation, Federal Highway Administration

16. Abstract

Fiber-reinforced composites are increasingly being used for repair of deteriorating and understrength concrete decks and columns due to their excellent properties. Carbon fiber-reinforced polymers (CFRP) sheets were used in this project to strengthen the arch. Four quarter-scale beams were tested to model the arch ribs before and after the retrofit to evaluate the strength of the arches. Two of the beams were designed to model the behavior of an arch rib below a heavily loaded column. The remaining two beams were designed to model the moment connection at the base of an arch. The test results were used to calibrate an analysis technique which was used to predict the strength of the full-scale arches. The retrofitted test specimens were between 22% and 30% stronger in bending than the control specimens. However, the strengthening scheme did not increase the strength of the retrofitted specimens as much as expected. The externally bonded FRP ruptured earlier than expected in one test specimen. Another specimen experienced peeling of the concrete which led to bond failure of the FRP rods.

Durability of bond between CFRP and concrete was studied by the pull-off bond strength test after various long-term conditioning, including room temperature, wetting in water, wetting/drying in water, immersion in 3% NaCl, freeze-thaw, immersion in 0.2N NaOH, and high temperature. The experimental results indicate that the bond strengths satisfy the selected acceptance criterion, although the bond strengths were significantly affected by the long-term environmental exposures. However, the bond failure modes were unsatisfactory based on the ACI criterion in that the ideal failure mode is to have 100% failure in substrate.

A wireless real-time remote bridge monitoring system was installed on the bridge site to evaluate the performance of the arch and the effectiveness of the corrosion inhibitor applied in the arch rib. The maximum strain recorded was 1400 με (0.14 %) under the service conditions, which is about 23 % of the minimum ultimate rupture strain. The chloride content and the corrosion potential in the new shotcrete cover have been increased, which are due to the re-distribution of the existing chloride in the old concrete.

Implementation:
The axial forces in the arches may limit the strength increase due to the longitudinal FRP. The transverse FRP increases both the strength and the ductility of the arches. The effects of concrete peeling must be considered at the arch-foundation moment connections, especially because of the CFRP dowel development at these locations.

The degradation in the pull-off strength must be considered in the specifications related to the structural design if the FRPs are to be used for repair. The monitoring results obtained so far provide valuable information. The monitoring process of the arch in the bridge should be continued, which will be very important for evaluating the effectiveness of carbon FRP repairing, the performance of the corrosion inhibitor, and long-term performance of the strengthened arch ribs.

17. Keywords	18. Distribution Statement
durability, CFRPs, pull-off strength, structure monitoring	No restrictions. This document is available to the public through the National Technical Information Service, Springfield, VA 22161

19. Security Classif. (of this report)	20. Security Classif. (of this page)	21. No. of Pages	22. Price
Unclassified	Unclassified	249	

Form DOT F 1700.7 (8-72) Reproduction of completed page authorized

EVALUATION OF THE FRP-RETROFITTED ARCHES IN THE CASTLEWOOD CANYON BRIDGE

by

Delchi Fafach and Benson Shing

Sunyoung Chang and Yunping Xi

University of Colorado at Boulder

Report No. CDOT-DTD-R-2005-01

Final Report

Prepared for

The Colorado Department of Transportation

Research Branch

December 2004

Colorado Department of Transportation

Research Branch

4201 E. Arkansas Ave.

Denver, CO 80222

(303) 757-9506

Acknowledgements

This study was sponsored by the Federal Highway Administration (FHWA) and conducted in conjunction with the Colorado Department of Transportation (CDOT) as part of FHWA's Innovative Bridge Research and Construction Program. The project was monitored by Matthew Greer of the Colorado Division of FHWA and administered by Ahmad Ardani of the Research Branch of CDOT.

Mike Mohseni and Trevor Wang of CDOT were the engineers for the Castlewood Canyon Bridge. Their technical assistance with the design of the test specimens is gratefully acknowledged.

The continued technical support of Pete Milligan of Fyfe Co., who designed the Fibrwrap plans for the Castlewood Canyon Bridge, was very helpful. The writers also wish to thank Rick Wheeler of Lafarge, who generously donated time and materials for the beam specimens.

The writers appreciate the invaluable assistance of Thomas L. Bowen, manager of the Structures and Materials Testing Laboratory of the University of Colorado, and the laboratory assistants, Chris Cloutier, David Shaw, Dan Caughlin, Chris Baksa, and Steve Cole in the experimental work. The writers would also like to thank Professor Enrico Spacone for the use of his reinforced concrete axial/bending analysis program and Research Associate Holger Basche for his continuous help throughout the entire project, especially in the preparation of the report.

The writers would like to express their thanks to the Colorado DOT for continuous support and encouragement throughout this study, and specifically to Ahmad Ardani and Richard Griffin of CDOT Research Branch; Trever Wang, Ali Haraj, and Michael McMullen of CDOT Staff Bridge; Greg Lowery of CDOT Staff Materials; and Matt Greer of FHWA for their valuable suggestions and inputs. The writers would also like to express their thanks to Ms. Lindsay Marshall for careful editing of the report.

Opinions expressed in this report are those of the writers and do not necessarily represent those of CDOT or FHWA .

Executive Summary

Under the Innovative Bridge Research and Construction (IBRC) program of the Federal Highway Administration (FHWA), the Colorado Department of Transportation (CDOT) has used a combination of carbon fiber-reinforced polymer (CFRP) bars and externally bonded CFRP fabric to strengthen the arch bridge in Castlewood Canyon State Park. The original bridge was in poor condition and required repair and strengthening to meet increased traffic loads due to widened lanes. During the summer of 2003, the bridge arches were repaired and strengthened. An innovative FRP scheme provides longitudinal reinforcement for flexural enhancement and transverse reinforcement for confinement, shear enhancement, and protection against concrete deterioration and steel corrosion.

The performance of FRP strengthening work was evaluated from several aspects. First, we evaluated the strength of the arch ribs in the Castlewood Canyon Bridge. For this purpose, four quarter-scale beams were tested to model the arch ribs before and after the retrofit. The test results were used to calibrate a theoretical analysis model which was then used to evaluate the strength of the arch ribs.

The retrofitted test specimens were between 22% and 30% stronger in bending than the control specimens. However, the strengthening scheme did not increase the strength of the retrofitted specimens as much as expected. The externally bonded FRP ruptured earlier than expected in one test specimen. The other retrofitted specimen experienced peeling of the concrete which led to bond failure of the FRP rods. This indicates that the bond between CFRP and substrate is a critical factor in order to increase load carrying capacity of structures and effectiveness of strengthening systems.

While the test specimens failed in tension, a load analysis of the arch ribs indicates that the arch strengths are governed by crushing of the concrete in compression. The test results were used to calibrate an analysis model that was in turn used to compute axial load-moment strength interaction diagrams for the arch ribs. However, further tests could be conducted on similar

specimens under varied axial load-bending moment ratios in order to investigate more points along the strength interaction diagrams.

A long-term durability of bond strength between CFRP sheets and concrete/shotcrete under various accelerated environment conditions was performed. The effect of corrosion inhibitor on the bond strength was also evaluated. The bond strength was evaluated as a measure of pull-off strength. Seven accelerated environmental parameters were utilized in this study: room temperature, freeze-thaw cycles, wetting in water, wetting/drying cycles in water, deicing chemicals, sodium hydroxide, and high temperature.

Pull-off strengths of CFRP sheet-to-concrete/shotcrete after being exposed to the environmental parameters were satisfactory based on the selected acceptance criterion. Therefore, good protection against aggressive environmental conditions can be provided by the CFRP wrapping repair method. However, the bond failure modes were unsatisfactory based on the ACI criterion in that the ideal failure mode is to have 100% failure in substrate.

In case of a fire, the bond strength may significantly decrease because the epoxy starts to decompose at a temperature of 446 ^{o}F. For the application of CFRP sheets in concrete structures the maximum useable temperature should be below 446 ^{o}F. Above that temperature, special surface treatments or additives should be applied to the FRP sheets to enhance their fire endurance.

In order to monitor the performance of the repaired bridge, a wireless remote structural monitoring system was installed on the bridge. The strains in the surface of the arch and five other corrosion related parameters were monitored using the wireless technology. The maximum strain was recorded up to 1400 με (0.14 %) under the service conditions. The overall variation of the strain gages in the arch indicated that the temperature variation currently governs the internal strain distribution of the arch. According to the design specification, the 0.14 % of the maximum strain reached 23 % of the minimum ultimate rupture strain. An increase of the chloride content was observed in the new shotcrete cover. It is not due to the penetration of chloride from outside

of the cover; because the C-FRP wrapping and the shotcrete are brand new, it will take some time for the chloride to penetrate into the concrete. The increase of the chloride concentration may be due to the re-distribution of the internal chloride in existing concrete. Since the internal chloride concentration of existing concrete is higher than that of the new shotcrete, the chloride will diffuse from the existing concrete to the new shotcrete, which makes the chloride level increase.

Implementation Statement

The axial forces in the arches may limit the strength increase due to the longitudinal FRP. The transverse FRP increases both the strength and the ductility of the arches. The effects of concrete peeling must be considered at the arch-foundation moment connections, especially because of the CFRP dowel development at these locations.

The degradation in the pull-off strength must be considered in the specifications related to the structural design if the FRPs are to be used for repair. The monitoring results obtained so far provide valuable information. The monitoring process of the arch in the bridge should be continued, which will be very important for evaluating the effectiveness of carbon FRP repairing, the performance of the corrosion inhibitor, and long-term performance of the strengthened arch ribs.

Table of Contents

List of Figures

List of Tables

CHAPTER 1. STRENGTH EVALUATION OF THE ARCH RIBS

1.1 Introduction

1.1.1 Background

The use of fiber-reinforced polymers (FRPs) in reinforced concrete (RC) bridge construction has dramatically increased since the early 1990's. FRPs are non-corrosive, lightweight, non-conductive, and very strong in tension. The corrosive resistance is important in bridges, where traditional steel reinforcement tends to deteriorate under exposure to moisture and to roadway deicing salts. Thus, the use of FRPs may significantly increase the lifespan of bridges.

Many innovative FRP applications have been developed and tested for use in new bridges and in existing bridge repair and strengthening. Carbon FRP (CFRP) tendons and rods have been used in various prestressed concrete members (Grace et al., 2004; Zylstra et al., 2001). Externally bonded FRP plates and fabrics have been used to increase the flexural and shear strengths of beams. Externally bonded FRP shells and fabrics have been used to increase the strength and ductility of columns, especially in seismic regions. FRP rods have been used similarly to conventional reinforcement in many bridge decks. Research into the use of FRPs in bridges is currently taking place all over the world. Banther et al., (2002) have investigated the use of sprayed FRP in Canada and the U.S. military (Ray et al., 2001) have studied the rapid installation of FRP plates by nailing them into concrete. An overview of early bridges constructed using FRPs is given by Magdi et al., (1993). A recent overview and state-of-the-art summary of the use of FRP in bridges worldwide is given by Keller (2003).

The bulk of literature on the behavior of FRP reinforced concrete is scattered throughout journals and conference proceedings. However, published resources are becoming available to aid engineers in design. An early example of this is the ACI 440R-96 report, which provides comprehensive information on FRP materials, design guidelines, and applications.

More recently, Teng et al., (2002) have provided a comprehensive overview of structural design issues related to FRP strengthened RC members.

1.2.1 Two examples of FRPs in bridge strengthening and repair

1.2.1.1 Field test of Bridge J-857 (Alkhrdaji et al. 1999)

Bridge J-857 along Route 72 in Phelps County, MO was field tested to destruction after having been strengthened with FRP composite systems.

The original bridge, built during the 1930's, consisted of three simply supported solid RC decks. Each deck was 18" deep by 25' wide and spanned 26' over a shallow, rocky creek bed. The decks were reinforced with No. 8 rebars at 5" on center in the longitudinal direction and No. 4 rebars at 18" in the transverse direction.

Two of the three decks were strengthened with FRP reinforcement. Two different FRP systems were used: externally bonded CFRP sheets and near-surface mounted (NSM) CFRP rods. The design goal was a strength increase of 30% due to the FRP. The externally bonded sheet system consisted of eight, 20"-wide, single-ply CFRP strips applied to the deck soffit with epoxy. The strips were evenly spaced and ran the length of the soffit in the longitudinal direction. The second system consisted of 20 NSM CFRP rods spaced at 15" on center. The rods were embedded with epoxy into 0.75" deep grooves cut into the bridge deck soffit in the longitudinal direction. Strain gages and fiber optic sensors were applied to the concrete, steel, and FRP to monitor the strains during testing.

The bridge was first tested under the weight of a moving vehicle. The individual decks were then tested to failure using hydraulic jacks. The control deck failed at 462 kips in a typical under-reinforced fashion (yielding of the steel reinforcement followed by crushing of the concrete beyond the ultimate moment capacity). The deck with NSM rods failed at 596 kips by rupture of the rods at the location of the widest crack. The deck with CFRP sheets failed at 543 kips by a combination of rupture and peeling (debonding) of the sheets.

The decks with FRP were stiffer than the control deck. However, the control deck exhibited the most ductility.

The authors concluded that the test results clearly indicated the successful performance of both FRP strengthening systems. However, the externally bonded FRP and NSM rod systems led to a 17% and 27% strength increase, respectively, which were less than the originally predicted values. This was due, at least in part, to the concrete and steel strengths being higher than originally assumed.

1.2.1.2 Retrofit of Bridge CLI-380-0032 (Shahrooz and Boy 2004)

Bridge CLI-380-0032 was retrofitted with multiple FRP systems and load tested for the Ohio Department of Transportation (ODOT). The structural performance was subsequently monitored for one year.

The original RC bridge, constructed in 1955, consisted of three decks with spans between 22' and 28'. The bridge was in good condition with only minor cracking. It was posted because of insufficient capacity of the slab.

Four different CFRP strengthening systems were incorporated in different part of the deck spans to compare their constructability and performance. The systems included: (1) bonded 2.86" wide by 0.052" thick plates spaced at 12" on center; (2) bonded 5" wide by 0.075" thick plates at 18" on center; (3) one layer of 12" wide fabric at 12" on center; and (4) 4" wide by 0.19" thick plates spaced at 12" on center. Systems 1, 2, and 3 were composed of unidirectional fibers while system 4 had unidirectional carbon fibers and E-glass fibers at ± 45 degrees. All FRP was applied on the soffit of the deck.

The bridge was instrumented and tested before retrofitting, shortly after retrofitting, and after one year of service. Two 30-kip loaded dump trucks in various critical configurations were used for testing. Furthermore, a 3-D finite element model was built to model the bridge. After strengthening, the rated bridge strength was increased by 22%. The test results

indicated that this was conservative compared to the actual strength increase of the structure. On the other hand, the FRP added little to the stiffness of the deck. Finally, no loss of performance was detected after one year of service. The authors concluded that the FRP strengthening systems were feasible due both to their simplicity and their effectiveness.

These examples, as well as many other bridge projects and experimental tests, demonstrate the feasibility of using externally bonded FRP and NSM FRP rods in the repair and strengthening of bridge members.

1.3.1 Project overview

Under the Innovative Bridge Research and Construction (IBRC) program of the Federal Highway Administration (FHWA), the Colorado Department of Transportation (CDOT) has used a combination of CFRP bars and externally bonded fabric to strengthen the arch bridge in Castlewood Canyon State Park. The original bridge, built in 1946, was in poor condition and required both repair and strengthening to meet increased traffic loads due to widened lanes. During the summer of 2003, the bridge arches were repaired and strengthened. An innovative FRP scheme provided longitudinal reinforcement for flexural enhancement and transverse reinforcement for confinement, shear enhancement, and protection against concrete deterioration and steel corrosion. After the arches were strengthened, the spandrel columns and bridge decks were replaced in a manner that minimized unbalanced loads on the arches.

The Castlewood Canyon Bridge is apparently the first arch bridge to have been retrofitted with FRP reinforcement. The primary objective of this project is to demonstrate the feasibility of using FRP composites to strengthen and protect the arch structure. Research was conducted to support the construction work. The research consisted of seven tasks: (1) quality assurance tests of FRP materials; (2) quality assurance tests of bond strength; (3) durability tests on bonding; (4) on-site corrosion monitoring of the bridge materials; (5) analysis of the arch structure; (6) structural testing of scaled RC specimens to model the arches before and after retrofit; and (7) field observation of the construction. Tasks 1 and 2

were the responsibility of the contractor. The remaining tasks were performed by faculty and students of the University of Colorado at Boulder.

1.4.1 Objectives and scope

This chapter summarizes the strength analyses of the structure and the testing of four RC beam specimens to failure. Two retrofit schemes were evaluated. One scheme was used for the arches and the other was used to strengthen the moment connections at the arch bases. The beams which modeled a typical arch section were 19" wide by 11" deep by 16'-0" long. The beams which modeled the arch-foundation connection scheme had cross sections of 19" wide by 18.5" deep and were 16'-0" long.

Two of the beams were control beams without FRP strengthening and two were strengthened with FRP. Of the two beams that were strengthened with FRP, one was wrapped with a scheme similar to that used around the spandrel column-arch rib connections. The other was wrapped and reinforced with a scheme similar to that used in the arch-foundation connections, using both external FRP wraps and internal FRP rods.

The beams were designed and loaded to model the arches as closely as possible at one quarter scale. The steel and concrete used in the test specimens was as close as possible to the existing materials in the original bridge. The same FRP materials that were used in the bridge were used in the test beams. The wet lay-up application of the FRP fabric for the specimens was performed by the same contractor who performed the work on the actual bridge.

1.5.1 Organization of Chapter 1

Section 1.2 gives a detailed description of the bridge and its deteriorated condition. The repair and strengthening scheme is then described and the nominal properties of the materials in the bridge are presented.

Section 1.3 explains the analysis procedures used to predict the responses of the specimens and the actual bridge arches. A method for predicting the theoretical moment-curvature response and ultimate strength of a general FRP-reinforced RC section under a combination of axial load and bending moment is presented.

Section 1.4 presents the detailed test specimen designs and the reasons why these designs were chosen. First, the initial strength and load analyses of the bridge structure are summarized. Next, the challenges encountered in the specimen design process are explained and reasons are given for the modeling schemes chosen. The as-built specimen drawings are presented, and the predicted strength and moment-curvature results for the specimens are presented and discussed.

Section 1.5 describes the experimental program. The specimen fabrication is recorded in detail. The tested properties of the materials used in the specimens are presented. The setup, procedure, and instrumentation for each test are described.

Section 1.6 contains a record of the observations, events, and data from each test.

Section 1.7 presents an analysis and interpretation of the test results. Moment-curvature responses are computed from the test data. The strengths and stiffness of the specimens are compared. The theoretical model, presented in Section 1.3, is calibrated from the test data. The behavior of the test specimens is used to predict the strengths of the actual bridge arch sections.

Section 1.8 contains a summary of the tests, results, and conclusions.

Appendix A presents the construction documents describing the externally bonded FRP wrapping scheme.

Appendix B presents detailed analysis of the test specimens.

Appendix C presents detailed analysis of the arch ribs and arch-foundation connections.

Appendix D presents the test strain data which is not included in Section 1.6.

1.2 Bridge Overview

1.2.1 Original design

The bridge is located along Highway 83 at the edge of Castlewood Canyon State Park in the Black Forest of central Colorado. The park is a historical area and the bridge is considered a historical landmark. The original two-lane reinforced concrete arch bridge, built in 1946, is shown in Figure 1-1. The arches are 6'-4" wide by 5'-10" deep at the base with the depth tapering down to 3'-4" at the highest point. The arch geometry is shown in Figure 1-2.

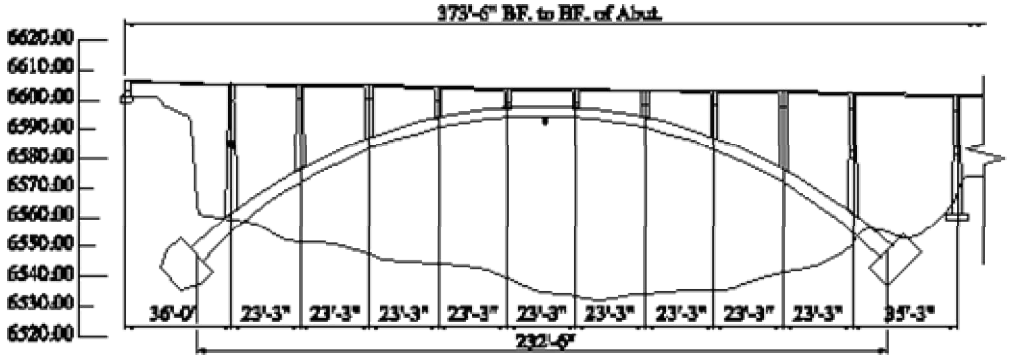

Figure 1-1 Profile of original bridge

In 2003, the bridge was severely dilapidated and in need of repair, enlarging, and strengthening. Parts of the soft concrete had spalled off the deck, columns, and arches, and the rebars were badly rusted. (See Figure 1-3 and Figure 1-4.) During the summer of 2003, the original arch was repaired, the spandrel columns were replaced, the bridge deck was replaced and widened from about 35' to 43'-0" including railings, and the overall length was increased from 373'-6" to 404'-5".

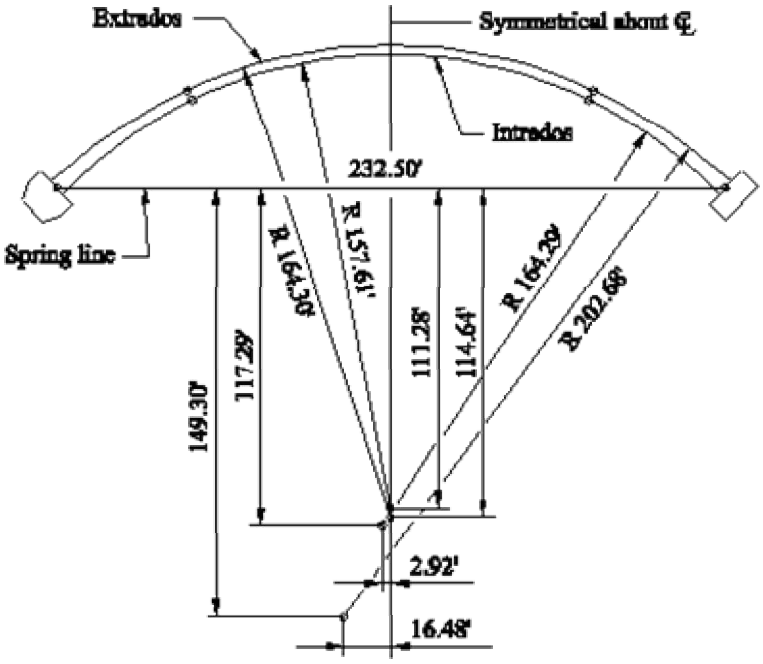

Figure 1-2 Arch geometry

Figure 1-3 Spalling concrete and exposed steel before repair

Figure 1-4 Spalling concrete and exposed steel during construction

1.2.2 Repair and strengthening

1.2.2.1 General

The arches were repaired and strengthened with Fibrwrap, an FRP product manufactured by Fyfe. The work on the arches included eight steps:

1) Loose materials and debris were removed from the surfaces and from around the reinforcing.
2) Exposed reinforcing bars were sandblasted clean from rust.
3) Penetrating corrosion inhibitor was applied to surface of concrete arches and struts to address hidden damage.
4) Leadline CFRP rods manufactured by Mitsubishi were anchored into the footings with epoxy around the bases of the arches to strengthen the arch-foundation connection.

5) The surfaces of the arches were finished to the original surfaces using hand and machine applied mortar. Cracks were sealed using epoxy injection.
6) New pedestals were constructed for new spandrel columns.
7) Fibrwrap, an externally bonded CFRP, was applied to arch ribs to confine concrete and to reinforce and strengthen the arch.
8) The arches were then painted to appear like concrete.

After the arch had been repaired and strengthened, new spandrel column were placed adjacent to the old columns and the original deck was replaced with precast panels. This replacement procedure began at the center of the arch and progressed outward symmetrically to minimize unbalanced loads in the arches. Much care was taken throughout the course of the construction to minimize the impact on the surrounding canyon environment. Figure 1-5 shows the arches during the repair process. Figure 1-6 shows the application of the longitudinal Fibrwrap. Figure 1-7 shows the completed bridge. Figure 1-8 shows the placement of the precast deck panels.

Figure 1-5 Arches during construction

Figure 1-6 Applying Fibrwrap to arch Extrados

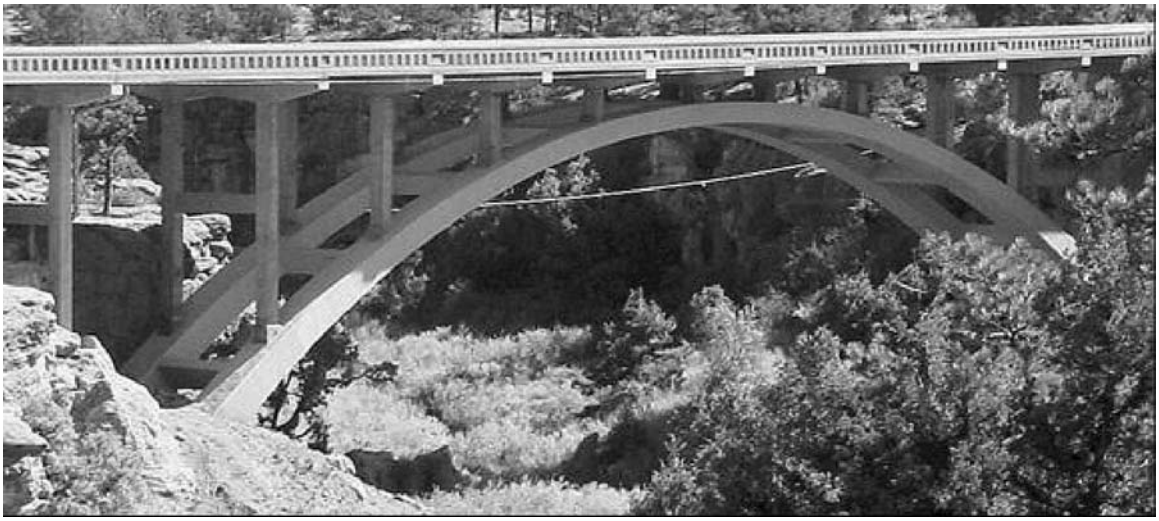

Figure 1-7 Completed bridge

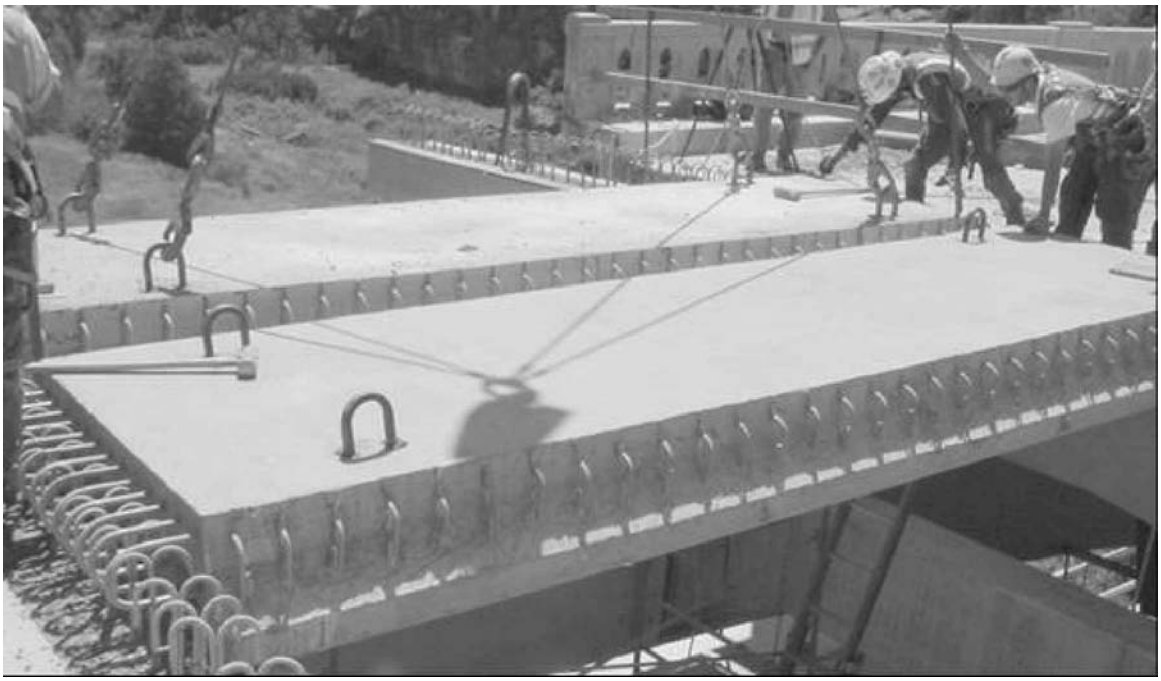

Figure 1-8 Precast deck panels

1.2.2.2 Arch construction

The reinforcing in the original arches is shown in Figure 1-9. The section height varied along the arch, but the amount of longitudinal reinforcing remained constant. The dowels shown in Section A-A were only at the arch-foundation connection.

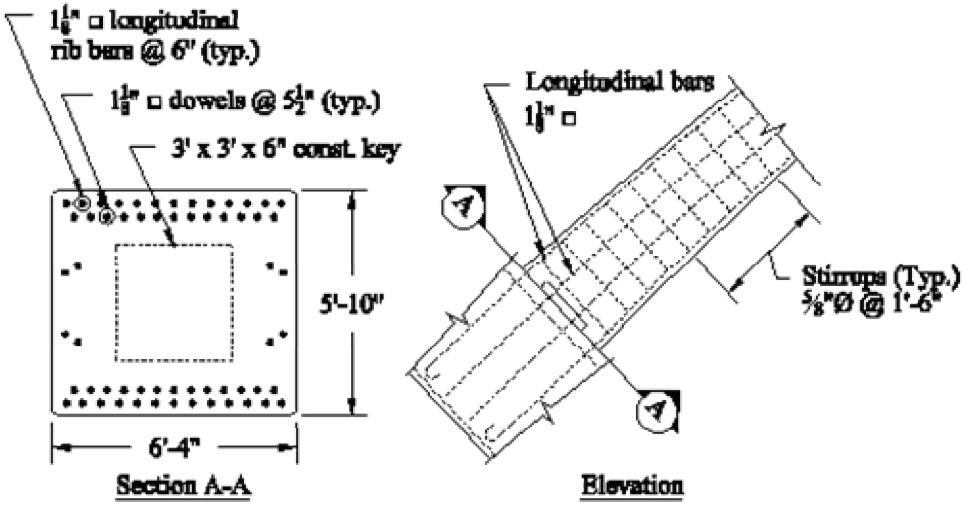

Figure 1-9 Construction details at the base of the arch.

In the new design, the base of the arch was expected to take a large negative moment. During the retrofit process, the loose concrete at the base was removed to expose the outer layer of steel bars. Holes were drilled at 6" all around the perimeter of the arches into the footing where pairs of 9.5-mm Leadline dowels were set with epoxy, as shown in Figure 1-10. A layer of concrete patch was applied to provide cover and bonding for the Leadline dowels. Fibrwrap was then applied in the longitudinal orientation with more Fibrwrap placed on the extrados than the intrados because of the large negative moment expected at the base. The longitudinal Fibrwrap on the rest of the arch was more symmetrically placed on the extrados and intrados. See Appendix A for design drawings for the placement of the Fibrwrap. The base of the arch was then wrapped with a 4'-0" wide layer of transverse Fibrwrap and the rest of the arch was wrapped with alternating transverse 1'-0" wide full and C-shaped bands providing confinement, shear reinforcement, and moisture protection.

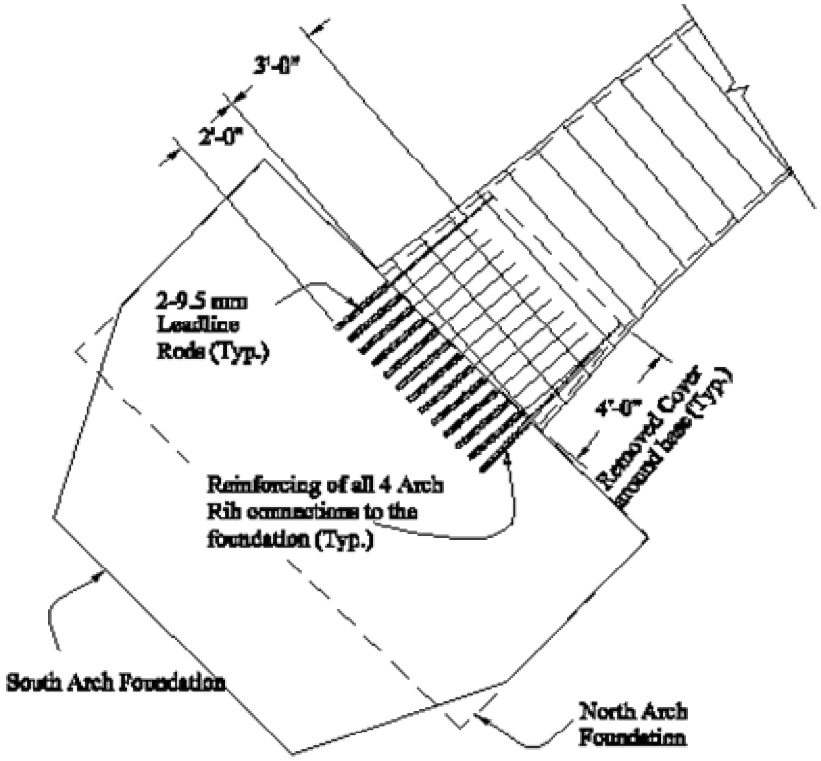

Figure 1-10 FRP dowel installation in arch-foundation connection

1.2.3 Materials

The nominal strengths and stiffness of the materials for the analysis of the new arches are shown in Table 1-1. The strength of the intact existing concrete was determined from tests of core samples. The yield strength of the existing steel was specified in the construction documents for the original bridge. The material properties of the Leadline and Fibrwrap were supplied by the manufacturers. The strength of the shotcrete was specified in the construction documents for the repair and strengthening.

Table 1-1 Material properties

Material	Yield Strength (*ksi*)	Ultimate Strength (*ksi*)	Modulus of Elasticity (*ksi*)
existing concrete	NA	2.5	unknown
existing steel	33	unknown	29,000
shotcrete	NA	4.0	unknown
Leadline	NA	409	21,320
Fibrwrap	NA	127	10,500

1.3 Strength Analysis of Rectangular Reinforced Concrete Sections with FRP

This section presents an analysis procedure for rectangular RC sections subjected to simultaneous axial compression and bending (hereafter referred to as beam-columns), which are commonly encountered in arch structures. The method presented here was used in this project to evaluate the ultimate strength and moment-curvature response of the Castlewood Canyon Bridge arches and test specimens.

1.3.1 Fundamental assumptions

The analysis procedures presented in this Section are based on the following fundamental assumptions:

1. plane sections remain plane during bending;
2. the tensile strength of concrete can be neglected;
3. perfect strain compatibility between concrete and reinforcing materials

1.3.2 Concrete material behavior

Many constitutive models have been proposed for the uniaxial compressive stress-strain relation of concrete. Three models were used for the analysis presented in this report. Kent and Park (1975) proposed a model which accounts for the effects of confinement due to transverse steel reinforcing by increasing the ultimate concrete strain (ε_{cu}). However, this model does not include the effects of confinement on the ultimate strength of the concrete (f'_c). Mander et al. (1988) proposed a model that includes the effects of confinement due to transverse steel reinforcing on the ultimate strength and ultimate ductility. They also proposed an energy balance equation to determine ε_{cu}, which is considered as the axial strain level at which the transverse steel will rupture due to lateral expansion in a concentrically loaded column. This model has gained wide acceptance since it was first proposed. Lam and Teng (2003) proposed a model for concrete uniformly confined with

transverse FRP reinforcement based on a large body of new and existing test data. They subsequently proposed a method for applying the model to concrete in rectangular columns. In this project, all three models were used and adjusted as explained below for application to eccentrically loaded columns. The tensile strength of concrete was considered to be zero.

1.3.2.1 Stress-strain relation developed by Kent and Park

The compressive stress-strain relation proposed by Kent and Park was applied only to unconfined concrete in this project. This relation is shown in Figure 1-11.

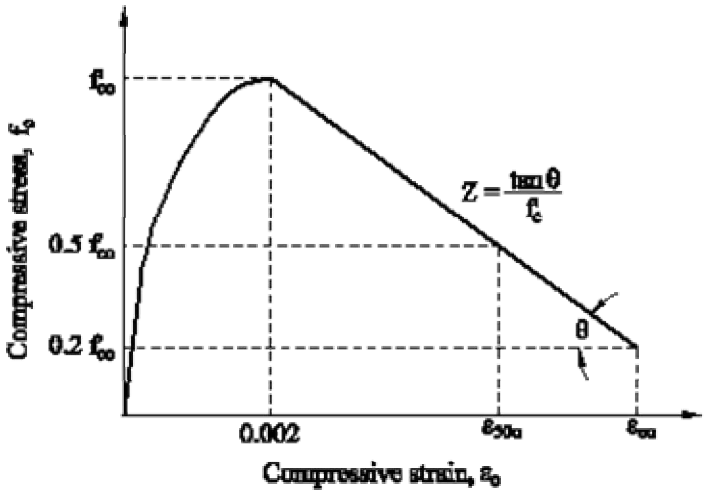

Figure 1-11 Kent and Park concrete stress-strain curve for unconfined concrete

It should be pointed out that the compressive strain is considered positive in the following equations. The proposed stress-strain relation is governed by the following equations:

In the region where $0 \le \varepsilon_c \le 0.002$,

$$f_c = f'_{co}\left[\frac{2\varepsilon_c}{0.002} - \left(\frac{\varepsilon_c}{0.002}\right)^2\right] \tag{1.1}$$

where f_c is the compressive stress at the strain ε_c and f'_{co} is the strength of the unconfined concrete.

In the region where $0.002 \le \varepsilon_c \le \varepsilon_{cu}$,

$$f_c = f'_{co}\left[1 - Z(\varepsilon_c - 0.002)\right] \tag{1.2}$$

where

$$Z = \frac{0.5}{\varepsilon_{50u} - 0.002} \tag{1.3}$$

$$\varepsilon_{50u} = \frac{3 + 0.002 f'_c}{f'_c - 1000} \tag{1.4}$$

In the region where $\varepsilon_c \ge \varepsilon_{cu}$, $f_c = 0$,

ε_{cu} can be solved from Equation (1.2) as

$$\varepsilon_{cu} = \frac{0.8}{Z} + 0.002\,. \tag{1.5}$$

1.3.2.2 Stress-strain relation developed by Mander et al.

The basic stress-strain relation for confined concrete proposed by Mander et al. (see Figure 1-12) is applicable to both circular and rectangular steel transverse reinforcement. In Figure 1-12, the Kent and Park graph for unconfined concrete has been superimposed to help visualize the confinement effects. The relation is governed by the following equations.

$$f_c = \frac{f'_{cc}\, xr}{r - 1 + x^r} \tag{1.6}$$

where f'_{cc} is the compressive strength of the confined concrete, and

$$x = \frac{\varepsilon_c}{\varepsilon_{cc}} \tag{1.7}$$

in which ε_{cc} is the strain corresponding to the ultimate stress f'_{cc}.

$$\varepsilon_{cc} = 0.002\left[1 + 5\left(\frac{f'_{cc}}{f'_{co}} - 1\right)\right] \tag{1.8}$$

Finally,

$$r = \frac{E_c}{E_c - E_{\sec}} \tag{1.9}$$

in which E_c can be computed for normal-weight concrete according to the ACI code (2002) as

$$E_c = 57{,}000\sqrt{f'_{co}} \tag{1.10}$$

In the above equations, f'_{co} is the compressive strength of unconfined concrete expressed in psi, and

$$E_{\sec} = \frac{f'_{cc}}{\varepsilon_{cc}} \tag{1.11}$$

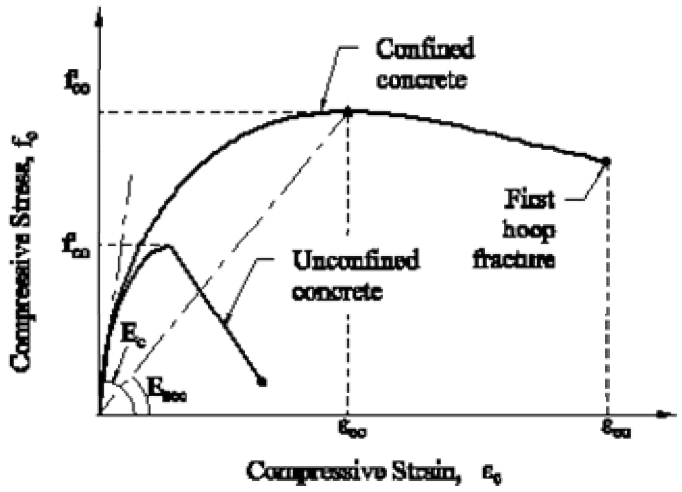

Figure 1-12 Mander et al.'s model for concrete confined by steel transverse reinforcement

In a rectangular section, only a portion of the volume of concrete within the core is effectively confined. The cross section of a rectangular column with steel hoops is shown in Figure 1-13, where the z-coordinate is parallel to the longitudinal axis of the column. The shaded area is the concrete that is assumed to have spalled and lost strength at high strains. The confinement effectiveness coefficient, k_e, can be defined based on the geometry of the transverse reinforcement as the ratio of the cross-sectional area of effectively confined concrete, A_e, to the total cross-sectional area of the concrete in the confined core, A_{cc}.

$$k_e = \frac{A_e}{A_{cc}} \tag{1.12}$$

$$A_{cc} = A_c - A_{sc} \tag{1.13}$$

in which A_c is the total area of the confined core, measured to the centerline of the transverse reinforcement, and A_{sc} is the area of the longitudinal reinforcement within the core. The difference between A_c and A_{sc} is due to two effects: spalling between the confined longitudinal bars and spalling between the transverse hoops.

Spalling between the confined longitudinal bars can be seen in Figure 1-13(a). Within rectangular hoops, the lateral stresses arch between the corners of the hoops or the ends of the ties. Mander described the border of the confined area using quadratic parabolas with 45^o tangents at either end. The maximum height of such a curve is $w_i/4$ and the area under the curve is . The portion of A_c which is not within these parabolas is A_i, where

$$A_i = \sum_{i=1}^{n} \frac{(w_i)^2}{6} \tag{1.14}$$

in which n is the number of parabolic spalled areas and w_i is the distance between confined longitudinal bars. In Figure 1-13, $n = 6$.

The second reduction in A_c is due to spalling between adjacent hoops. This effect is shown in Figure 1-13(b), and applies to circular as well as rectangular sections. The arching between the hoops follows is contained by parabolic curve similar to those described above. The parabolas extend into the core a distance of $s'_s/4$, where s'_s is the clear distance between the hoops. This results in the spalled offset shown in Figure 1-13(a). For simplicity, Mander et al. propose accounting for this further reduction in A_e using the factor $(1 - s'_s/2b_c)(1 - s'_s/2h_c)$. Thus, A_e is given by

$$A_e = (b_c h_c - A_i)\left(1 - \frac{s'_s}{2b_c}\right)\left(1 - \frac{s'_s}{2h_c}\right) \tag{1.15}$$

Unfortunately, the use of the factor $(1 - s'_s/2b_c)(1 - s'_s/2h_c)$ to account for the spalling between the hoops may only be appropriate to concentrically loaded columns. In a section

subjected to a bending moment, the neutral axis may be within the hoops but still outside of the effectively confined core if the hoops are spaced far enough apart. Thus, when descritizing the beam-column section for analysis for this project, the region within a distance $s'_s/4$ inside the centerline of the hoops was considered unconfined, and A_e for the interior region was defined as

$$A_e = \left(b_c h_c - A_i\right) \tag{1.16}$$

Equation (1.16) is identical to Equation (1.15) without the last two factors in parentheses.

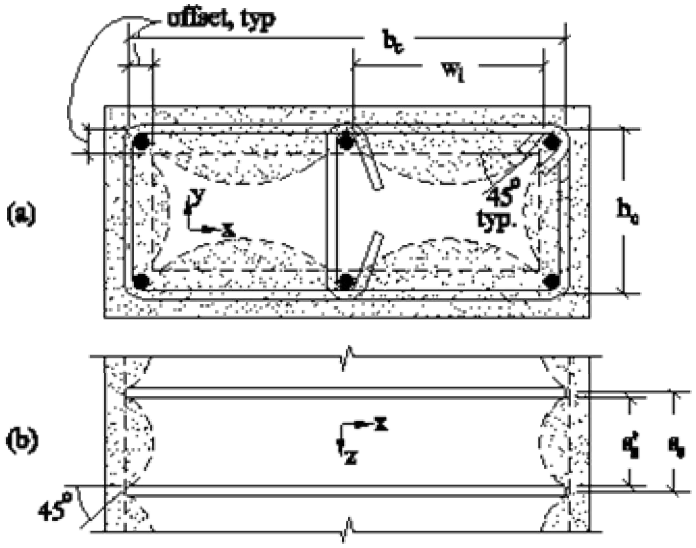

Figure 1-13 Effectively confined core for rectangular hoop reinforcement: (a) cross section; (b) longitudinal section

The increase in the strength and ductility of the concrete is due to the presence of lateral confining stresses in the x and y directions (f_{lx} and f_{ly}, respectively).

$$f_{lx} = \frac{A_{sx}}{s_s h_c} f_{yh} \tag{1.17}$$

$$f_{ly} = \frac{A_{sy}}{s_s b_c} f_{yh} \tag{1.18}$$

in which A_{sx} and A_{sy} are the areas of steel per unit length in the x and y directions, respectively; s_s is the spacing of the hoops; h_c and b_c are the dimensions of the confined core in the y and x directions, respectively; and f_{yh} is the yield stress of the hoop steel.

The compressive strength f'_{cc} can then be determined from Figure 1-14 using the effective lateral stresses in the x and y directions (f'_{lx} and f'_{ly}, respectively), which can be computed as

$$f'_{lx} = k_e f_{lx} \tag{1.19}$$

$$f'_{ly} = k_e f_{ly} \tag{1.20}$$

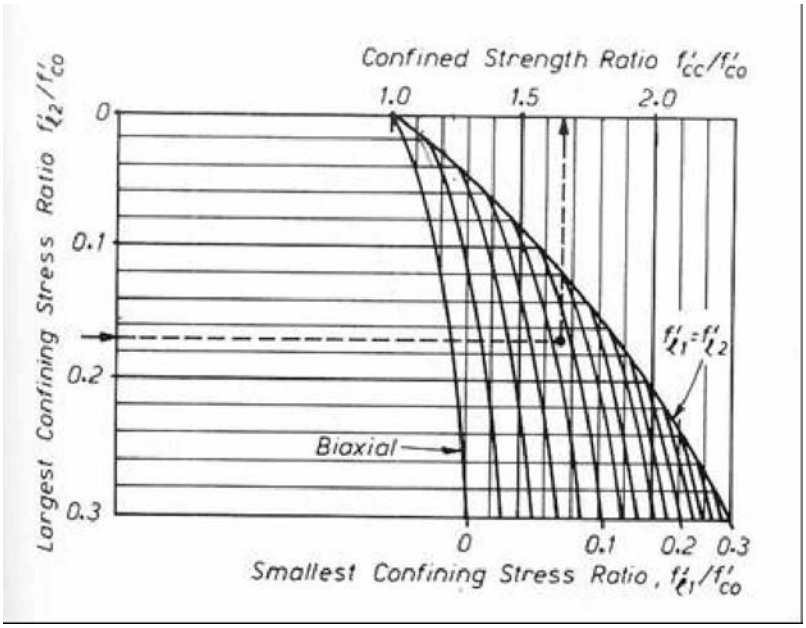

Figure 1-14 Confined strength determination from lateral confining stresses for rectangular sections (Mander et al., 1988)

The energy equation given in Mander et al. for the determination of ε_{cu} was not used in this project due to the uncertainty in applying the principles to beam-columns.

1.3.2.3 Stress-strain relation developed by Lam and Teng

Lam and Teng proposed a constitutive model for concrete in rectangular columns confined by transverse FRP reinforcement which includes both an increase in the strength and the ductility of the confined concrete. However, the model is only applicable to members with an effective confinement ratio (ECR, defined later) of at least 0.07. Generally, concrete in specimens with a lower ECR experienced an increase in ε_{cu} but no increase in strength.

Since the specimens and the bridge arches in this project all had very low ECRs, the model by Lam and Teng has to be modified to limit the ultimate compressive strength of the concrete to the unconfined strength. This model is shown in Figure 1-15.

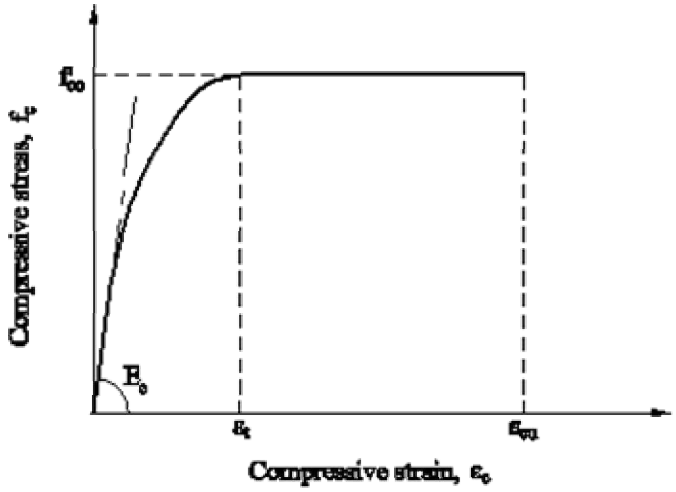

Figure 1-15 Stress-strain relationship based on Lam and Teng's model for concrete confined by transverse FRP

The relation is governed by the following relations:

$$f_c = E_c\varepsilon_c - \frac{E_c^2}{4f'_{co}}\varepsilon_c^2 \qquad (0 \le \varepsilon_c < \varepsilon_t) \qquad (1.21)$$

$$f_c = f'_{co} \qquad (\varepsilon_t \le \varepsilon_c < \varepsilon_{cu}) \qquad (1.22)$$

in which ε_t is given by

$$\varepsilon_t = \frac{2f'_{co}}{E_c} \qquad (1.23)$$

The ultimate strain is given by

$$\varepsilon_{cu} = 0.0035 + 0.024k_{s2}\frac{f_l}{f'_{co}}\left(\frac{\varepsilon_{h,rup}}{0.002}\right)^{0.45} \qquad (1.24)$$

in which k_{s2} is a shape factor for rectangular sections, f_l is the lateral confining stress and $\varepsilon_{h,rup}$ is the rupture strain of the FRP hoops. $\varepsilon_{h,rup}$ of FRP hoops in a column is generally lower than the ultimate rupture strain determined from coupon tests (ε_{frp}).

$$\varepsilon_{h,rup} = k_{\varepsilon}\varepsilon_{frp} \tag{1.25}$$

in which an average value of k_{ε} =0.586 has been found for column confined with CFRP.

The lateral stress is determined by defining an equivalent circular column with a diameter *D*, where

$$D = \sqrt{h^2 - b^2} \tag{1.26}$$

in which *h* and *b* are the dimensions of the section, respectively, as shown in Figure 1-16.

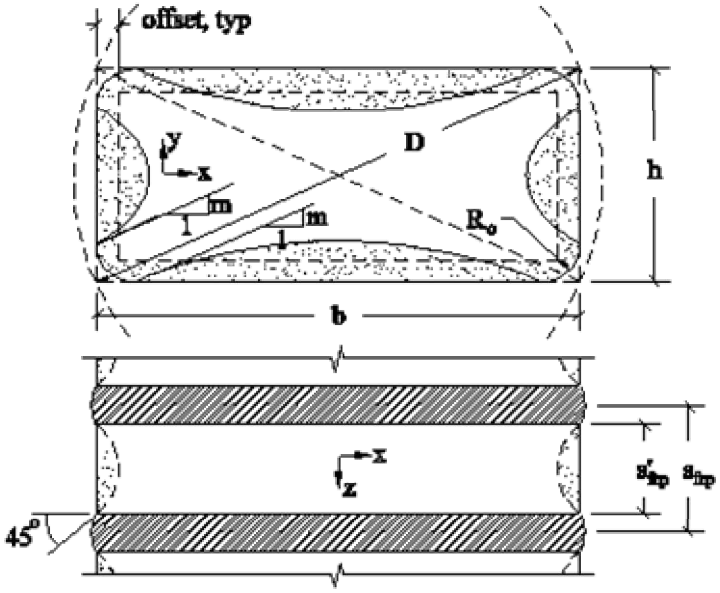

Figure 1-16 Equivalent circular column and effectively confined concrete region

The lateral stress f_l at rupture is the lateral stress for the equivalent circular column:

$$f_l = \rho_{h.\,frp}\frac{E_{frp}\varepsilon_{h,rup}}{2} \tag{1.27}$$

in which $\rho_{h,\,frp}$ is the ratio of the volume of FRP hoops to the volume of concrete, assuming that the hoops are wrapped fully around the section. The shape factor k_{s2} is based on the geometry of the section. The concrete is assumed to spall in parabolic curves which have slopes parallel to the diagonals at the ends. In Figure 1-16, this slope is labeled m, where

$$m = \frac{h}{b} \tag{1.28}$$

The ratio of the effectively confined area (A_e) to the total area of the concrete (A_c) is computed as

$$\frac{A_e}{A_c} = \frac{1 - \frac{1}{3A_g}\left[\frac{h}{b}(b-2R_c)^2 + \frac{b}{h}(h-2R_c)^2\right] - \rho_{sc}}{1-\rho_{sc}} \tag{1.29}$$

in which A_g is the gross area of the section, R_c is the radius of the corner fillets, and ρ_{sc} is the ratio of the cross sectional area of longitudinal steel reinforcement to the area of concrete.

It must be pointed out that the effects of the FRP hoop spacing were not addressed by Lam and Teng due to the fact that most, if not all, test specimens from past studies have been completely enclosed. In this study, the confinement effect between the limits the effectively confined area to a boundary that is offset within the sides of the beam by a distance $s'_{frp}/4$, where s'_{frp} is the clear spacing between the FRP hoops.

The shape factor k_{s2} is

$$k_{s2} = \sqrt{\frac{b}{h}}\frac{A_e}{A_c} \tag{1.30}$$

where $b \geq h$.

1.3.3 Summary of concrete constitutive models and their application to beam-column analysis

The three constitutive models described above are shown in Figure 1-17 for a section with arbitrary properties. The shapes of the curves change for different concrete strengths and reinforcement ratios.

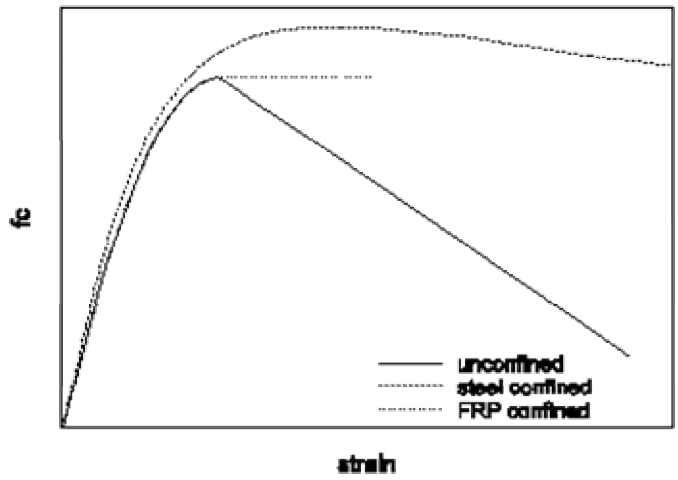

Figure 1-17 Three constitutive models for concrete

The three concrete models are used for different regions of an RC section according to the layout of the transverse FRP and steel. The assignment of the appropriate constitutive model to different regions of a section can be somewhat complex. Figure 1-18 shows an example of how the different models can be applied to a section confined with steel as well as FRP. Before rupture, (Figure 1-18 a) all three models are used. The model for unconfined concrete is used for the exterior portion, where the spacing of the FRP hoops rendered the confinement ineffective. The model for FRP confined concrete is applied to the region that is effectively confined by the FRP hoops but that is not effectively confined by the steel hoops. In the area confined by both FRP and steel, the models for steel confined concrete and FRP reinforced concrete are compared and the maximum value of f_c is used. After the FRP hoops ruptured, based on the predictions for the FRP confined model, the application of the models can be changed. (see Figure 1-18 b.) The model for steel confined concrete is applied to the area within the effectively confined steel core and the model for unconfined concrete is used elsewhere. The boundaries of the various regions are offset from the centerline of the FRP or steel confining hoops by a distance equal to one quarter of the clear spacing between the confining hoops.

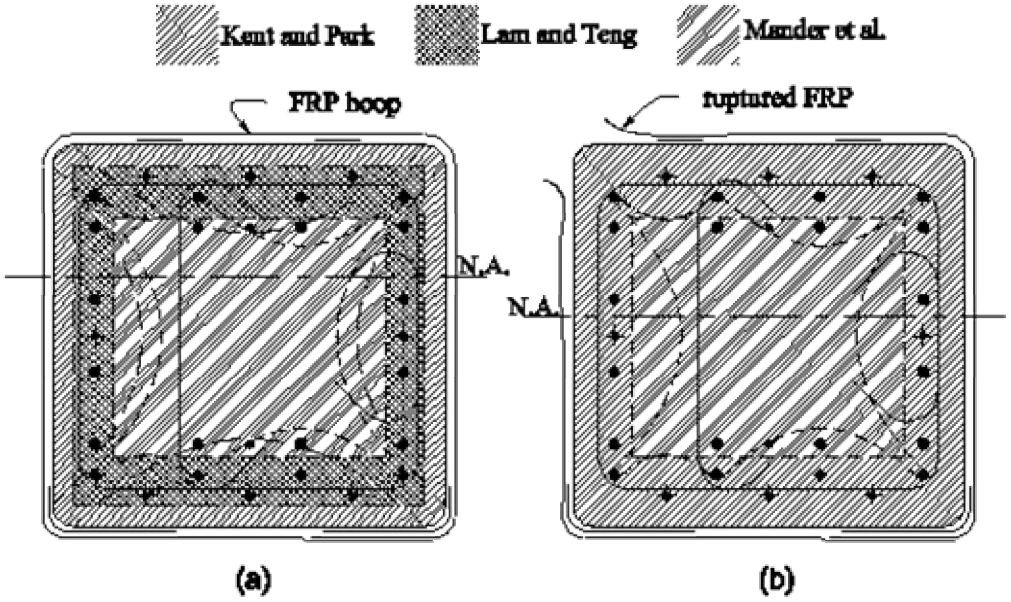

Figure 1-18 Regions of application of constitutive models: before FRP rupture; (b) after FRP rupture

1.3.4 Other material behaviors

1.3.4.1 Steel

The stress in the steel at less than the yield stress can be taken as the product of the steel strain and the modulus of elasticity of the steel, which is assumed to be 29,000 ksi in both tension and compression. In general, it is conservative to ignore the effects of strain hardening. The effects of buckling in the compression steel were ignored in this project.

1.3.4.2 FRP

The stress-strain behavior of FRP can be taken as linear elastic to rupture. Rupture is brittle and complete, leaving no strength in the FRP after failure. The strength of FRP bars and wraps in compression is not yet well understood, and was assumed to be zero in this project.

1.3.5 Moment-curvature relationships for members under combined bending and axial load

The common analysis method which approximates the concrete stress as a rectangular block was not used in this project. The definition of the rectangular stress block is based on two assumptions: (1) the concrete is stressed beyond its peak strength at the extreme compression fiber; (2) the neutral axis is within the section. These assumptions are generally invalid for the analysis of beam-columns reinforced with FRP. The FRP may rupture while the concrete is still linear elastic or the entire section may be in compression. A more fundamental approach can be used to compute the moment-curvature relation as well as the ultimate moment capacity of an RC member using the constitutive models for concrete.

Typically, the strains in a section are described in terms of curvature (κ) and the distance to the neutral axis (c). However, c can become very large and can alternate between $\pm\infty$ for sections under small bending loads. Thus, a search for c can lead to numerical

instability for beam-columns. It is also possible to describe the strain distribution using κ and the strain at the geometric center (ε_{CL}), which works much better when using a numerical solver to find the equilibrium state. This is illustrated in Figure 1-19. The strain variation along the section, $\varepsilon(y)$, is

$$\varepsilon(y) = \varepsilon_{CL} + \kappa y \tag{1.31}$$

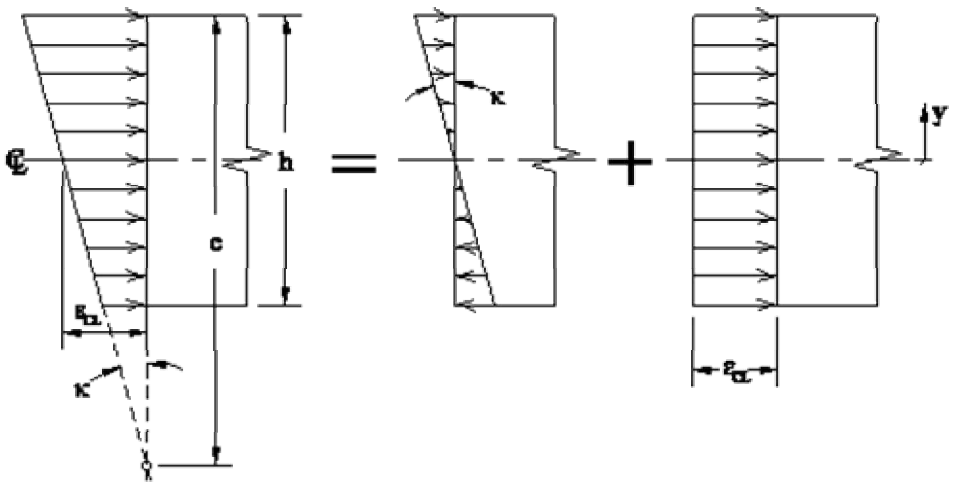

Figure 1-19 Strain distribution (Arrows indicate direction of corresponding stress.)

Figure 1-20 (a) shows an illustrative section reinforced with steel bars, internal FRP bars (FRPB), and externally bonded FRP wraps (FRPW) that is subjected to a combination of bending and compressive axial load. Figure 1-20(b) shows the strain at each level in the section. The section may have an existing strain at the time of the application of the externally bonded FRP. Let this initial strain be denoted $\varepsilon_0(y)$. Hence, the total concrete strain after the application of the FRP, $\varepsilon_c(y)$, can be expressed as

$$\varepsilon_c(y) = \varepsilon_{CL} + \kappa y + \varepsilon_0(y) \tag{1.32}$$

In a section that has been repaired or strengthened, the strains of the different material components may either be given by Equation (1.30) or Equation (1.31) depending on whether the strain in the component is affected by the initial strain configuration.

The stress in each material component can now be found with appropriate stress-strain relationships. Figure 1-20(c) illustrates the stresses in the various material components.

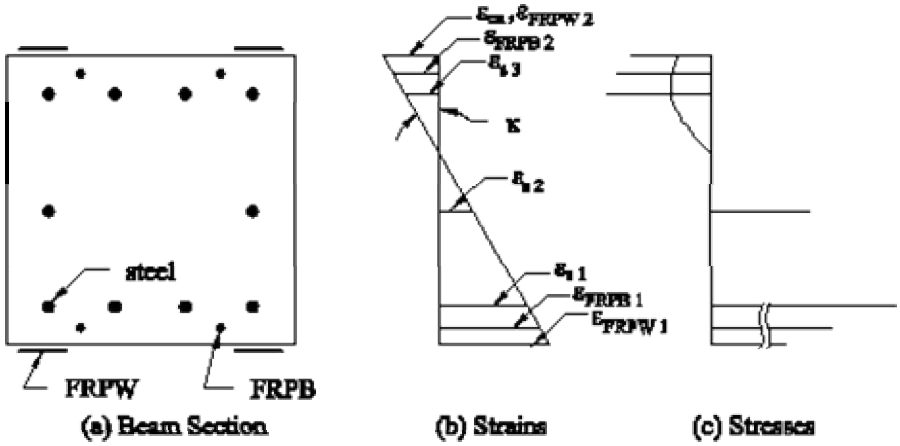

Figure 1-20 Strains and stresses in the section

Once the stresses are known, the forces in the section can be calculated. In Figure 1-21(a), the *C*'s and *T*'s denote the compressive and tensile forces, respectively, in each material component. These forces are found by integrating the stress over the area of the material component. For the concrete,

$$C_c = \int_A f_c dA \tag{1.33}$$

in which f_c is the concrete stress. Equation (1.32) can be integrated in closed form or evaluated numerically.

The resultant axial force, N_{int}, can be computed as

$$N_{\text{int}} = \sum C_i - \sum T_i \tag{1.34}$$

The applied axial force N is known at the outset of the analysis. The section is in equilibrium when $N_{\text{int}} = N$. As shown in Figure 1-21(b), N is considered to act at the geometric centroid of the section with a corresponding moment M.

The moment in the section is found by summing the moments due to each material layer in the beam about its centroidal axis. For the contribution of the concrete,

$$M_c = \int_A y\sigma_c dA \tag{1.35}$$

where y is the distance from the geometric centroid (as opposed to the neutral axis).

The moment contributions of the other material components are found by multiplying their force by their distance from the geometric centroid, taking the signs of the forces into account.

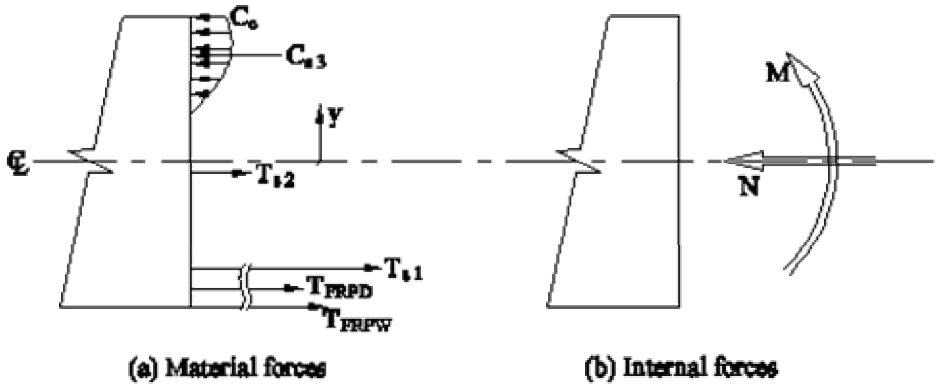

Figure 1-21 Forces on the section

To find the moment for a given N and κ, one can choose an initial value for ε_{CL} to compute the strains. The stresses are then found using the appropriate stress-strain curve for each material component. To find the resultant compressive force of concrete, the stress in concrete can be integrated in closed form or the section can be divided into thin layers for numerical integration. The internal axial resultant force N_{int} is then found by Equation (1.33) and ε_{CL} is adjusted until $N_{int} = N$. The moment is found by Equation (1.34). This process can be repeated for a range of curvatures to generate moment-curvature plots for the entire response of the section and is easily programmed or developed into a spreadsheet.

1.4 Specimen Design and Analysis

1.4.1 Bridge analysis

The test specimens considered in this study were scaled models of critical arch sections in the bridge. For this purpose, the renovated bridge structure was analyzed to find the smallest loading that could cause failure. Prior analysis by CDOT engineers showed that a critical area of the arches was at the points where they met the foundation. In this study, axial load-moment interaction diagrams were generated for arch-foundation sections as well as other locations to evaluate the load-carrying capacities of the arches. A linear elastic analysis was conducted with SAP2000, a structural analysis program. Results of this analysis were combined with the axial load-moment interaction diagrams to estimate the failure loads. These results were then checked with a nonlinear finite element analysis conducted with ABAQUS.

Two arch models were constructed in SAP2000. The first was a 2-dimensional model consisting of a single arch rib. The stiffening effect of the rest of the bridge was ignored and the foundation connections were assumed to be perfectly rigid. The arch was broken into 22 straight, uniform elements so that each section of the arch between spandrel columns was comprised of 2 beam-column elements. The arch sections were defined as plain concrete with E_c=2850 ksi. The depth and weight of each element changed based on the dimensions of the arch rib at the point that corresponded to the center of the element. The self weight of the rest of the bridge was applied at the nodes that corresponded to column-arch connections. The locations of these loads are indicated in Figure 1-22(a). The second SAP2000 model was identical to the first except for the addition of weightless concrete members which simulated the bridge deck and spandrel columns. This model is shown in Figure 1-22(b).

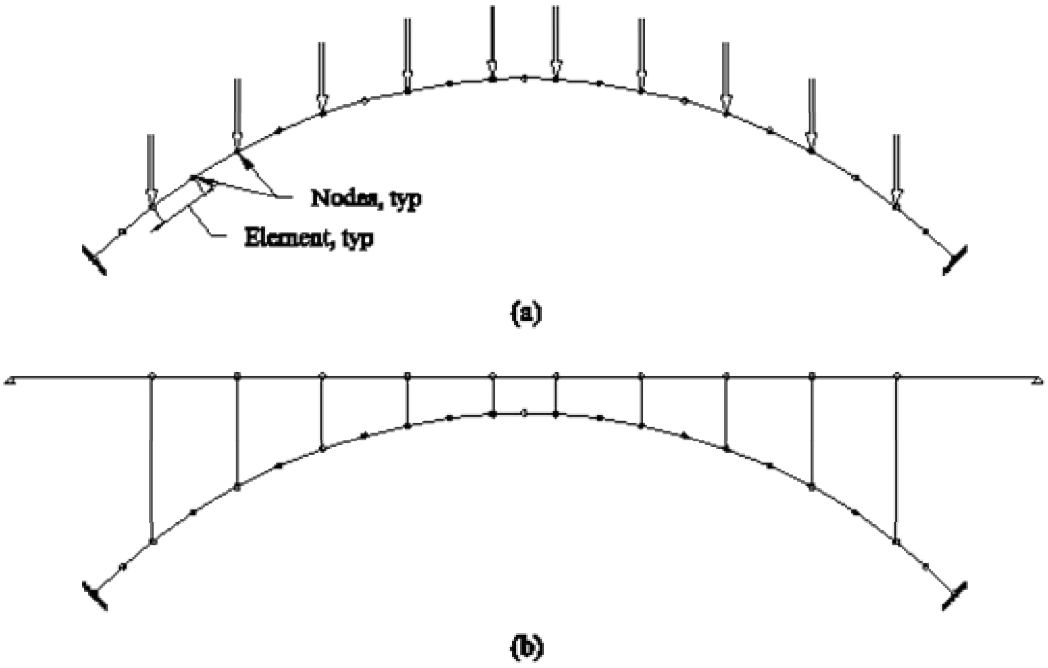

Figure 1-22 SAP2000 models: (a) Arch rib under bridge self weight; (b) Model with deck and spandrel columns

The bridge structure was first analyzed under a condition with only dead load. The dead-load strains were then calculated for the arch-foundation section. (The detailed arch strength calculations are presented in Appendix C.) Given this initial strain distribution in the existing concrete, the axial load-moment interaction diagram was calculated for the arch-foundation connection under a bending that caused downward curvature. (Hereafter, negative bending refers to moments which cause downward curvature and positive bending refers to moments which cause upward curvature.) The axial load-moment interaction diagram shown in Figure 1-23 was calculated for the sections where the arches meet foundation blocks (hereafter referred to as arch-foundation connection) using the nominal material strengths presented in Section 1.2. The interaction diagrams presented in Figure 1-24 and Figure 1-25 were computed for the arch sections located underneath the second and third spandrel columns, respectively. These diagrams show the strengths of the structure prior to the FRP strengthening using the existing concrete strength from core samples and the nominal steel strength from the original construction documents.

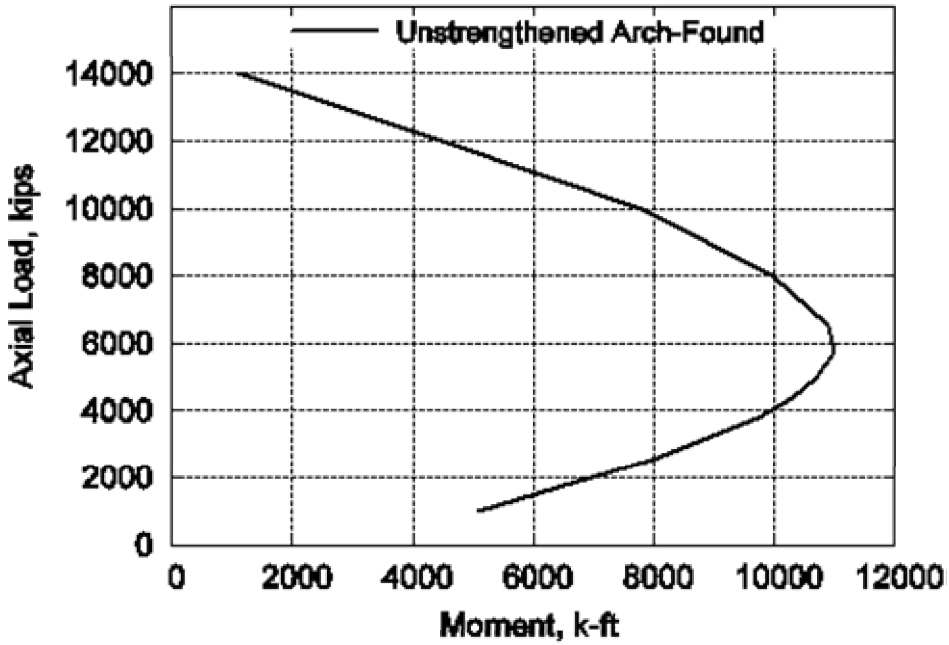

Figure 1-23 Strength interaction diagram for the arch-foundation connection

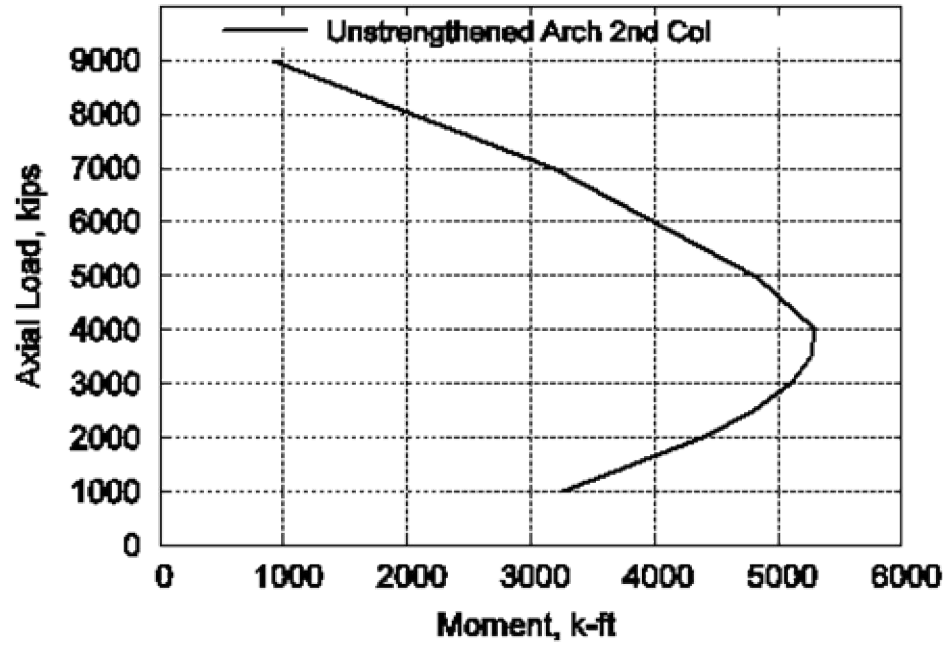

Figure 1-24 Strength interaction diagram for the arch under the second column

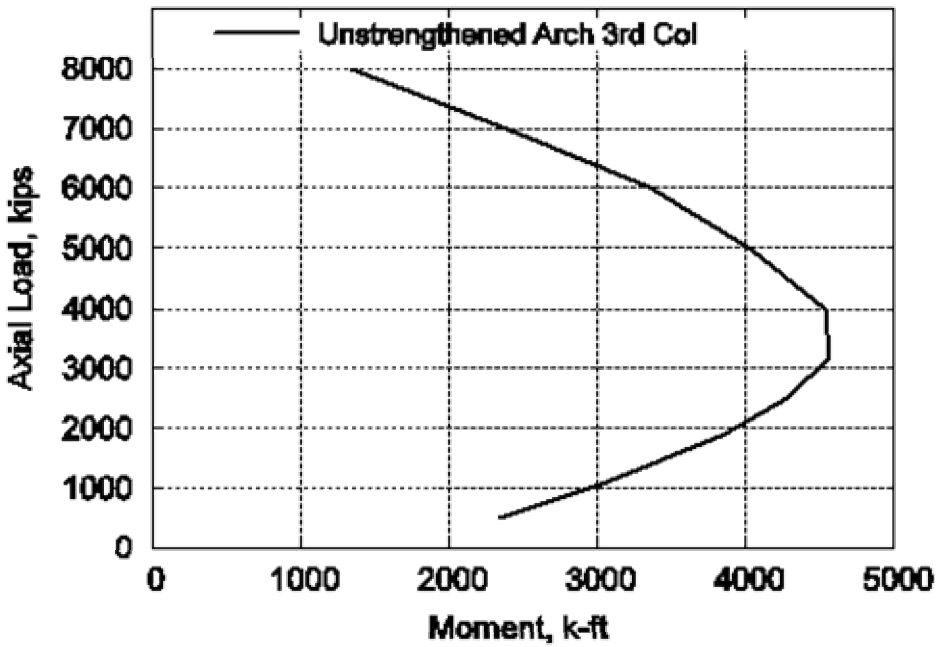

Figure 1-25 Strength interaction diagram for the arch under the third column

The live load applied to the SAP2000 model was in accordance with AASHTO specifications. The original deck, which was about 30' wide, was subjected to a design lane load of 64 lb/ft^2. A concentrated load based on the HS-20 truck with the total truck weight concentrated at a single point was applied to the arch rib at various column locations. (see Figure 1-26.) The negative moment induced at the arch-foundation connection was found to be highest when the concentrated load was placed over the second spandrel column. The concentrated load was then increased until the forces in the arch-foundation connection exceeded the strength of the section given by the interaction diagram.

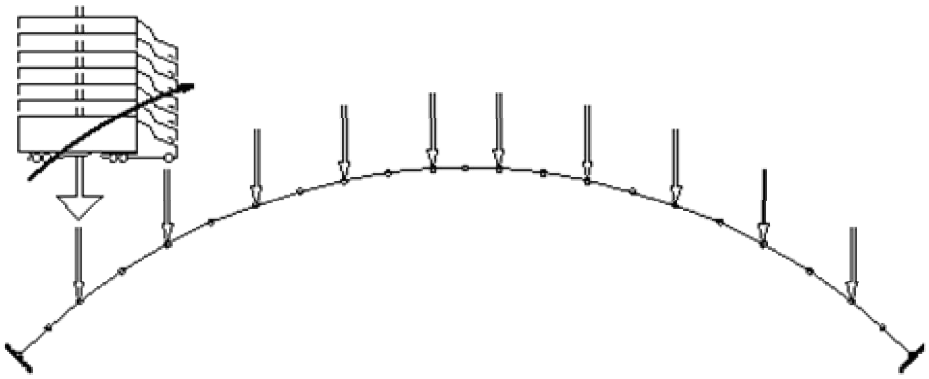

Figure 1-26 SAP2000 arch model with moveable truck load

Two sets of analysis results were obtained using the two different SAP2000 models. The results for the model consisting of only the arch rib were as follows: When considering the arch-foundation connection, the critical load configuration consisted of a force of 610 kips located at the second spandrel column. This loading resulted in an axial force (N_{cr}) and internal moment (M_{cr}) at an arch-foundation connection of 4600 kips in compression and 10500 kip-ft in bending, respectively. The internal moment in the arch under this loading condition is shown in Figure 1-27. The strength of the arch at location of loading was not critical. However, as the arch rib decreased in size higher up, the strength was limited by the positive bending in the arch directly underneath the concentrated load. For example, the arch was expected to fail at the third column under a concentrated load of 380 kips placed at the third column. In this case, N_{cr} and M_{cr} at the third column were 3430 kips and 4460 kip-ft.

The results were significantly different when the columns and deck were added to the model. The arch-foundation connection was no longer a critical section. When a concentrated load of 910 kips was placed above the second column, the arch failed directly under the load with N_{cr} and M_{cr} equal to 3950 kips and 5290 kip-ft. When the load was moved over the third column, a concentrated load of 630 kips was expected to fail the arch directly under the load. The resulting N_{cr} and M_{cr} at this location were 3830 kips and 4400 kip-ft.

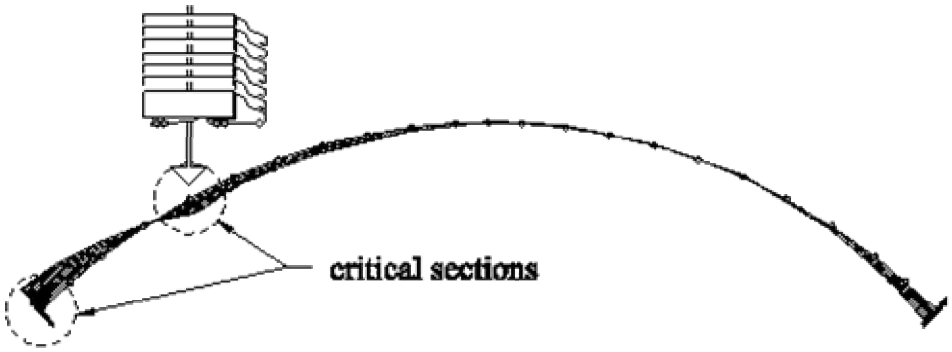

Figure 1-27 SAP2000 display of internal moment in arch under critical loading.

1.4.2 Specimen designs

1.4.2.1 General

Four quarter-scale models were tested to investigate the behavior of the two regions of the arch described above. Two of the specimens were a control specimen and an FRP reinforced specimen that were designed to simulate the connection regions between the arches and the foundations as shown in Figure 1-28(a). Hereafter, these specimens will be referred to as Foundation Control (FC) and Foundation Retrofitted (FR). The remaining two specimens were designed to simulate the arch underneath the third spandrel column. They are thus referred to as Arch Control (AC) and Arch Retrofitted (AR) as shown in Figure 1-28(b).

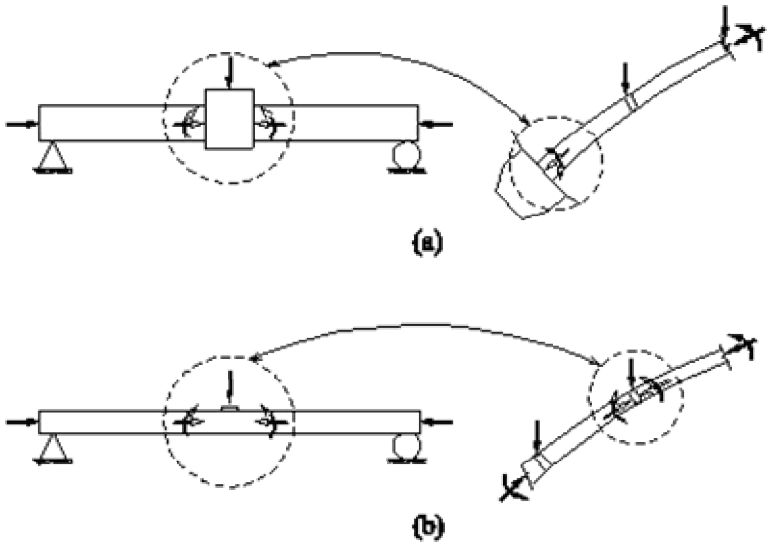

Figure 1-28 Arch and specimen regions: (a) FC and FR specimens; (c) AC and AR specimens

The loading scheme for the specimens is illustrated in Figure 1-28. The solid arrows indicate the applied loads on the specimens to simulate the loads on the actual arch segments, and the hollow arrows indicate the resulting internal forces at the critical sections. The loading scheme for the tests was designed to simulate these internal forces in a realistic

manner. The FC and FR specimens had a block with an increased cross section at midspan to simulate the foundation block.

The dimensions of the specimens were one quarter of the actual sizes resulting in a cross-sectional area of one sixteenth of the original arch. Scaling the individual material components proved to be the most challenging aspect of the specimen design. It was not possible to obtain many of the materials for the models that would exactly reflect quarter-scale. For example, 9.5 mm diameter Leadline rods were used in the actual foundation connection, but no Leadline rods were available at quarter-scale. Compromises also had to be made with the steel bars, stirrups, and Fibrwrap.

1.4.2.2 Design of FC and FR specimens

The geometry shown in Figure 1-29 was the same for both the FC and FR specimens except that the beam edges were rounded on the FR specimen to provide a smooth curvature for the Fibrwrap to enhance its confinement effect as in the actual arch. The specimens had an overall length of 16'-0" with a 2'-0" long block in the center to model the arch-foundation connections. The specimens, except for the blocks, were 19" wide by 18.5" deep.

As shown in Figure 1-28(a), the specimens were loaded with a compressive axial load and a vertical load on the central block (hereafter referred to as "center load"). They were simply supported with the supports located at 6" in from each end of the specimens. Thus, one specimen provided two arch-foundation connections. The test setup is shown in more detail in Section 1.5.

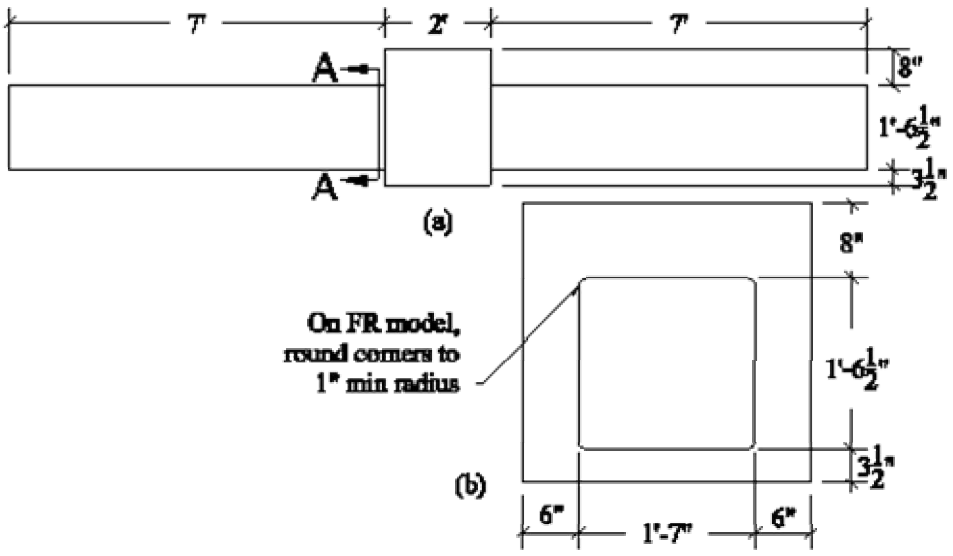

Figure 1-29 FR and FC specimen geometry: (a) side elevation; (b) end elevation.

The scaling of each material in the arch-foundation connection presented its own set of challenges. It was impossible to obtain 33 ksi steel bars like those used in the bridge. Many alternatives were considered, but the only feasible option was to use grade 40 deformed bars, which might have a yield strength of well over 40 ksi. At this point, it was decided to scale the area of longitudinal steel by a factor of 1/16, resulting in accurately scaled stiffness but a higher strength. No. 4 bars were used for longitudinal reinforcement to reduce congestion. The amount of damage to the steel reinforcing bars in the actual bridge arches due both to corrosion and drilling during the renovation process was estimated to result in a reduction of the steel area by about 10%. For this reason, the area of the longitudinal steel reinforcing in the FR specimen was reduced by replacing a No. 4 bar with a #3 bar on both the tension and compression sides of the specimen. The reinforcing for the FR specimen is shown in Figure 1-30 and the reinforcing for the FC specimen is shown in Figure 1-31.

An oversight of the original construction documents led to the doubling of the amount of steel used at the arch-foundation joint of the FC and FR specimens. In the original bridge, the footings and the arches were poured separately. Dowels extend out of the footings to reinforce the joints and the reinforcement in the arches terminates at the foundation.

However, in the test specimens both the dowels and the reinforcement ran through the entire central block.

The arch has two pairs of 5/8" diameter stirrups spaced at 1'-6" all along the arch for shear reinforcement and confinement. An exact quarter scale model would have 0.156" diameter shear reinforcement at spaced at 4.5" along the length. Many possibilities for shear reinforcement were considered, but the only available option was to use No. 3 stirrups and ties. To preserve the scaling of the steel area, these would have been placed at 1'-4", which was equal to the depth of the specimens. Stirrups at this spacing would not have been effective to prevent diagonal cracks. Therefore, it was decided to follow the minimum shear reinforcement spacing requirements of the 2002 ACI code with the understanding that there would actually be more shear reinforcement in the specimen than in an exact quarter-scale model. This is not a problem in this study, where we focus on the bending capacities of the arches rather than the shear capacities. The foundation specimens had a small L/d ratio, so extra shear reinforcement was considered beneficial to prevent unintended shear failure.

The arches in the bridge are covered with hoops of transverse Fibrwrap. In general, alternate hoops are full wraps with C-shaped wraps in between. (see Appendix A.) These hoops were provided by a single layer of Fibrwrap. Quarter scaling was achieved for the FR specimen by placing the transverse Fibrwrap in hoops covering only one quarter of the surface area of the specimen. It was decided to place 1.5" wide hoops at 6" on center and to decrease the width to 1" at 4" on center near the central block. The hoops were placed closer together in this region to help increase the effectiveness of the confinement at the section where failure was expected. They were placed farther apart elsewhere for ease of construction. The base of the arch has a 4'-0" wide band of full wrap which helps to provide confinement around the Leadline. A scaled version of this band would only be 1'-0" wide, but the region of full wraps was increased to 2'-6" to cover the entire development of the Leadline. For all full transverse wraps, the 6" overlap was the same as that used in arch. (see Figure 1-31.)

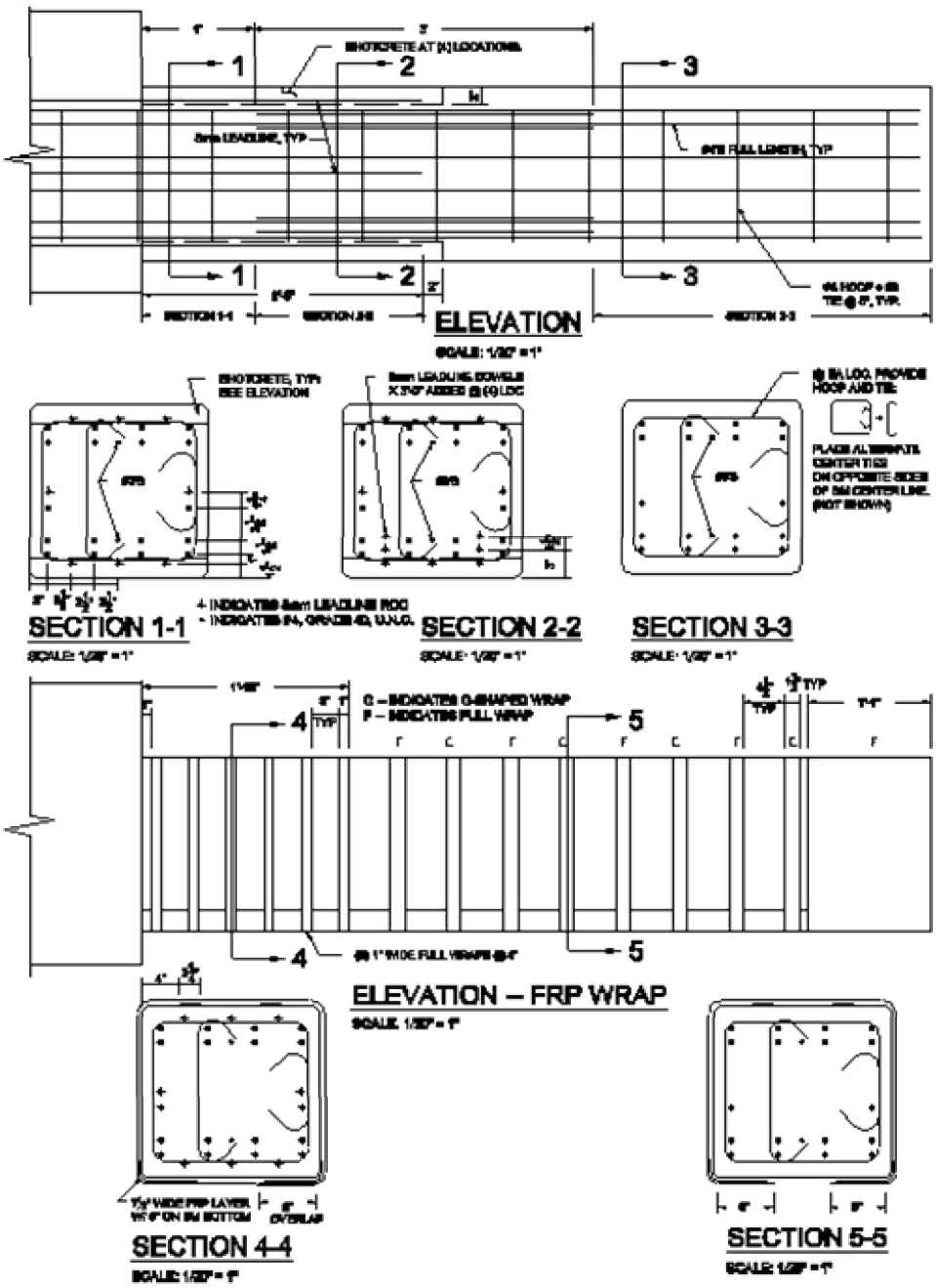

Figure 1-30 Reinforcing details for one side of FR specimen (Other side similar)

The Leadline rods used in the actual bridge strengthening are 9.5 mm (3/8 inch) in diameter and have 3'-0" of development in the shotcrete around the arch. However, the smallest available Leadline for the specimens was 8 mm (5/16 inch) in diameter. Therefore, the scaling was applied by using fewer number of 8-mm rods. At the ultimate tensile load of

the Leadline, the average bond stress at the surface of the Leadline in the bridge is calculated to be 0.797 ksi. This same average maximum bond stress was used in the scaled specimens, resulting in a development length of 2'-6".

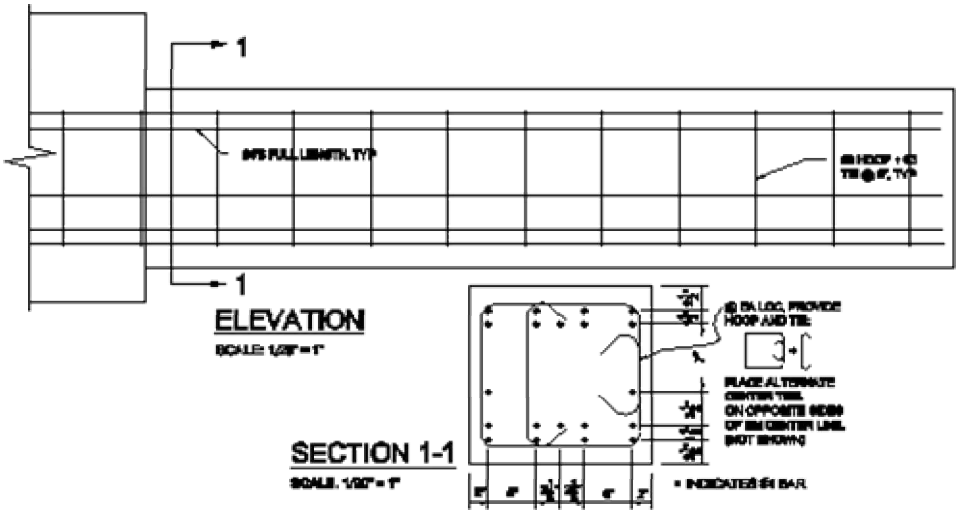

Figure 1-31 Reinforcing details for one side of FC specimen (Other side similar)

An exact quarter-scale of the section would have placed the center of the first row of steel 1.5" away from surface of the concrete. This would only allow about an inch of concrete over the Leadline rods. To provide more cover to develop the Leadline rods, the height of the section was increased by one inch to result in an 18.5" depth, and the rebar cage was decreased in height by one inch. This adjustment to the section dimensions was applied to both the FR and FC specimen. This preserved the moment arm between the resultants of the concrete stress and the tension reinforcement in the section while allowing for a 2" deep layer of shotcrete on the top and bottom of the FR specimen in which to develop the Leadline rods. As shown in Figure 1-30, the shotcrete was only placed on the tension and compression on the faces of the FR specimen. The Leadline rods on the sides of the FR specimen were placed inside the steel hoops to allow adequate cover. The FC specimen was designed with neither Leadline nor shotcrete.

The region of the arch which the FR specimen was intended to model had five layers of longitudinal Fibrwrap on the extrados and two layers on the intrados. It was not possible to

keep the same number of layers using thinner layers of the Fibrwrap to satisfy the scaling. Therefore, the Fibrwrap was placed on the specimen in a single layer on both sides and the width was adjusted to achieve the scaled cross-sectional areas.

Finally, an analysis of the moment demand and the strength variation along the FR specimen showed that there was a possibility of failure at about 1'-6" away from the central block before failure at the section adjacent to the block due to simultaneous rupture of the Fibrwrap and pullout of the Leadline. To prevent this, additional 3'-0" long Leadline rods were placed on either side of the specimen, strengthening the section at the termination of the Leadline. (see Figure 1-30, Section 1.2.2)

1.4.2.3 Design of arch specimens

The geometry of the arch specimens is shown in Figure 1-32. The specimens were 16'-0" long, 1'-7" wide and 11" high. The small cap on the top had a footprint that is a quarter-scaled version of the spandrel columns. The specimens were loaded as shown in Figure 1-28(b). The center load was applied to the cap to model the behavior of a heavily loaded column.

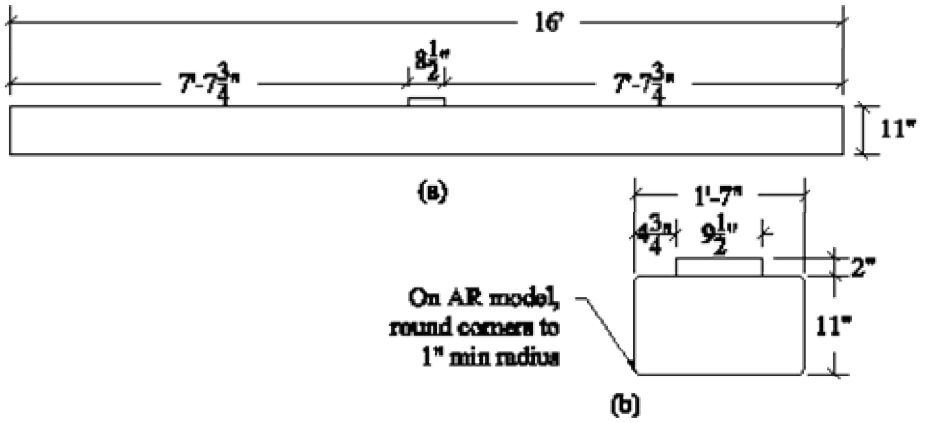

Figure 1-32 AR and AC specimen geometry: (a) side elevation; (b) end elevation

The cross section of the arch specimens remained constant throughout the length. (See Figure 1-33 and Figure 1-34.) No. 3 bars were used for the longitudinal reinforcement

because the cage was not as congested as for the foundation models. One bar was removed from the compression side to simulate the loss of steel in the arch.

The transverse steel reinforcement was comprised of rectangular hoops placed at 5" spacing. The hoops did not enclose all the longitudinal bars in the quarter-scaled specimens. Rather, the hoops were alternately placed on each side of the specimens as shown in Figure 1-33 and Figure 1-34. This was to reduce the amount of transverse steel reinforcing in the specimens while still maintaining a maximum hoop spacing of one half of the depth of the section. This was still more transverse steel than required by the scaling.

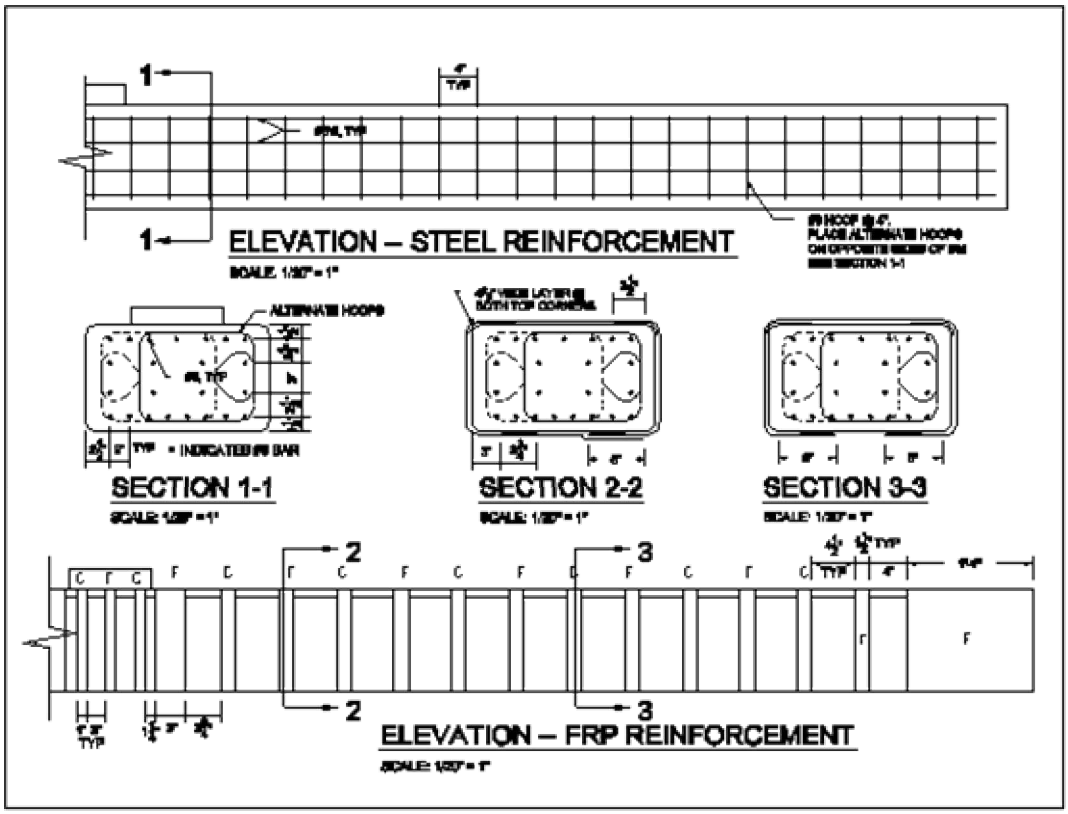

Figure 1-33 Reinforcing details for one side of AR specimen (Other side similar)

Fibrwrap was placed on the FC specimen according to a scheme similar to that used for the foundation models. The arch has two layers of transverse Fibrwrap on either side of the spandrel columns. This was simulated on the specimens with a 3" wide strip instead of the

typical 1.5” width. These hoops and their locations are shown the FRP Reinforcement elevation in Figure 1-33.

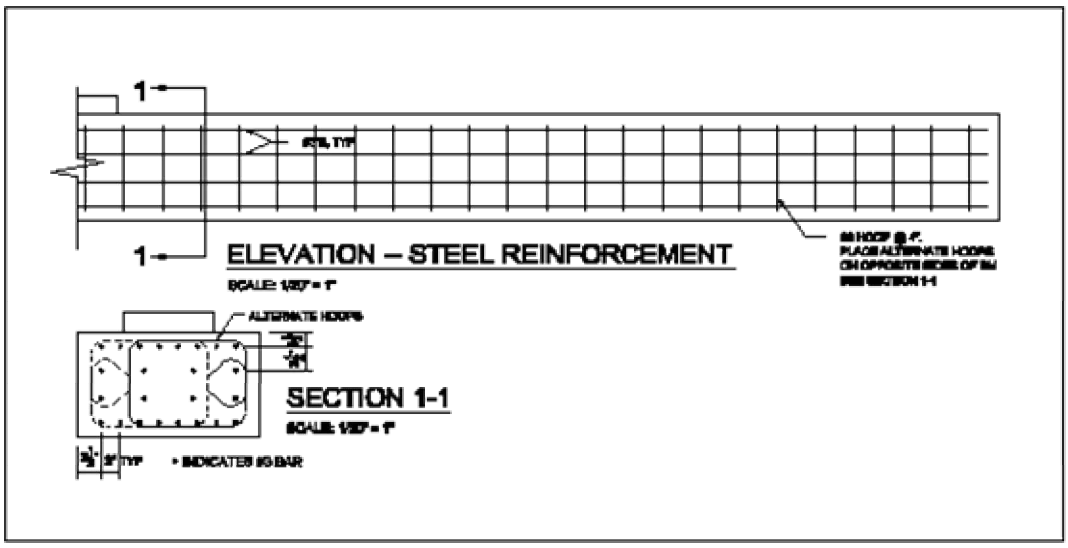

Figure 1-34 Reinforcing details for one side of AC specimen (Other side similar)

1.4.3 Specimen analysis

1.4.3.1 Strength

The ultimate strength of the specimens was predicted using the moment-curvature method (see Section 1.3) and checked with a simple rectangular stress block analysis. In the tests, it was decided to apply a compressive axial load of 30 kips to the AC and AR specimens and 75 kips to the FC and FR specimens. These were about 18% and 32% of the expected axial loads at failure, as predicted from the analysis in a previous section, if the exact scaling was followed. This is because of the limitation of the axial loading apparatus. However, results of these tests will be used to validate analytical models which will, in term, be used to predict the load-carrying behavior of the actual arches. The strengths presented in Table 1-2 were computed using the nominal material properties. (see Section 1.2) In the rectangular

stress block analysis of the FR specimen, the concrete strength used was $f'_c = 3.25$ ksi, which is the average of the values of f'_c for the concrete and f'_c for the shotcrete.

Table 1-2 Predicted specimen strengths

Specimen	Axial Compression (kips)	Mu from M-κ Method (k-ft)	Mu from Rect. Stress Block, k-ft
AC	30	49	43
AR	30	78	65
FC	75	145	124
FR	75	225	194

1.4.3.2 Moment-curvature relations

In the predicted $M-\kappa$ relation for the FC specimen, the moment rises steeply until $\kappa = 0.00016$, where the steel yields. (see Figure 1-35). As the curvature increases beyond this point, moment increases slightly and then drops gradually. The ductility of the section is due to the confinement provided by the steel hoops enabling the concrete in the core to maintain stresses at very high strains.

In the predicted $M-\kappa$ relation for the FR specimen, the Leadline, which has a lower stiffness than steel and is present in relatively small quantities, contributes little to the stiffness of the section before the steel yields at $\kappa = 0.00016$. (see Figure 1-35). The stiffness beyond this curvature is due to the ductility of the concrete confined by the transverse FRP and the tension developed in the Leadline rods. At $\kappa = 0.00098$, the transverse FRP ruptures and the moment drops off quickly due to concrete spalling. Then the moment rises again until $\kappa = 0.0021$ when the Leadline rods rupture in tension. At this point, the strength immediately drops and the strength contribution of the FRP is zero.

In the predicted $M-\kappa$ relation for the AC specimen, the behavior is similar to the FC specimen except that it maintains its ultimate strength at higher curvatures due to the decreased depth to width ratio of the section. (see Figure 1-36)

In the predicted $M-\kappa$ relation for the AR specimen, the stiffness is only slightly higher than that of the FC specimen until the steel yields at $\kappa = 0.00025$ (see Figure 1-36). The moment continues to rise with increasing κ until the tension Fibewrap ruptures at $\kappa = 0.0015$.

The predicted $M-\kappa$ relationships for all four specimens exhibit minor nonlinearity at very low curvatures. This is to the cracking of concrete. In the analytical model, concrete is assumed to develop no tension.

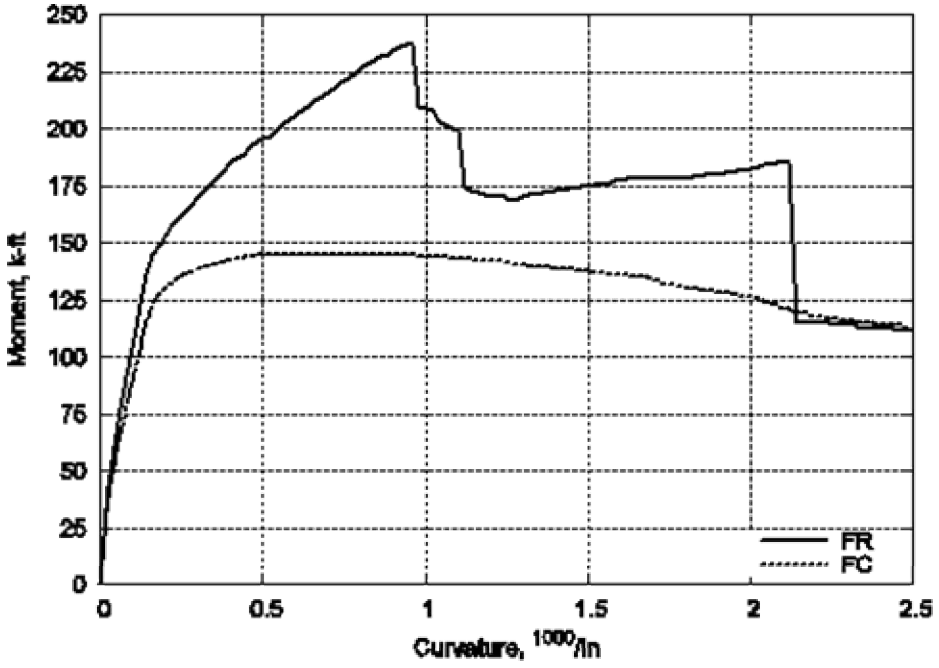

Figure 1-35 Nominal moment-curvature plots for foundation specimens

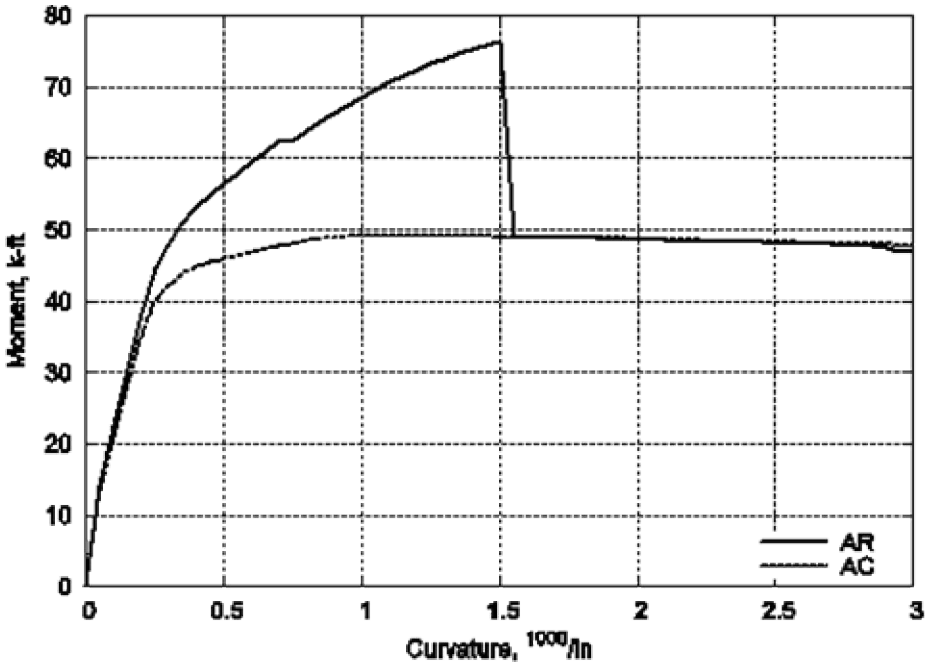

Figure 1-36 Nominal moment-curvature plots for arch specimens

1.5 Experimental Program

1.5.1 Specimen fabrication

The specimens were built in the structures lab at the University of Colorado at Boulder. The forms were constructed of wood and steel cages were placed inside. Grade 40, non-epoxy-coated deformed bars were used for all steel reinforcement. The FC and FR specimens required corner fillets of at least 1" diameter. On the bottom of the beams this was achieved by placing pieces of split 2" diameter PVC pipe in the corners of the forms. The fillets on the tops of the beams were worked in after the concrete was poured. A 2" thick layer of foam was placed on the bottom of the FR form on either side of the central block to create voids for the gunite, which was intended to mimic the retrofit of the arch bases where concrete was removed to install Leadline bars. This foam was covered with plastic, creating a very smooth surface that had to be roughened later.

The concrete for all 4 specimens, except for the shotcrete, was designed, mixed, and delivered by a local supplier. The concrete mix design used for the FC and FR specimens was different than that used for the AC and AR specimens. The former was air entrained based on the assumption that air entrained concrete was used in the bridge arches. Before the AC and AR specimens were poured, this assumption was found to be invalid. The mix design for the AC and AR specimens was adjusted to be non-air-entrained. These mix designs are shown in Table 1-3.

The concrete was placed using a large bucket carried by either a crane or a forklift. The concrete was placed in layers about 8 inches deep with consolidation between layers. The vibrator used during the pour for the FC and FR specimens was not working properly so some of the consolidation was performed manually. After the forms were removed, the concrete appeared to have been well consolidated. The exposed curing concrete was kept covered with plastic for approximately one week after pouring.

Twenty-four 4" by 8" test cylinders were poured from each batch of concrete. Half of the cylinders were cured in the same room as the specimens, the molds being removed at the same time that the forms were removed from the specimens. The other half was cured in a fog room. Some of these cylinders were tested before 28 days and others were tested within a day or two of the applicable specimen test date. The concrete strengths are shown in Table **1-5**.

After the forms were removed, the concrete in the blockouts of the FR specimen had to be roughened and cleaned to prepare the surfaces for the application of the shotcrete. The surfaces were chipped with a power chisel, care being taken to avoid striking the rebar, until the surface was rough and all loose concrete had been removed. (see Figure 1-37). The surface was thoroughly cleaned and then soaked with wet rags and sealed with plastic for at least 24 hours prior to placing the shotcrete.

Figure 1-37 The surface of the FR specimen was roughened and prepared for shotcrete. The specimen was turned upside-down by rolling on large plywood wheels, like the one supporting the far end of the specimen, to avoid disturbing the shotcrete before it had fully cured.

The shotcrete for the FR specimen was mixed and placed on two different days. Both batches were mixed at CU in a large concrete mixer and placed manually. The roughened, soaked surface was dried using pressurized air immediately before applying the shotcrete. A small amount of shotcrete was worked into the surface with a stiff brush to help achieve a strong bond between the shotcrete and the concrete before the rest of the shotcrete was applied. Fillets on the corners were formed by trowelling, an inexact method that resulted in a radius between 1" and 2". The freshly applied gunite was then covered with sealed plastic and allowed to cure. After a few days, the specimen was turned upside-down and the process was repeated.

The gunite was mixed according to a design provided by a local supplier for 4.0 ksi shotcrete. While mixing the first batch, which was to be placed on the top (compression side) of the beam, it seemed that the design called for too much water. For this reason, some of the water, which had water reducer and air entrainment mixed with it, was omitted. This extra moisture was due to the use of damp sand in the mix. In the second batch, the sand was dry and this problem was not encountered. The mix for the shotcrete is shown in Table 1-4. Twelve 4"x 8" cylinders were made from each batch of gunite for strength tests. These were cured in the same room as the specimen and kept covered while the specimen was covered with plastic. The tests of these cylinders showed that the upper shotcrete was weaker than specified and the lower shotcrete attained the target strength.

Samples from the No. 3 and No. 4 longitudinal rebars were tested in a 110-kip MTS 810 material test system to obtain their stress-strain behavior. The strengths are presented in Table 1-6. The strain data could not be relied on due to grip slippage, so Young's Modulus (E_s) was assumed to be 29000 ksi. The transverse hoop steel was not tested.

The Fibrwrap was provided by Fyfe Co. in one large roll and had to be cut into smaller pieces before application. The cutting was done with scissors. This was tedious and difficult, leading to actual widths that were often up to 0.25" wider or narrower than called for.

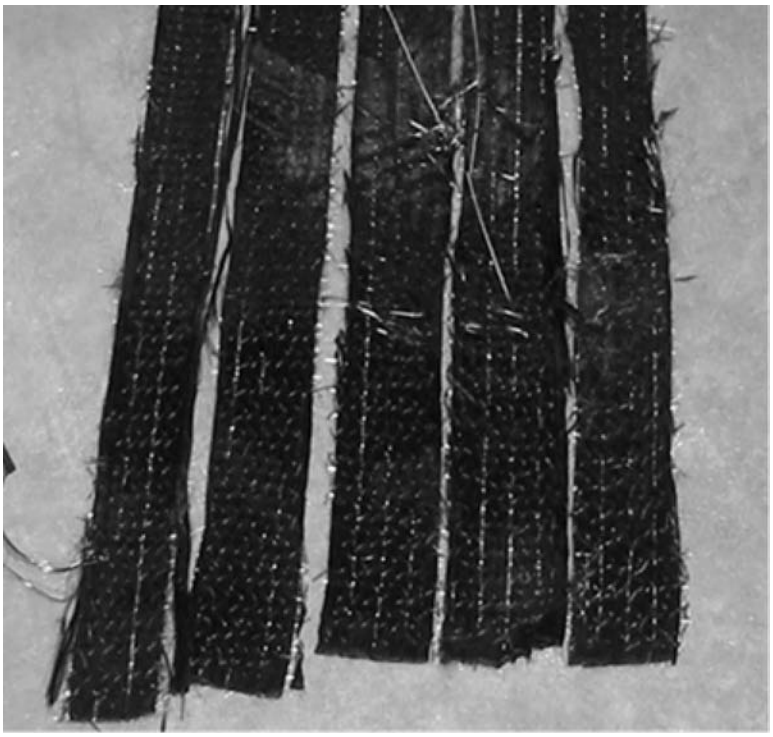

Figure 1-38 Fibrwrap strips were cut with scissors. The widths varied due to the inexactness of the cutting process.

The FR and AR specimens were hoisted outdoors and prepared for the application of the Fibrwrap. Except for some grinding of rough corners, all surface preparation of the specimens and cutting and placement of the Fibrwrap was performed by the same contractor who performed the work on the bridge. The surfaces of the specimens were roughened by sandblasting. Epoxy was rolled onto the surface of the concrete and the pieces of Fibrwrap were submerged in a pool of epoxy. The saturated Fibrwrap was laid on the epoxy-wetted concrete and pressed onto the surface with rollers. The specimens were left undisturbed and uncovered while the epoxy cured, which took about 24 hours. The application of the Fibrwrap required about 3 days, partly because the epoxy could not be applied to the specimens while they were hot from the sun. This procedure is shown in Figure 1-39.

Step 1: Wetting surface with epoxy

Step 2: Saturating Fibrwrap in epoxy

Step 3: Trimming saturated piece

Step 4: Applying Fibrwrap

Figure 1-39 Fibrwrap application procedure

Figure 1-40 Placing final transverse wrap on AR specimen. The man below the beam is rolling more epoxy into the freshly applied wraps.

1.5.2 Material properties

1.5.2.1 Concrete and shotcrete

The actual compositions of the concrete and shotcrete used in the project and their tested strengths are presented in this Section. Table 1-3 contains the mixes used for the two concrete batches as given by the local concrete supplier. Table 1-4 gives the mixes used for the two different shotcrete batches applied to the FR specimen. The problems described earlier in this section with the upper shotcrete batch added some ambiguity to the actual mix. However, the material proportions were estimated as well as possible. For the lower shotcrete, the mix design given by the local supplier was followed very closely.

Table **1-5** presents the results of the concrete and shotcrete cylinder compression tests. The concrete age at the date of the tests ranged from 73 to 96 days because the cylinders were tested as closely as possible to the time that the corresponding beams were tested. Some of the test values from the FC and FR specimens are actually averages from cylinder tests conducted over a few day period around the time of the beam tests. This is not considered to be a problem because the concrete strength had become sufficiently stable after 90 days that no strength variance was noted apart from the scatter common to cylinder tests.

Table 1-3 Concrete mix designs

Materials	Design Weights, Pounds per Cubic Yard	
	Foundation Specimens	**Arch Specimens**
Cement, Type 1-2	301	260
Fly Ash	75	70
Course Aggregate, ¾”	1700	1650
Fine Aggregate, Sand	1450	1480
Air Entrainment	2.5	
Water	315	292

Table 1-4 Shotcrete mix designs

Materials	Design Weights, Pounds per Cubic Yard	
	Upper Shotcrete	**Lower Shotcrete**
Cement, Type 1-2	574	574
Fly Ash	101	101
Int. Aggregate, No. 8	550	550
Fine Aggregate, Sand	2200 (5%-10% moisture)	2200 (dry)
Air Entrainment	1.8	2.2
Water Reducer	22	27.0
Water	245	300
Moisture in sand	110 – 220 (estimated)	

Table 1-5 Concrete and shotcrete strengths

Specimen Data	**4" x 8" Cylinder Compression Tests**
Specimen type *Fog/air cure* *Date poured*	*Date tested* *Age, days* *fc, ksi*
AC and AR Air cure 5/7/2004	7/12/2004 73 2.93
AC and AR Fog cure 5/7/2004	7/12/1004 73 3.10
FC and FR Air cure 4/14/2004	7/14/2004 91 2.59
FC and FR Fog cure 4/14/2004	7/14/2005 91 3.17
FR top gunite Air, covered 5/18/2004	7/19//2004 96 3.40
FR bot gunite Air, covered 5/20/2004	7/19/2004 96 4.97

1.5.2.2 Steel

Two sets of three tests were conducted on the No. 3 rebars and the No. 4 rebars used for the longitudinal reinforcement in the beams. Lengths were cut out of different bars and were tested in tension with a 10" clear distance between the grips of the testing machine. The results indicated very uniform strengths among similar bars, confirming the supplier's claim that all bars of a certain type were milled together. The strengths presented in Table 1-6 are based on cross sectional areas of 0.11 in^2 and 0.20 in^2 for the No. 3 and No. 4 bars, respectively.

Table 1-6 Steel properties

Steel type	Size	Grade	f_y, (ksi)	f_u, (ksi)
Longitudinal bars used in FR and FC	No. 4	40	50.5	72.7
Longitudinal bars used in AC, AR, and FR	No. 3	40	64.1	102

1.5.2.3 FRP

No tests were conducted on the properties of the Fibrwrap fabric or Leadline rods during the research described in this report. The values in Table 1-7 are based on the manufacturers' data.

Table 1-7 FRP properties

Brand Name	Manufacturer	Material	F_u, (ksi)	E, (ksi)
Fibrwrap	Fyfe Co.	carbon	127	10500
Leadline	Mitsubishi	carbon	409	21320

1.5.3 Test setup

The specimens were simply supported. The specimens rested on steel bearing plates which rested directly on roller supports as shown in Figure 1-41. A manually operated 100-ton piston was used with a small reaction frame to apply axial loads between 30 to 75 kips. (see

Figure 1-41 and Figure 1-42.). The primary bending load (hereafter referred to as "center load") was applied with two 110-ton pistons and the reaction frame shown in Figure 1-43. Both pistons were used during the foundation tests, but only a single piston was used in the arch tests. (see Figure 1-44)

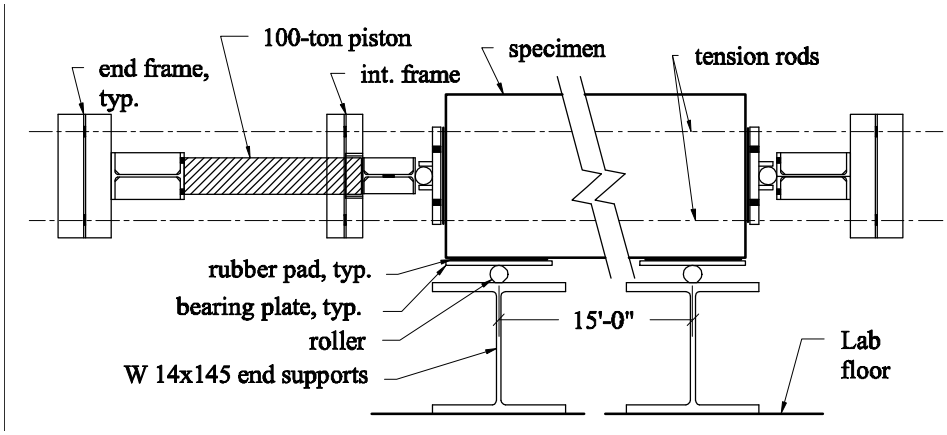

Figure 1-41 Specimen supports and axial loading frame

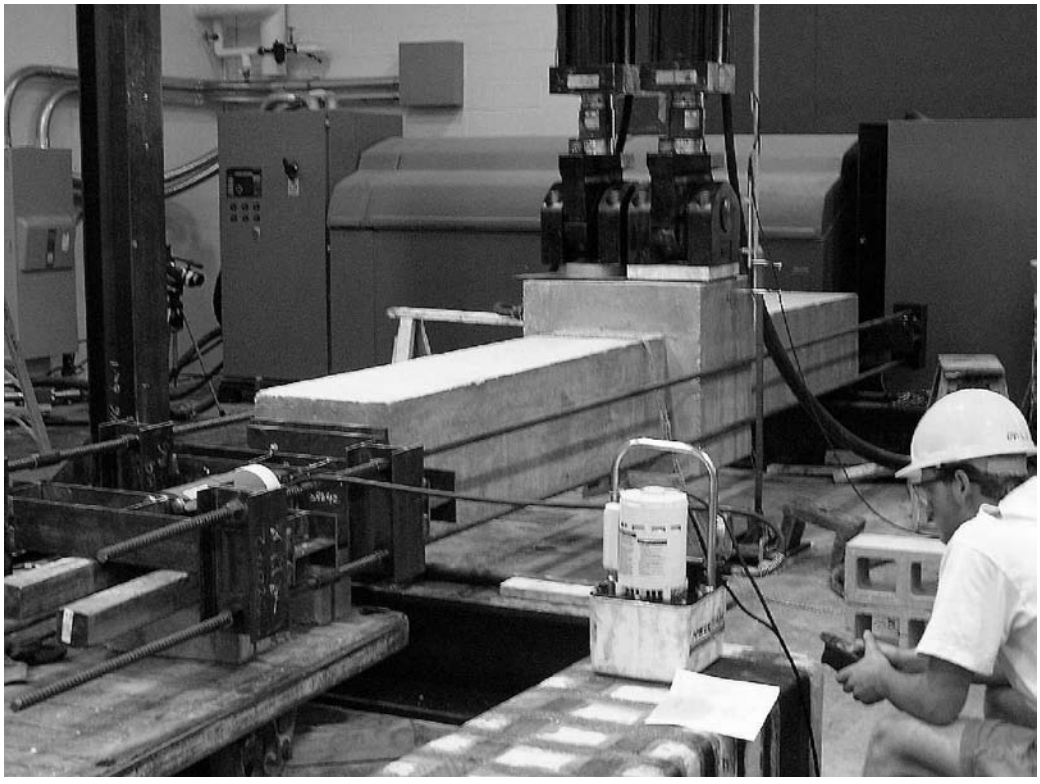

Figure 1-42 Test setup for FC specimen

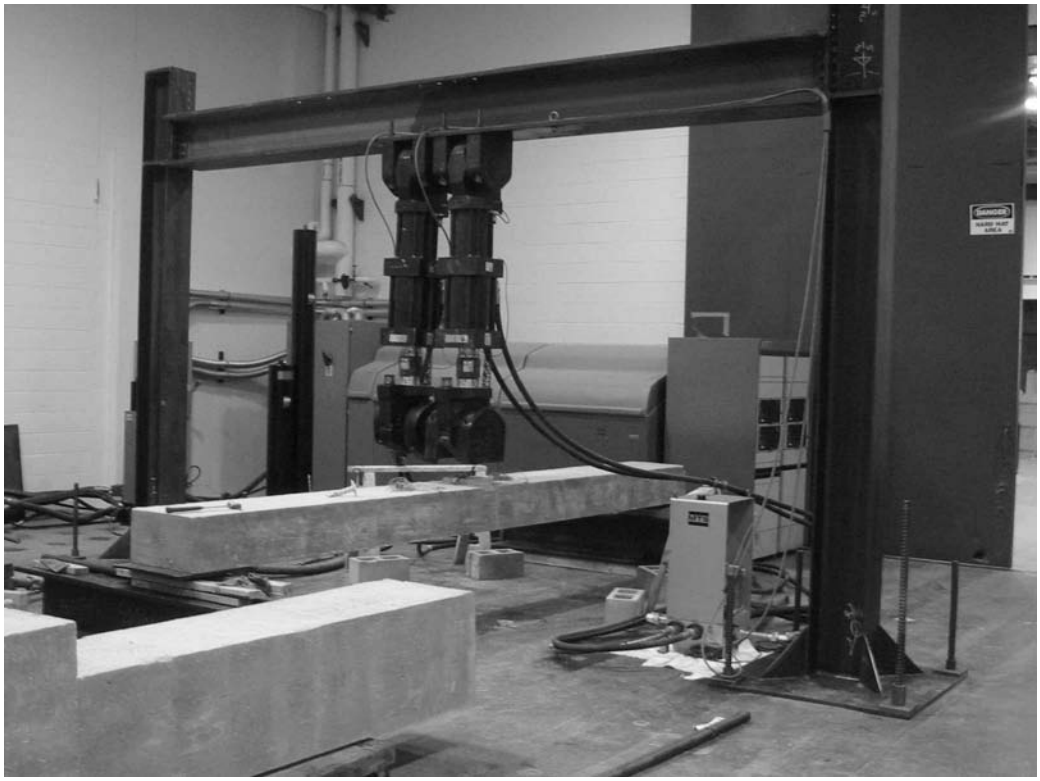

Figure 1-43 Center load reaction frame (Axial load frame not shown)

A relationship between hydraulic pressure and force was found for the 100-ton axial force cylinder by placing it in a 110-ton Tinius-Olsen testing machine. During the tests of the specimen, the hydraulic pressure in the axial force was monitored and adjusted manually to maintain a constant force. The pump could only increase the hydraulic pressure, so as the test progressed the operator had to either bleed the piston slightly or incrementally run the pump. The hydraulic pressure was difficult to maintain as the specimen deflection increased, which resulted in errors in the applied axial load of up to about one kip. However, the errors were small compared the actual loads applied. No data records were obtained of the applied axial load.

The center load was controlled with a program called Labview which allowed precise displacement control. The displacement rate of the center load actuators was set to 0.5 inches per minute for the AC and AR specimens, which resulted in test durations of 20

minutes for a 10 inch stroke. The displacement rate for the FC was initially set to 0.5 inches per minute, causing the center load to rise very quickly. The rate was immediately reduced to 0.25 inches per minute until a deflection of 0.55 inches. At this point, the rate was increased to 0.5 inches per minute. At a deflection of 3.19 inches, the rate was increased to 0.72 inches per minute to ensure that the entire test would be recorded by the data acquisition system. The total time for this test was 20 minutes, which had been set as the limiting length of data acquisition at the beginning of the test. For the FR specimen, the test length was increased to 30 minutes. The stroke was set to 0.25 inches per minute until a displacement of 4.13 inches was reached. At this point, the stroke rate was increased to 0.5 inches per minute.

Figure 1-44 A single piston was used to apply the center load to the AR specimen. This picture was taken near the end of the test.

1.5.4 Instrumentation

Strain gages were placed in each specimen at two sections where plastic hinges were expected to develop. On the FC and FR specimens this was located 1" away from the edge of the foundation block and on the AC and AR specimens it was located 1" away from the edge of the central cap. The strain gage locations are shown in Figure 1-45. They are designated "C" for a gage on concrete, "S" for a gage on steel, "L" for a gage on Leadline, and "F" for a gage on Fibrwrap. The number indicates the quantity of gages at each location. Gages were placed in pairs on the steel and Leadline on opposite sides of the bars and the strains were averaged to correct for any bending in the bar. The strain gages were zeroed before the beginning of the test by supporting the specimens in a configuration that caused zero moment at the gage locations.

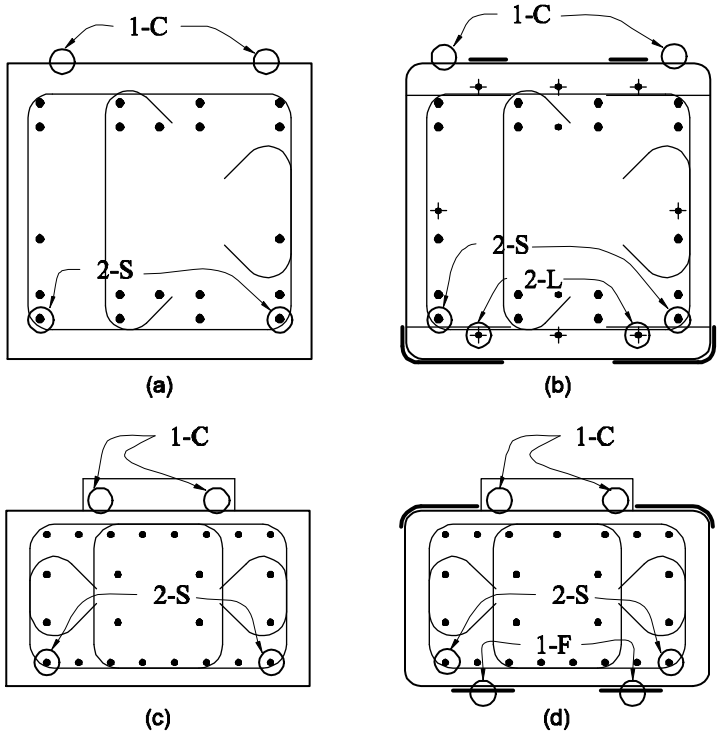

Figure 1-45 Strain gage locations: (a) FC; (b) FR; (c) AC; (d) AR.

The load and stroke data from the actuators was recorded and the displacement at the center of the beam was measured with an LVDT with a 6" stroke. The LVDT had a tendency to bend, causing inaccurate readings at large deflections. However, enough data was obtained with the LVDT at earlier stages to deduce the actual deflection of the beams from the stroke readings of the actuators by calculating the flexibility of the reaction frame and the deformation of the rubber pads.

The data from the actuators, the LVDT, and the strain gages was recorded with an MTS 490 series data acquisition system with a sampling rate of 55 kHz. During the test, the data was digitally filtered and down-sampled to 1.0 Hz.

1.6 Experimental Observations and Results

This Section presents the data collected during the tests, including load and deflection data, strain gage data, and observations related to specimen behavior and failure.

1.6.1 General

The load and displacement data were obtained with the following procedure. The load from the vertical actuators (P) at the mid-span of the beams was recorded directly from the load cells attached to the actuators. The stroke (δ_{stroke}) measured with the displacement transducers within these actuators included the deflection of the reaction frame and the deformation of the rubber pad as well as the mid-span deflection (Δ) of the specimens. The mid-span displacement measured with the external LVDT in the Foundation Control (FC) test was used to determine the stiffness of the reaction frame and the rubber for the purpose of subtracting their contributions out of δ_{stroke}. First, δ_{stroke} and the displacement of the external LVDT (δ_{LVDT}) were normalized to zero at the time when resistance from the specimen was first detected as the actuator piston was lowered. Secondly, P was plotted against the difference (δ_{stroke} - δ_{LVDT}). This curve had an initial non-linear region where the displacement was governed by compression of the rubber pad and a subsequent linear region where (δ_{stroke} - δ_{LVDT}) was due purely to the frame deflection. Finally, a line was fit to this linear portion of the curve. The slope of the line was the stiffness of the reaction frame (K_f) and the value of the line at the point $P = 0$ was approximately equal to the maximum compression of the rubber pad. It was found that the deflection of the rubber pad was less than 1/32" and was therefore ignored. An analysis of the load-vs.-differential deflection curve showed that the reaction frame deformed elastically for all four tests. As a result, the mid-span deflection of the beam was given by

$$\Delta = \delta_{stroke} - K_f P . \tag{1.36}$$

The data from the strain gages seemed consistent and accurate while they remained intact. During the tests, most of the gages on the steel and Leadline were eventually damaged and the readings became unreliable. The gages on the concrete were sometimes damaged when the adjacent Fibrwrap buckled. Most of the gages usually failed before the specimens had reached their ultimate strengths, which limited the strain data to the earlier parts of the tests.

1.6.2 Arch control specimen test data

The Arch Control (AC) specimen failed in a typical under-reinforced fashion. The sequence of events was as follows: P rose rapidly at first (See Figure 1-46). The tension steel began to yield at $\Delta = 1.1$ inch. A minimal amount of concrete spalling occurred at the upper corners of the beam and along the sections adjacent to the central cap. (see Figure 1-47). The load began to rise less quickly at a center deflection of $\Delta \approx 1.0$ inch and reached a maximum of 13.9 kips at $\Delta = 2.3$ inches. P decreased slowly throughout the remainder of the test. P was characterized by small, sharp variations at high values of Δ. This was probably due to variations in the axial load applied. It was very difficult to maintain a constant axial load using the manually operated piston when Δ was greater than about 5 inches. The small kink at the beginning of the graph in Figure 1-46 is probably due to the actuator not being in firm contact with the specimen at the beginning of the test.

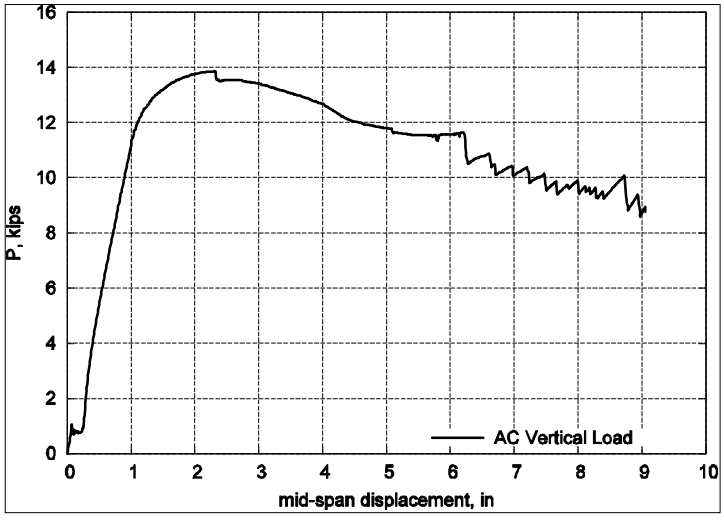

Figure 1-46 Plot of P vs. mid-span deflection for AC specimen

The AC specimen failed in bending as reflected in the final crack pattern. The major cracks were flexural running vertically until they were within a few inches of the top of the specimen, where they curved slightly toward the center (see Figure 1-48).

The load P is plotted against samples of the strain gage data in Figure 1-49. The concrete spalled at a section that was adjacent to the strain gage locations. This caused a decrease in the concrete stresses under the gages and a corresponding drop in the concrete strains after the peak load. The strain gages on the steel were damaged before the maximum value of P was reached.

Figure 1-47 Concrete spalling around central cap (AC specimen)

Figure 1-48 Crack pattern at end of test (AC specimen)

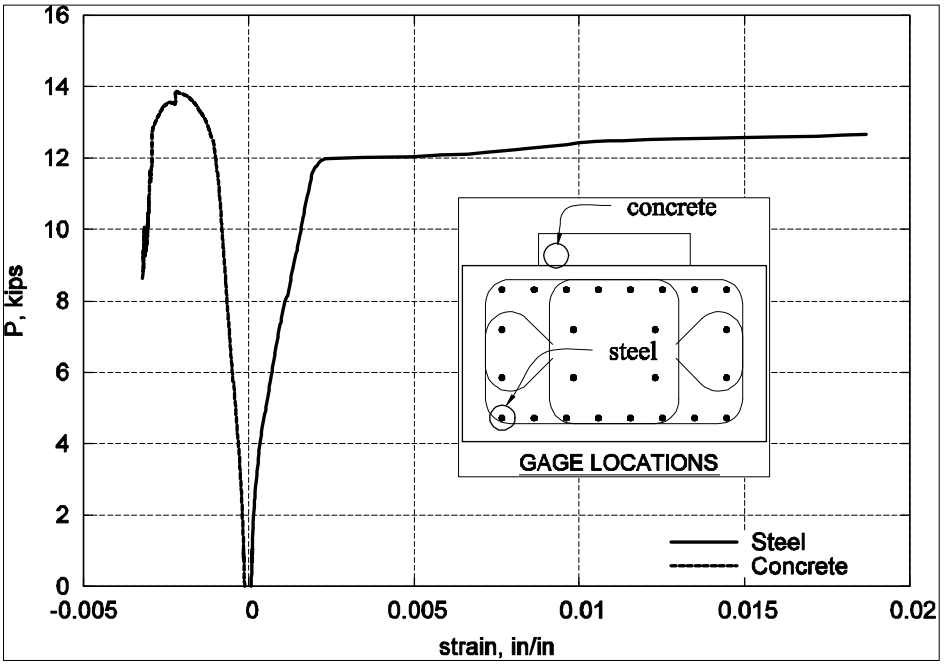

Figure 1-49 Plot of P vs. strain for selected strain gages

1.6.3 Arch retrofitted specimen test data

The strength of the Arch Retrofitted (AR) specimen was limited by the rupture of the tension FRP at the bottom of the specimen. The sequence of events during the test was as follows: *P* rose rapidly at first (see Figure 1-50). The tension steel began to yield at $\Delta = 0.93$ inch and *P* began to rise at a decreasing rate. The FRP at the bottom of the specimen suddenly ruptured at $\Delta = 2.1$ inches. *P* reached a maximum of 19.3 kips immediately before rupture. After rupture, *P* immediately dropped to 15.0 kips and continued to decrease slowly throughout the rest of the test. The Fibrwrap buckled on the sides of the central cap and outside of the 3" transverse wraps located at either side of the central cap (see Figure 1-51). Some concrete spalling could be observed around the central cap (see Figure 1-52). The underside of the specimen after the test is shown in Figure 1-53. In this figure, the longitudinal beam axis is oriented vertically. The wide Fibrwrap hoop running horizontally in the figure is one of the 3" wide hoops located on each side of the

central cap. The longitudinal Fibrwrap strips on the underside of the beam ruptured at locations about 9.5" away from mid-span. After the test, the Fibrwrap had pulled away from the concrete. This bond failure left a thin layer of concrete attached to the ruptured Fibrwrap. This is shown in Figure 1-54. The edges where rupture occurred are shown at the top of the figure.

Strain gages on the bottom Fibrwrap, installed directly at the location of the rupture, read ultimate strains between 0.0074 and 0.008 (see Figure 1-55). This was around 63% of the expected ultimate strain based on data from the manufacturer.

The transverse Fibrwrap hoops were sheared along the bottom corners of the specimen by the movement of the longitudinal tension Fibrwrap. They never ruptured along the upper corners of the specimen, nor did they experience bond failure on the sides of the specimen.

The beam failed in bending as reflected in the final crack pattern. (see Figure 1-56).

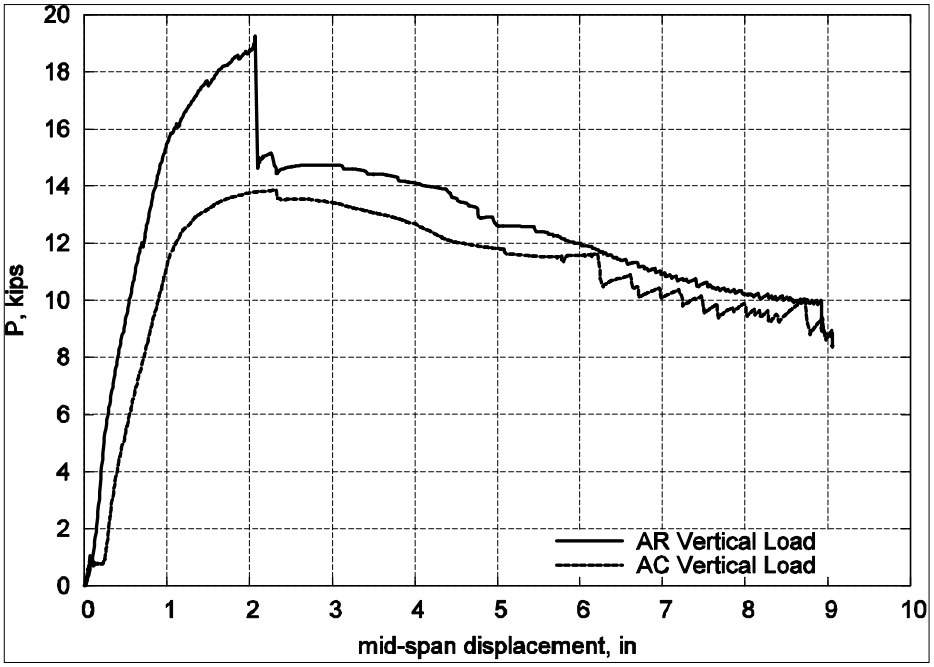

Figure 1-50 Plot of P vs. mid-span deflection for AR and AC specimens

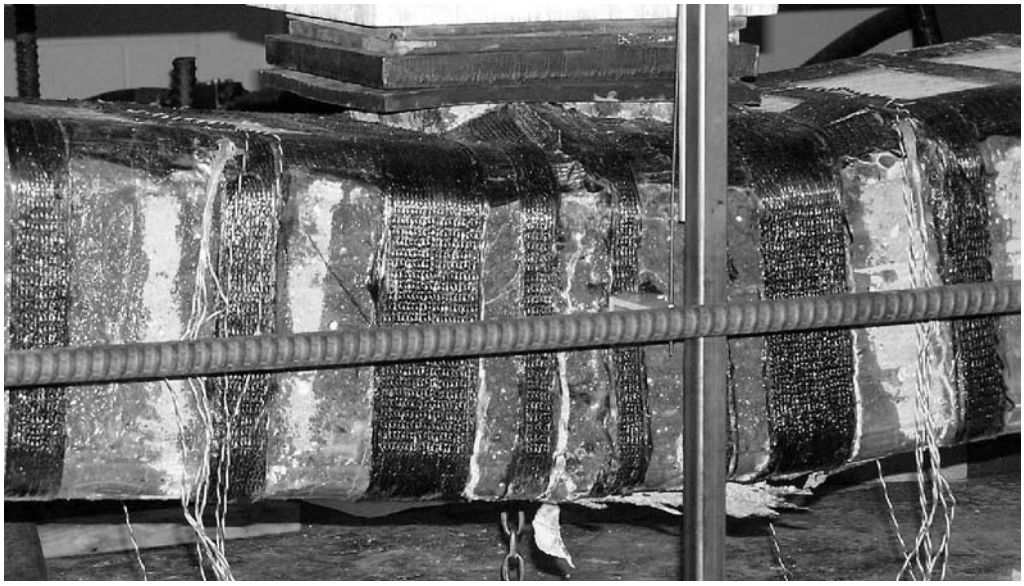

Figure 1-51 Fibrwrap with compression buckling and tension rupture (AR specimen)

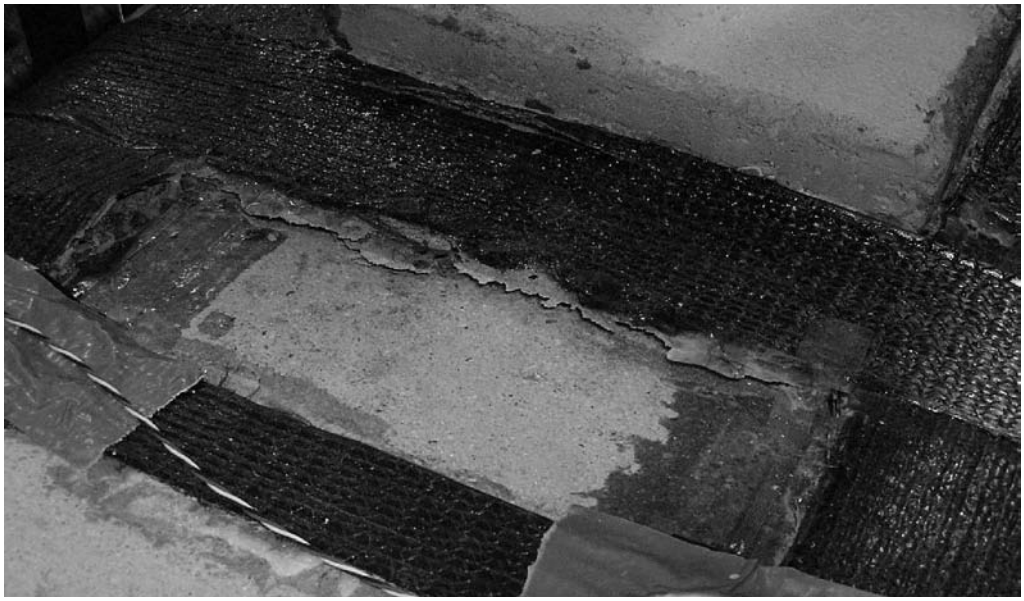

Figure 1-52 Spalled concrete underneath transverse Fibrwrap hoop (AR specimen)

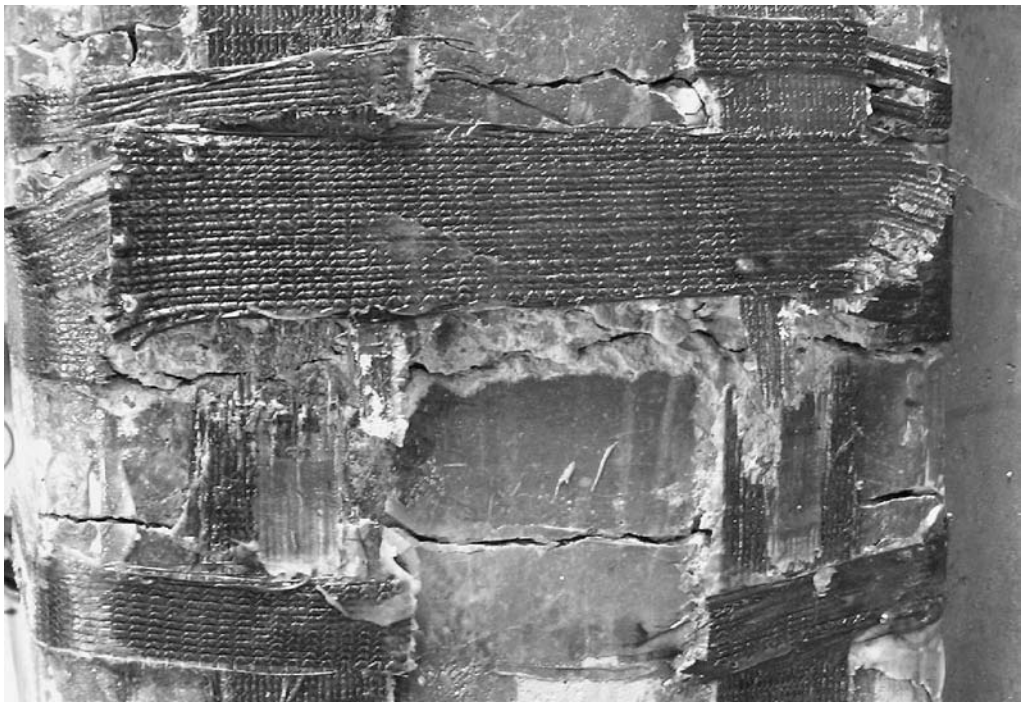

Figure 1-53 View of ruptured Fibrwrap on underside of specimen (AR specimen)

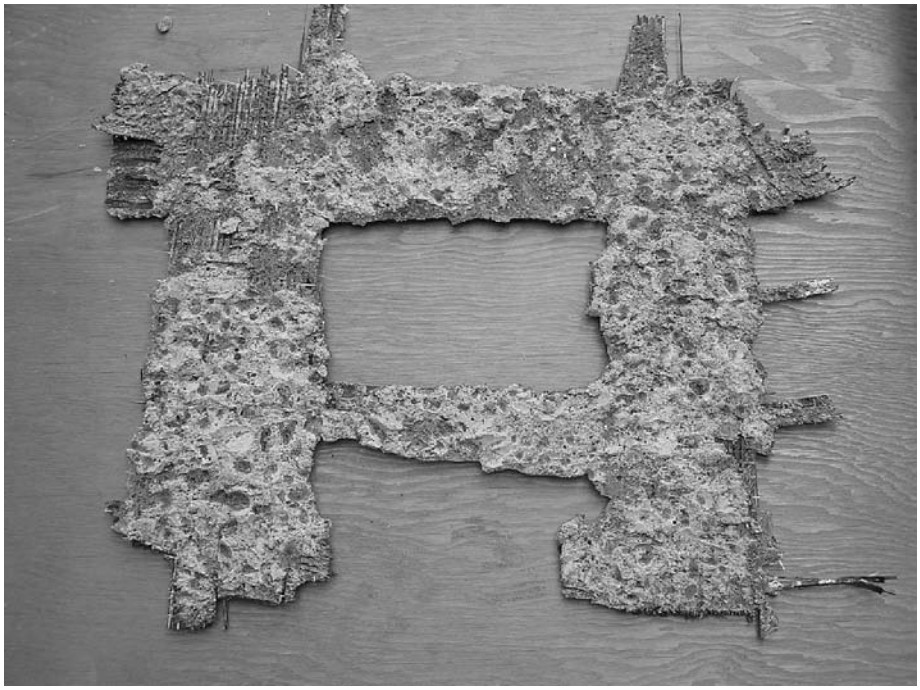

Figure 1-54 Concrete attached to the debonded tension Fibrwrap (AR specimen)

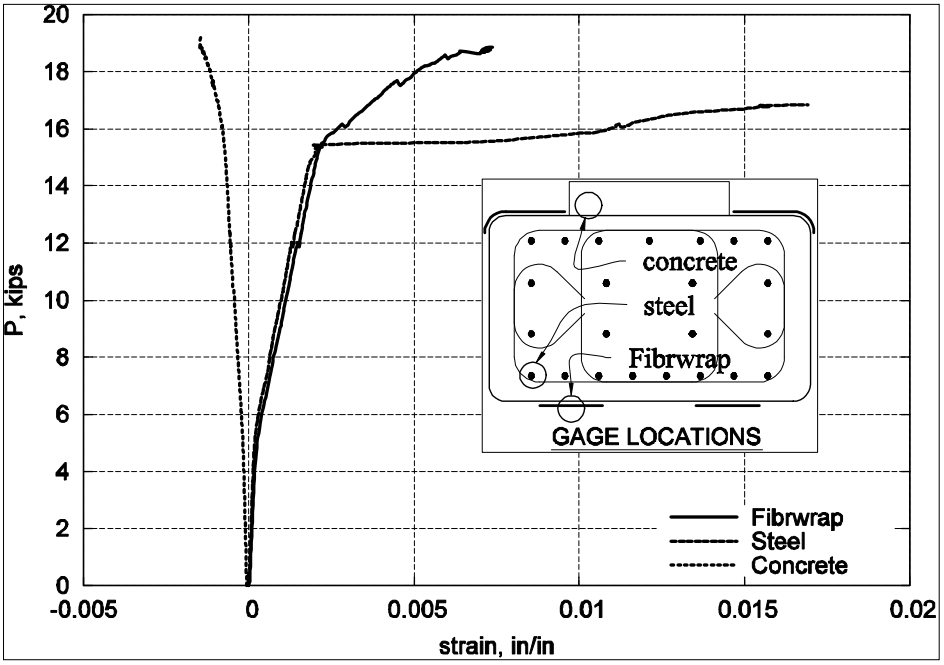

Figure 1-55 Plot of P vs. strain for selected strain gages

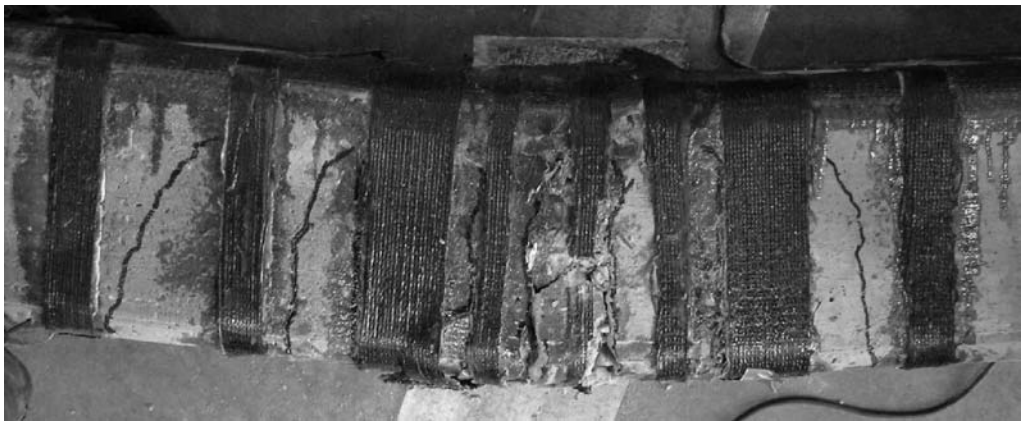

Figure 1-56 Crack pattern (AR specimen)

1.6.4 Foundation control specimen test data

The Foundation Control (FC) specimen failed in a typical under-reinforced fashion. The sequence of events was as follows: *P* rose rapidly at first (see Figure 1-57). The tension steel began to yield at $\Delta = 0.65$ inch. The concrete strain gages recorded strains of 0.004 to 0.005 between $\Delta = 0.75$ inches and $\Delta = 1.30$ inches. This may indicate the beginning of

spalling in the compressed concrete at the top, though the spalling could not be observed at that time. *P* began to rise less quickly at $\Delta = 0.84$ inch and reached a peak of 61.9 kips at $\Delta = 1.46$ inch. *P* decreased slowly until $\Delta = 5.2$ inches, when crushing of the concrete caused a more rapid loss of strength.

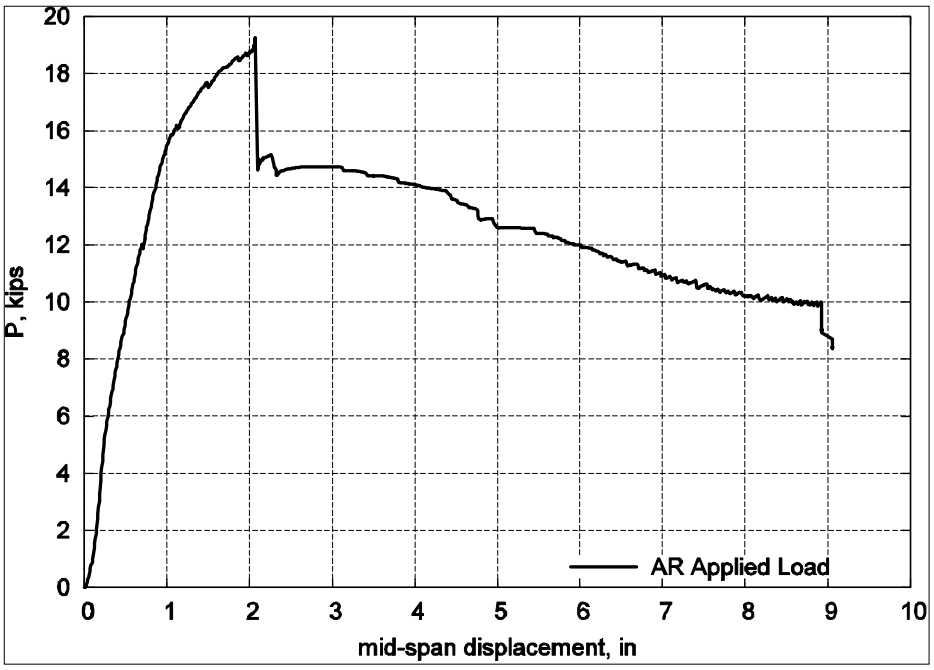

Figure 1-57 Plot of P vs. mid-span deflection for FC specimen

The strength of the FC specimen was governed by bending, but some diagonal shear cracks widened significantly after reaching the peak load. The initial cracks near the central block were vertical and near the central block (see Figure 1-58 and Figure 1-59). The diagonal crack widening was gradual and occurred only on one side of the specimen. It began at a mid-span deflection of about 6" and caused the central block to begin to rotate due to a loss of stiffness at the cracked section. By the end of the test, these diagonal cracks were the widest cracks (see Figure 1-60).

After the test, the loose debris was cleared away and the buckled compression rebar could be seen (see Figure 1-61). The section where the most damage occurred, hereafter referred to as the critical section, was not adjacent to the central block. Rather, it appeared to be

located between the first two steel hoops. This section was located at approximately 8" from the central block at the beginning of the test.

The load *P* was plotted against samples of the strain gage data (see Figure 1-62). The concrete strain curve was terminated before the ultimate load due to concrete spalling which disturbed the gage. The steel strain experienced a sharp increase at yielding until strain hardening began in the steel.

Figure 1-58 Cracking and spalling around central block (FC specimen)

Figure 1-59 Final crack pattern at non-critical side of specimen (FC specimen)

Figure 1-60 Final crack pattern at critical side of specimen (FC specimen)

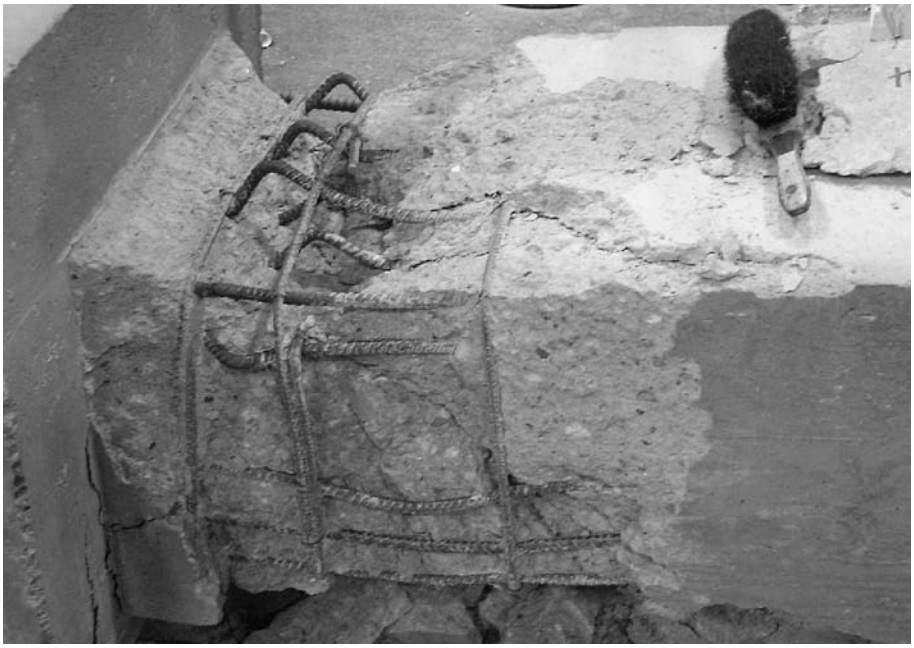

Figure 1-61 Critical section with debris cleared away (FC specimen)

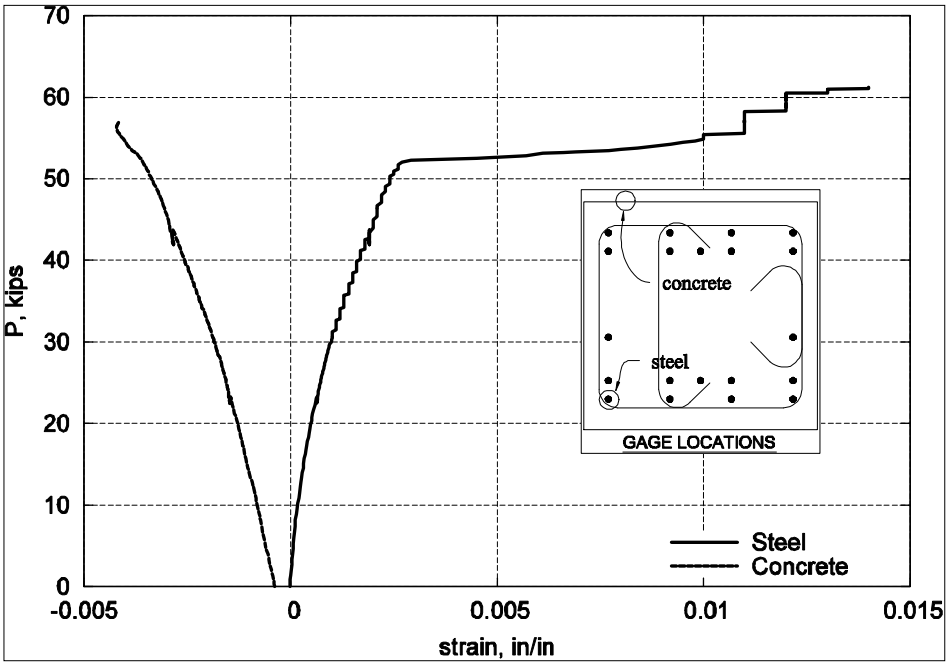

Figure 1-62 P vs. strain curve for selected strain gages

1.6.5 Foundation retrofitted specimen test data

The test of the Foundation Retrofitted (FR) specimen was characterized by the following sequence of events: *P* rose rapidly at first (see Figure 1-63). The tension steel began to yield at $\Delta = 0.65$ inch. At $\Delta = 0.9$ inch, the longitudinal Fibrwrap on the compression side buckled between the transverse Fibrwrap bands. *P* reached a maximum value of 77.3 kips at $\Delta = 2.0$ inches. *P* dropped off dramatically when the three tension Leadline rods experienced simultaneous bond failure at $\Delta = 2.1$ inches with a loud acoustic emission. For the next few inches, the load rose and fell at approximately 1" intervals of Δ as the Leadline experienced incremental pull-outs. At $\Delta = 2.3$ inches, the first transverse Fibrwrap band ruptured on one of the bottom corners with a loud acoustic emission. By this time, cracks had already developed between the concrete and the lower shotcrete, which was being peeled off the bottom of the specimen by the longitudinal tension Fibrwrap (see Figure 1-64). Eventually, the three Fibrwrap shear bands on either side of the central block ruptured. The concrete continued to crush until it had broken into small pieces (see Figure 1-65). By this time, the Leadline on the compression side of the beam had ruptured and the rebars had buckled out between the transverse steel hoops (see Figure 1-66 and Figure 1-67).

The ultimate strength of the specimen was limited by bond failure of the Leadline dowels. A picture of the tension Leadline at the point where it entered the central block is shown in Figure 1-68. In Figure 1-69, the shotcrete which was detached from the specimen had been removed to expose the Leadline. The surface of the Leadline rods appeared to be undamaged during the test. It appeared that the Leadline bond failure was due to the crack that developed between the concrete and the lower shotcrete. This crack appeared to be due to the force exerted on the shotcrete by the tension Fibrwrap.

P is plotted against samples of the strain gage data in Figure 1-70. The data from the concrete and steel strain gages was similar to the data for the FC specimen, though the gages failed before the ultimate load was reached. The Leadline strain (ε_{LL}) can be more easily understood from the plot of ε_{LL} vs. Δ, as shown in Figure 1-71. The Leadline strain

experienced a sudden reduction at the initial pullout and then rose significantly before a second pullout. This process repeated itself multiple times with diminishing peak strains. Data from different locations in the section indicated that all Leadline rods experienced bond failure simultaneously. The Leadline strain at pullout ranged from 0.0087 to 0.0105.

Both of the monitored Leadline rods pulled out simultaneously. It appeared that the pullout of one rod caused a sudden increase in the stress of the other two and led to their simultaneous pullout.

The crack pattern indicated that some of the deflection was due to shear. The cracks that were farther away from the central block were diagonal up toward the center of the beam. This indicates that the transverse Fibrwrap hoops probably experienced increased strains due to the shear forces and thereby ruptured.

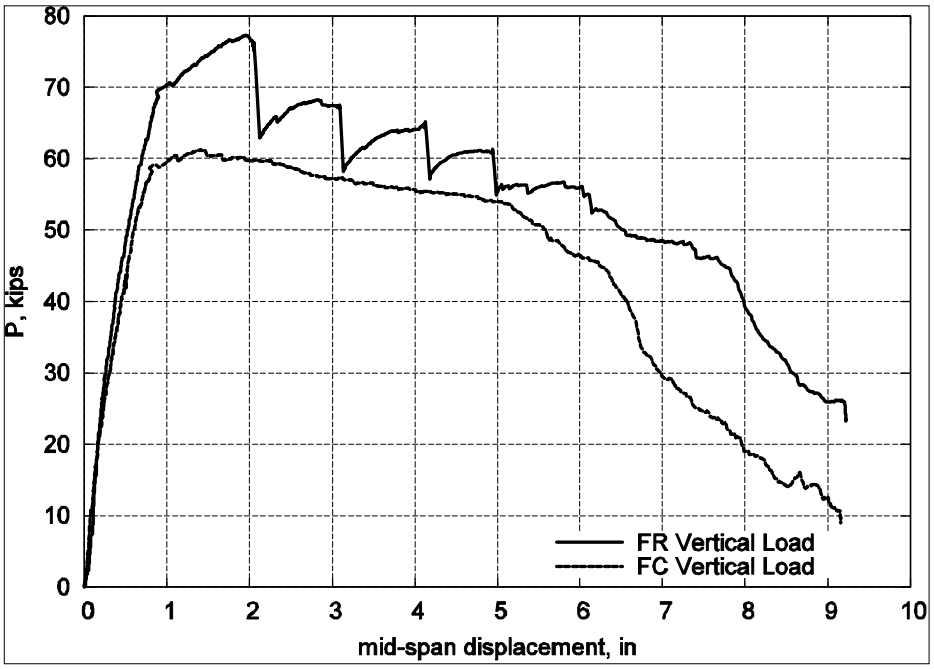

Figure 1-63 P vs. mid-span deflection for FR and FC specimens

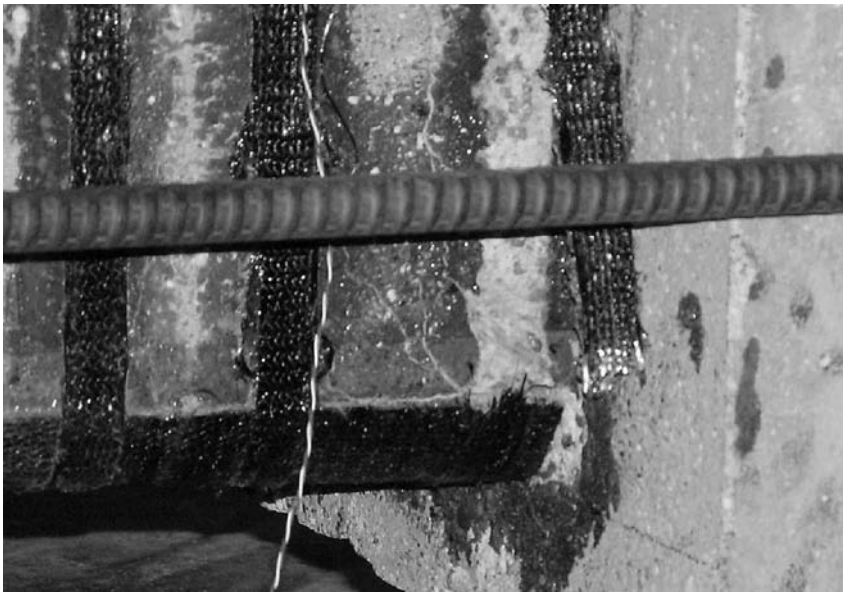

Figure 1-64 Ruptured transverse Fibrwrap where shotcrete pulled away from FR specimen

Figure 1-65 Critical section of FR specimen

Figure 1-66 Compression region of the FR specimen critical section

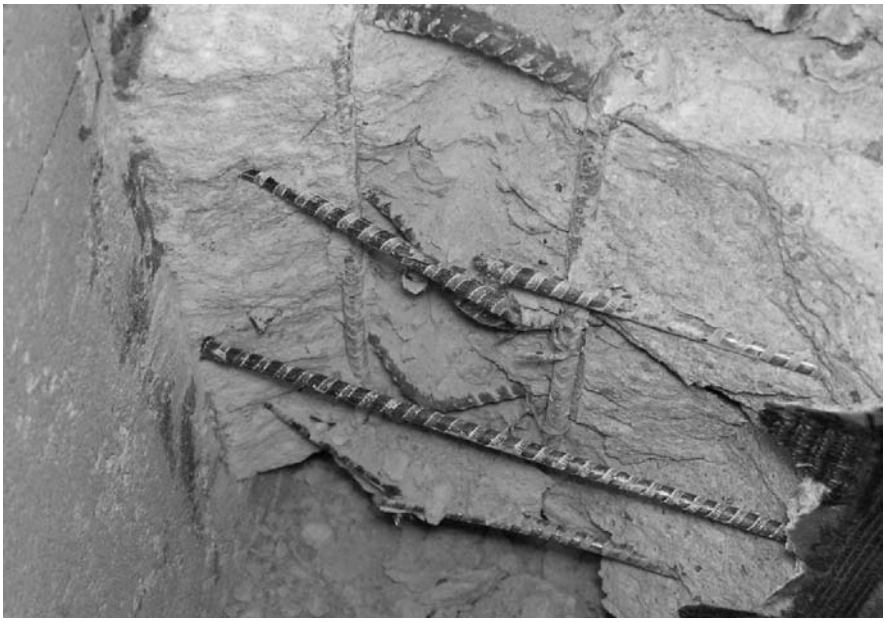

Figure 1-67 Buckled rebars and ruptured Leadline at the top of the FR critical section (Note: specimen is lying on its side and loose debris has been cleared away.)

Figure 1-68 FR specimen tension Leadline between concrete and shotcrete

Figure 1-69 FR specimen tension Leadline with loose shotcrete patch removed

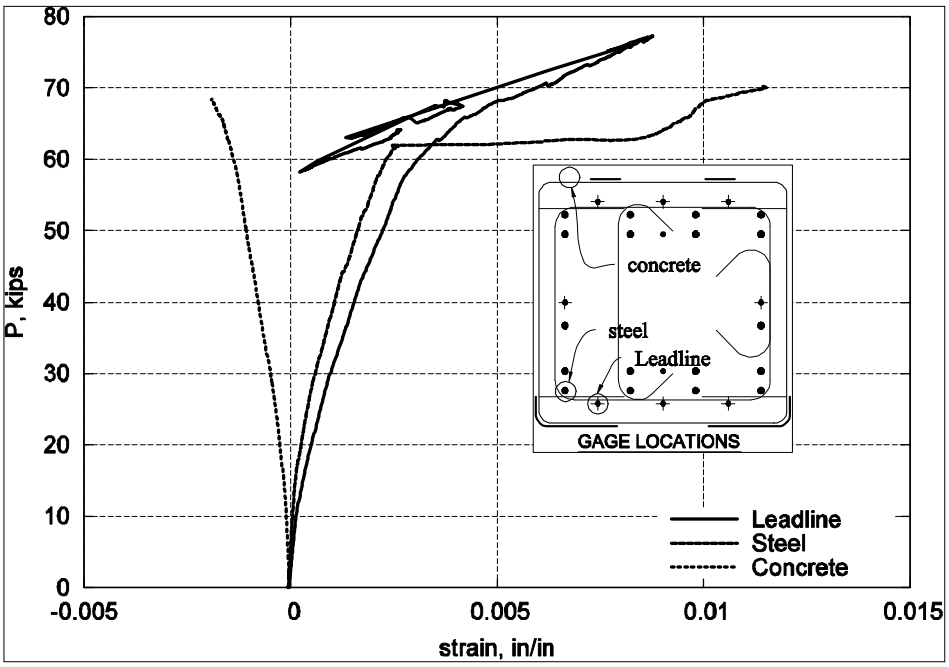

Figure 1-70 P vs. strain curve for selected strain gages

Figure 1-71 Plot of Leadline strain vs. mid-span displacement

1.7 Analysis of Experimental Results

1.7.1 General

From the experimental results, the moment resistance developed at a section of a specimen can be computed as the sum of the moments due to the vertical actuators (M_{CL}), the eccentricity of the axial load (M_{ecc}) at the section, and the self-weight of the specimen ($M_{self-wt}$).

$$M(x) = M_{CL} + M_{ecc} + M_{self-wt} \tag{1.37}$$

where x is a coordinate along the specimen axis. $M(x)$ is defined to be positive for a simply supported specimen when the center of the specimen deflects downward. M_{ecc} is given by the product of the axial load N and the vertical displacement $\delta_y(x)$ at the section.

$$M_{ecc}(x) = N\delta_y(x) \tag{1.38}$$

where $\delta_y(x)$ is positive when the specimen deflects downward.

One of the goals of this project was to compare the theoretical $M-\kappa$ plots with the behavior of the specimens. The curvature in a section can be computed from the strain gage data as

$$\kappa = -\frac{\varepsilon_2 - \varepsilon_1}{y_2 - y_1} \tag{1.39}$$

in which ε_1 and ε_2 are the strains measured at the locations y_1 and y_2, respectively, where y is the vertical position in the section as defined in Figure 1-19.

Curvature values could be different when computed using different sets of strain gage data. For the Arch Control (AC) and Foundation Control (FC) specimens, the concrete strains (ε_c) in the top compression region and the longitudinal tension steel strains (ε_s) were measured. For these specimens, the curvatures were computed from the values of ε_c and ε_s. For the Arch Retrofitted (AR) and Foundation Retrofitted (FR) specimens, the

longitudinal FRP strains (ε_{frp}) were also measured, as discussed in Section 1.5. In these two specimens, one set of curvatures was computed from ε_c and ε_s, and another set was computed from ε_c and ε_{frp}.

In general, the $M-\kappa$ plots from the test data were terminated before the ultimate moment of the section was reached due to the failure of the strain gages.

1.7.2 Moment-displacement responses

The plots of the internal moments vs. the mid-span displacements are shown in Figure 1-72 through Figure 1-75. Each figure contains four curves showing the total moment, the vertical load moment, the eccentric moment, and the self-weight moment. For the AC and AR specimens, the vertical load was approximated as a point load acting at mid-span, and the moments were computed at mid-span. Figure 1-72 and Figure 1-73 show the moments at mid-span for the AC and AR specimens under this simplified loading condition. Figure 1-74 and Figure 1-75 show the moments at the faces of the central blocks of the FC and FR specimens, in which cases the approximation of the vertical load as a point load was unnecessary.

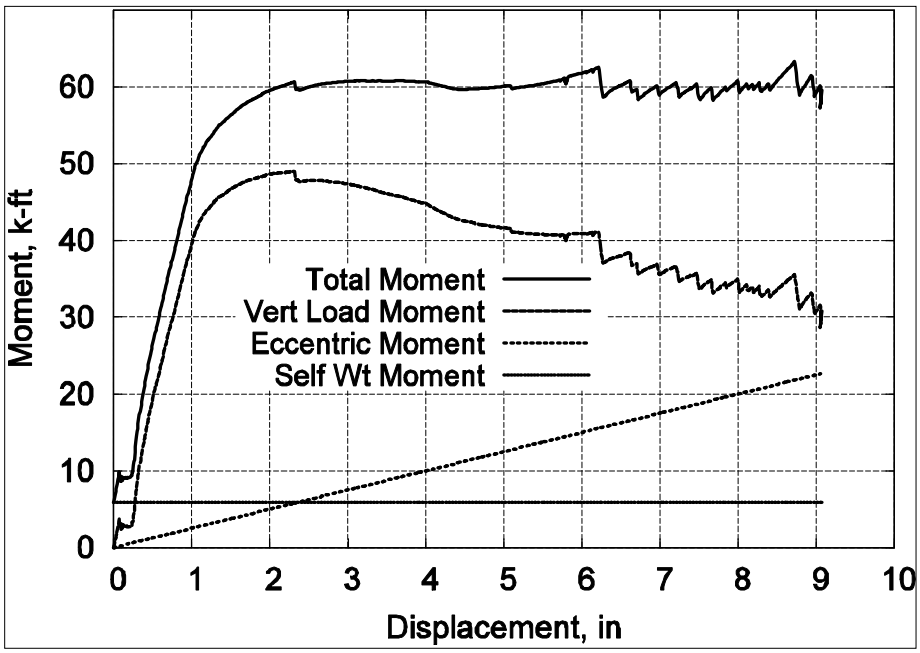

Figure 1-72 M **vs. mid-span deflection for AC specimen**

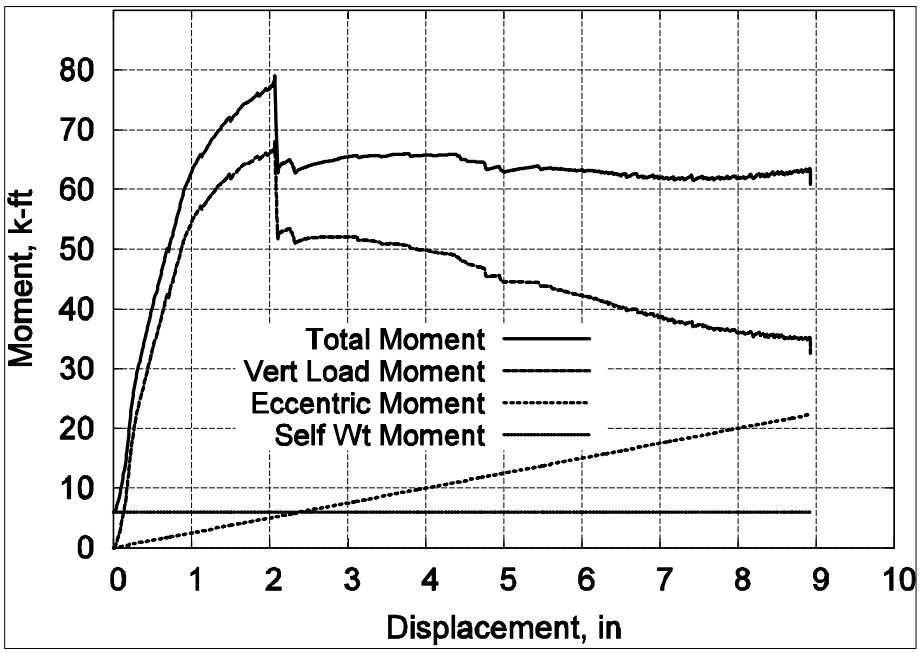

Figure 1-73 M **vs. mid-span deflection for AR specimen**

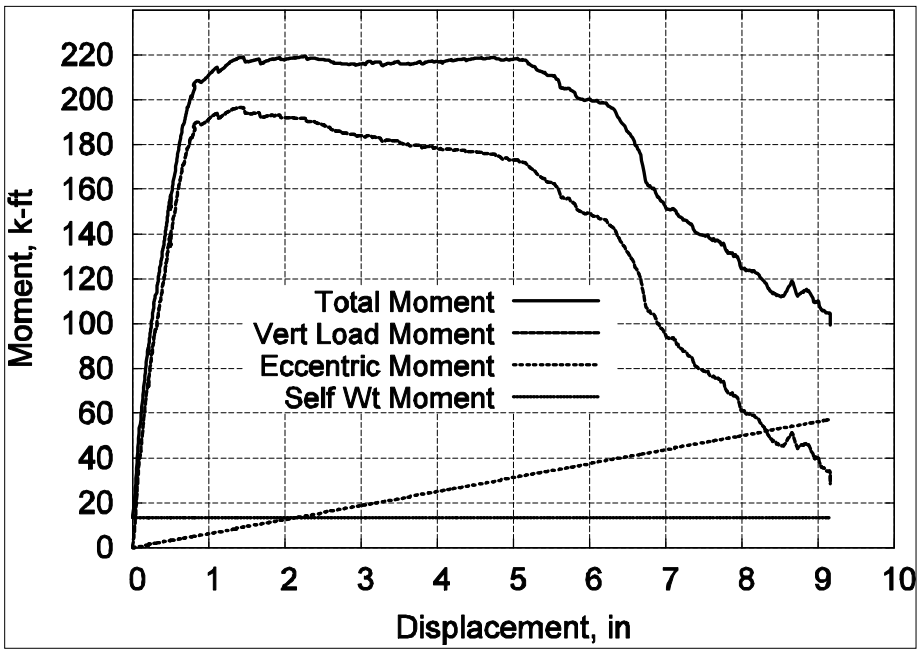

Figure 1-74 M **vs. mid-span deflection for FC specimen**

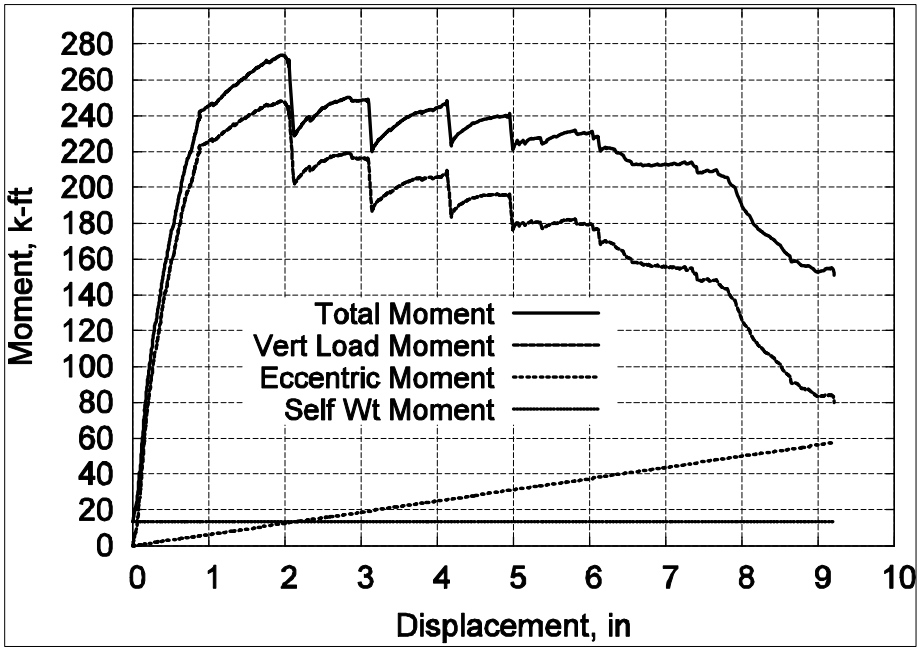

Figure 1-75 M **vs. mid-span deflection for FR specimen**

1.7.3 Comparison of specimen strengths and stiffness

To compare the ultimate bending capacities developed by the specimens with the values predicted by the moment-curvature analyses, we had to first identify the locations of the sections where failure actually occurred in each specimen.

The critical failure of the AC specimen was exactly at midspan. Therefore, the maximum moment shown in Figure 1-72 was considered to be the ultimate moment capacity of the specimen.

The failure section of the AR specimen was identified to be at the location where the tension Fibrwrap ruptured, which was approximately 9.5" away from midspan. Measurements made of the specimen after the test revealed a reduction in the amount of tension Fibrwrap at this location from the specified 7.5" width down to a width of approximately 6.625" because of a construction problem.

The failure section of the FC specimen, as described in Section 1.6, was located approximately 8" away from the face of the central block. This was probably due to the confining effect of the large block on the adjacent concrete.

The failure section of the FR specimen was somewhere between the face of the central block and a point 6" to 8" away, similar to the FC specimen. The Leadline did not necessary have a peak stress immediately adjacent to the central block. Before the Leadline experienced total bond failure, there could have been a region of maximum Leadline stress extending to at least a few inches away from the central block. The deepest concrete spalling occurred at about 8" away from the central block, similar to the FC specimen. However, the first transverse hoop to rupture was adjacent to the central block, which indicates that the failure section was closer than 8" away from the block. The failure section was thus estimated to be approximately 4" away from the central block.

The maximum bending moments at the failure sections identified above are compared to the predicted moment capacities from moment-curvature analyses. The analysis was based on the tested material strengths of the concrete, shotcrete, and steel presented in Section 1.5. In the test of the AR specimen, the average tensile strain in the longitudinal Fibrwrap at rupture was measured to be 0.0077 instead of the value recommended by the manufacturer. Thus, in this analysis, the Fibrwrap was considered to have a tensile strength of 81 ksi, which is equal to the product of the measured ultimate strain and the specified Young's modulus of the Fibrwrap. The average tensile strain in the Leadline at pullout was 0.0096 from the test of the FR specimen. Thus, the Leadline was considered to have a tensile pullout strength of 205 ksi, which is equal to the product of the measured ultimate strain and the specified Young's modulus of the Leadline. Typically, the Fibrwrap in compression experienced buckling at a strain of about 0.002. The Leadline buckling could not be observed due to the concrete cover, but it was assumed to fail at a compressive strain of 0.002 as well. This is probably a conservative estimate since the concrete would provide some confinement at higher strains. The Leadline and Fibrwrap were assumed to have the same axial stiffness in compression as in tension, though this information was not provided by the manufacturers.

The maximum bending moments are presented in Table 1-8. The calculation details are presented in Appendix B.

Table 1-8 Comparison of predicted strengths and actual strengths for specimens

Specimen	**Compressive axial load, *kips***	**M_n from M-κ analysis, *k-ft***	**M_u from test data, *k-ft***	$\frac{M_u - M_n}{M_u}$
AC	30	59	62	4.8%
AR	30	74	76	2.6%
FC	75	198	203	2.5%
FR	75	255	264	3.4%

For both sets of specimens, the strength of the retrofitted specimens was significantly higher that that of the control specimens. Due to the FRP strengthening, the ultimate moment capacities of the AR and FR specimens increased by 22% and 30%, respectively.

Figure 1-76 shows a comparison of the mid-span moment M vs. Δ for the AC and AR specimens. Figure 1-77 shows a similar comparison of the FC and FR specimens.

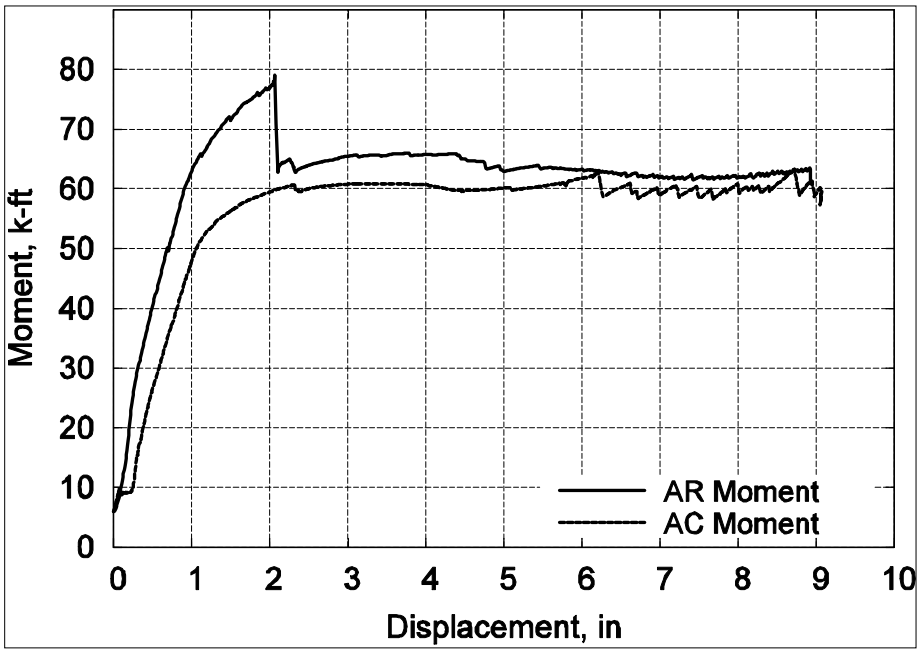

Figure 1-76 M vs. mid-span deflection for arch specimens

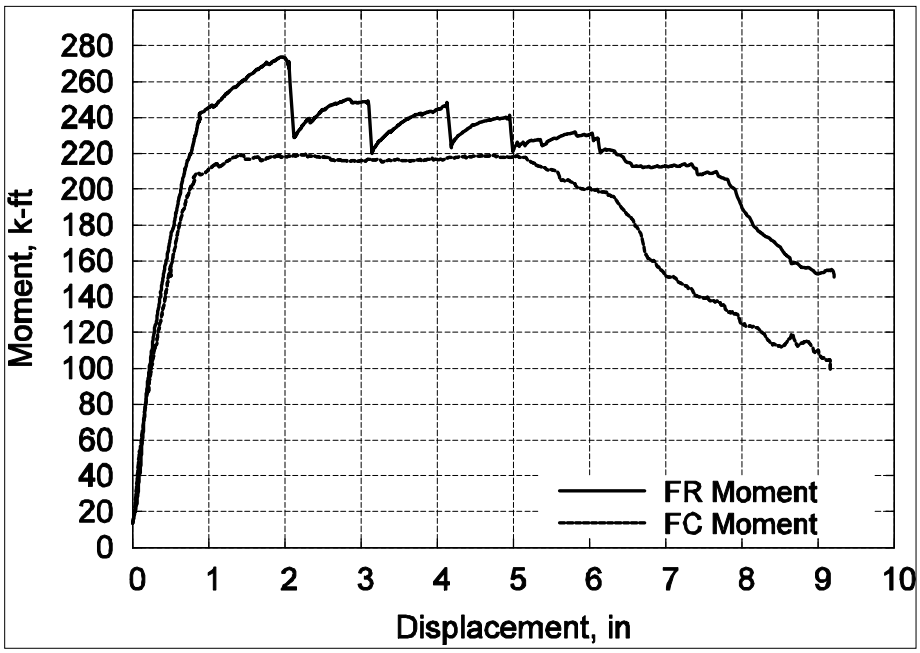

Figure 1-77 M **vs. mid-span deflection for arch-foundation specimens**

The axial load-moment strength interaction diagrams for the test specimens calculated based on measured material properties are shown in Figure 1-78 and Figure 1-79. Each diagram presents the strengths of the control specimen, labeled "Unstrengthened", and the retrofitted specimen, labeled "Strengthened". The strength difference between the AC and AR specimens diminishes as the axial load increases, as seen in Figure 1-78. This is due to the decrease in compression steel reinforcement in the AR specimen, which cancels the strength increase caused by the FRP confinement. Conversely, the FR specimen remains stronger than the FC specimen at high axial loads, as seen in Figure 1-79. There are two reasons for this: the reduction of compression steel area in the FR specimen is not as significant as for the AR specimen, and a layer of higher-strength shotcrete is placed around the perimeter of the FR specimen.

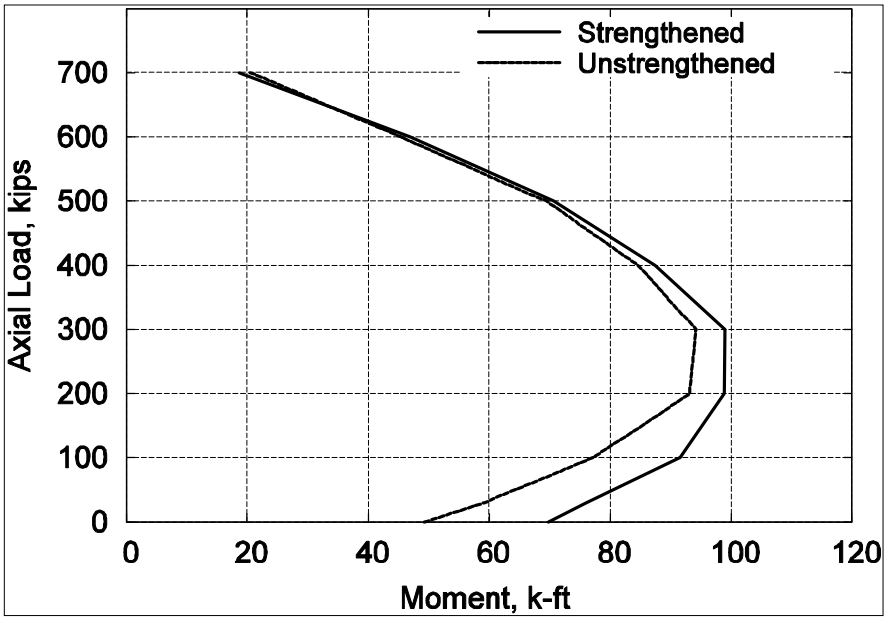

Figure 1-78 Axial load-moment strength interaction diagram for AC and AR specimens

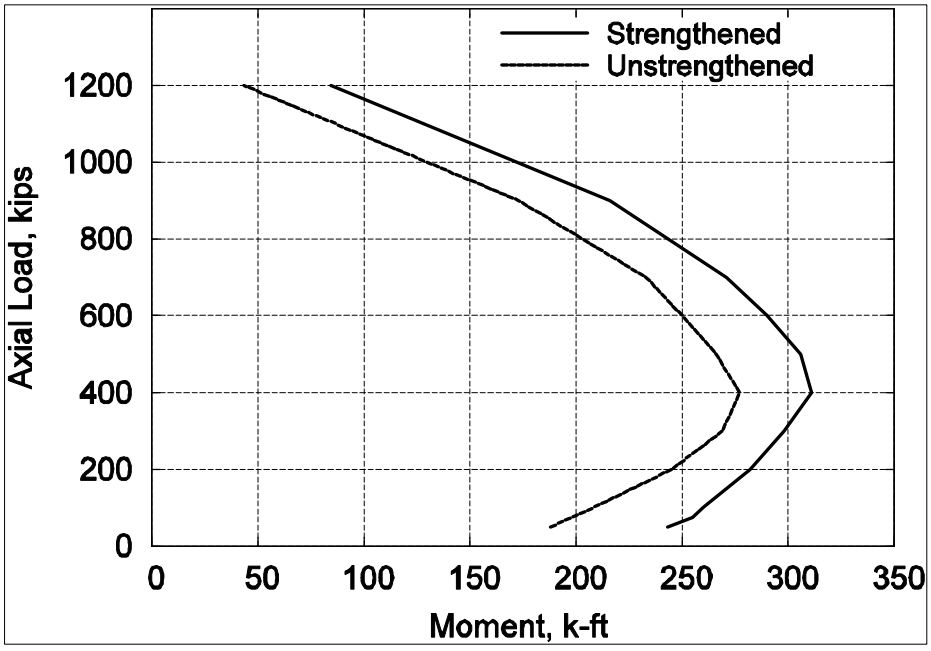

Figure 1-79 Axial load-moment strength interaction diagram for FC and FR specimens

1.7.4 Moment-curvature results

The plots of internal moments vs. section curvatures are shown in Figure 1-80 through Figure 1-83. The moments were calculated at the sections where the strain gages were

located. The curvatures were calculated by Equation (1.38) using selected strain gages. Gages were chosen from locations that appeared to be closest to tensile cracks as will be explained further below.

For the curvatures computed from the rebar strains, gages were chosen at sections that contained tension bars that exhibited yielding at the lowest bending moment. Curvatures computed from other rebars were closer to the predicted values, but these gages were more likely located away from a crack. In general, the $M-\kappa$ plots based on the steel strains followed the predicted curve fairly well until the bars yielded. After yielding, these curvatures increased rapidly until the gages were damaged and the curvature plots terminated. The prediction model was based on the assumption that plane sections remained plain under a bending load, but this would no longer be the case after the tensile cracks began to widen and bond slips occurred. Therefore, the $M-\kappa$ plots based on the steel strains were not expected to agree with the predicted $M-\kappa$ plots after the onset of steel yielding.

The strain data from the Leadline and the Fibrwrap was much more uniform than the strain data from the steel due to the linear elastic behavior of FRP. The choice of which gages to use to calculate the curvatures made little difference. Furthermore, some of the gages remained intact until the ultimate moment capacity of the section was reached. For the AR specimen, the $M-\kappa$ plot from the Fibrwrap strain extended to the rupture of the Fibrwrap. However, for the FR specimen, the $M-\kappa$ plot from the Leadline strain was terminated early due to damage to the concrete gages.

The $M-\kappa$ plots based on the FRP strains seemed to follow the theoretical $M-\kappa$ plots very well. No jumps or irregularities were recorded in the FRP strains before rupture or pullout, even when cracks formed in the concrete. For the FR specimen, the shotcrete layer might have begun separating from the rest of the specimen much earlier than observed. This could have caused debonding of the Leadline rods over a certain distance. Thus, the Leadline strain might not have been affected by the localized tension cracks in the member, and the Leadline gages would have measured the strain in the tension side of the specimen

in an average sense. A similar scenario could have been present in the AR specimen. If the tension cracks in the concrete near midspan initiated a fracture path which caused localized debonding of the tension Fibrwrap prior to rupture, then the gages on the Fibrwrap would have measured the tensile strain in an average sense as well. These bond failures are common in FRP reinforced flexural members (Teng et al. 2002). This initial localized debonding could have gone undetected in both tests.

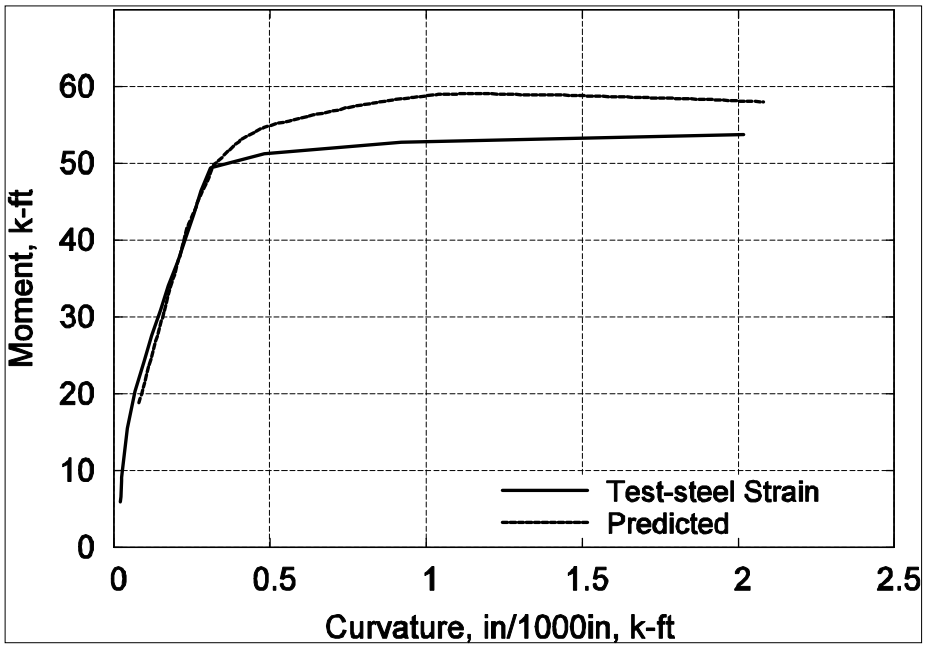

Figure 1-80 Comparison of M vs.κ plots for AC specimen

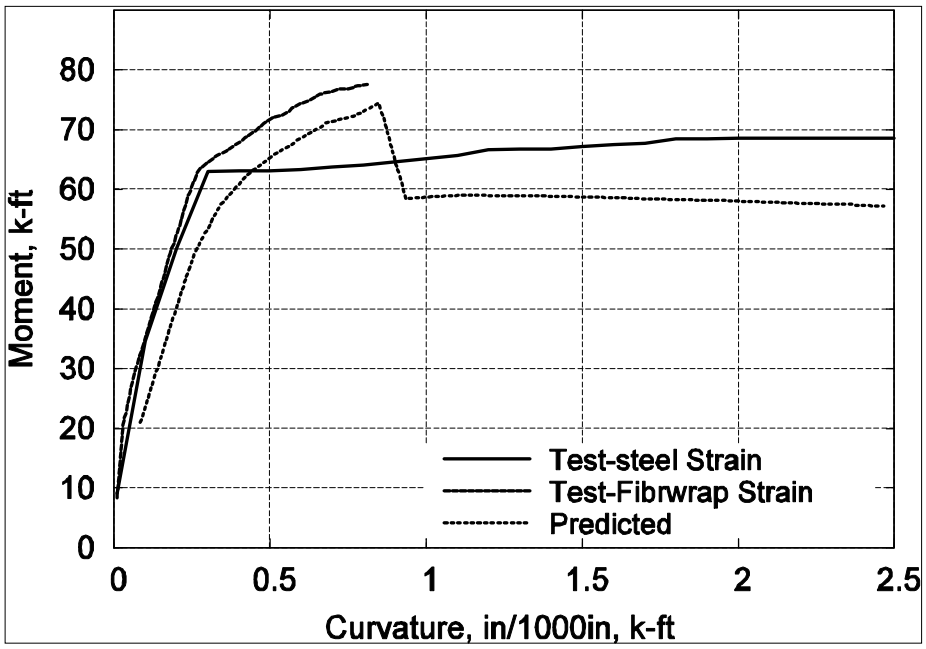

Figure 1-81 Comparison of M vs.κ plots for AR specimen

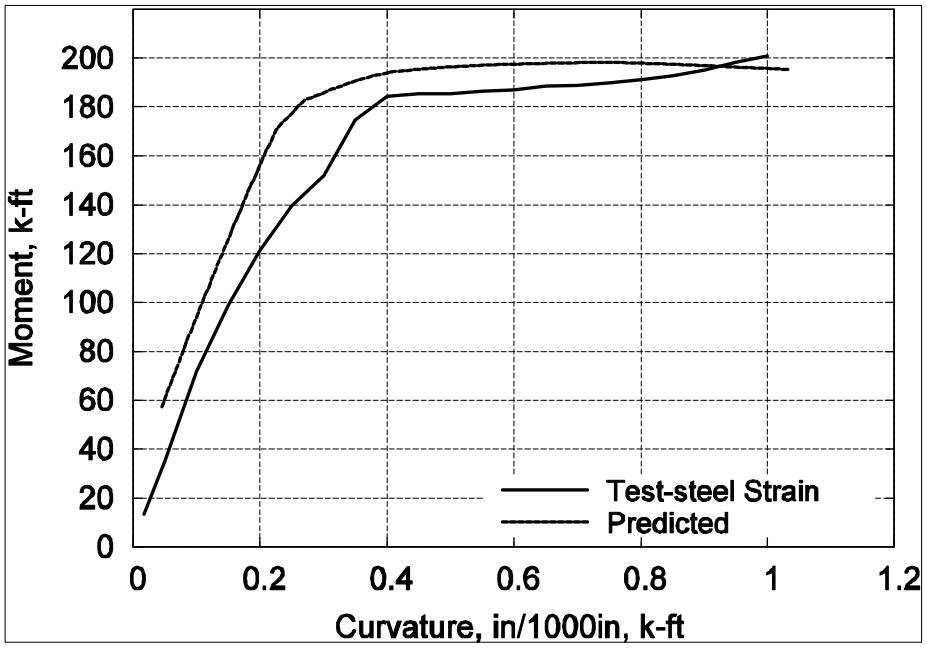

Figure 1-82 Comparison of M vs.κ plots for FC specimen

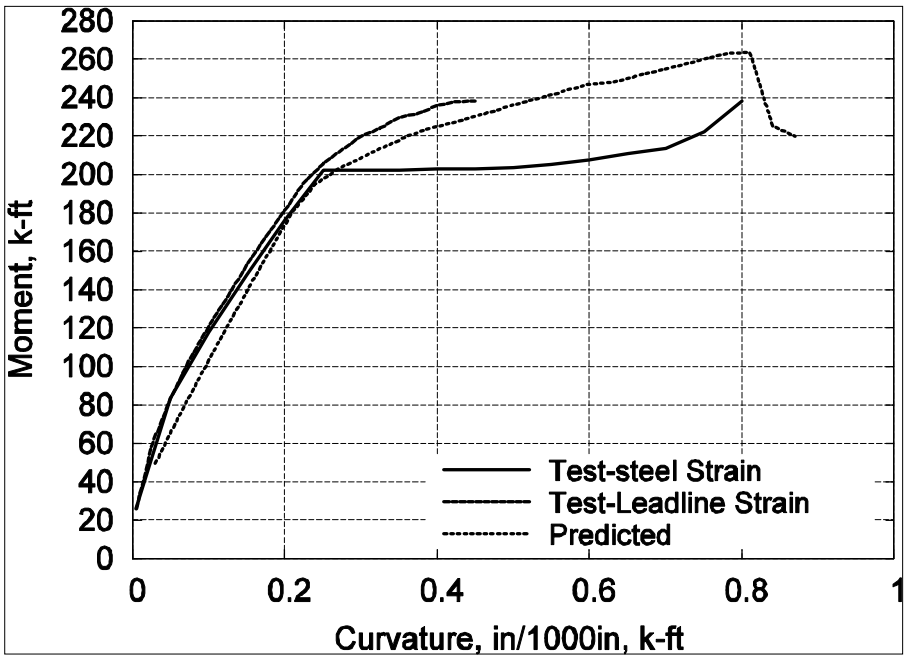

Figure 1-83 Comparison of M vs. κ plots for FR specimen

1.7.5 Predicted strength of the actual arches

In this section, the load-carrying capacity of the actual arches in the bridge are evaluated using the test results and analytical models. To this end, the axial load-moment interaction diagrams were recomputed based on the actual material strengths presented in Section 1.5 and the experimentally observed behavior of the specimens as described previously.

The axial load-moment interaction diagrams for arch sections at the third column and near a foundation block are shown in Figure 1-84 and Figure 1-85. In these figures, the curves labeled "Nominal" were computed for the FRP retrofitted specimens using the nominal material properties given in Section 1.2, the minimum strengths were computed using the ultimate tensile strength of 81 ksi for the Fibrwrap and 205 ksi for the Leadline as mentioned above, and the curves labeled "Unstrengthened" were computed using the nominal material properties without considering FRP strengthening. Finally, the lines labeled "DL Axial Force" represent the axial load in the sections due to the self-weight of the bridge as found in the SAP2000 arch analysis presented in Section 1.4.

As shown in Figure 1-84, the strength of the arch section at the third column is affected much more by the FRP retrofit in the tension-controlled region than in the compression-controlled region of the interaction diagram. There are two reasons for this. First, the analysis assumed no shotcrete around the arches at this location, so concrete strengths in the section before and after the retrofit were the same. Secondly, the ratio of the confining Fibrwrap to the concrete was relatively small as only alternate straps were wrapped completely around the arch ribs.

The strength of the arch section near a foundation block is significantly strengthened for the entire range of the axial load-to-bending moment ratio, as seen in Figure 1-85. This is due partly to the confining effect of the full wraps around the very base of the arch. It is also due to the application of shotcrete which is stronger than the original arch concrete.

The strengthening effect of the retrofit was estimated using the simple arch-rib SAP2000 model described in Section 1.4 and the predicted retrofitted arch strengths. This was approached as described in Section 1.4 for the unstrengthened arch. The strength-interaction diagrams used are the curves labeled “Minimum” in Figure 1-84 and Figure 1-85. The ultimate moment in the arch under the third column occurred under a concentrated load of 430 kips. The axial force and moment under this loading were 2780 kips and 5160 kip-ft, respectively. The ultimate moment in the arch-foundation connection occurred under a concentrated load of 735 kips located at above the second column. The axial force and moment under at the arch bases under this loading were 3880 kips and 13188 kip-ft, respectively.

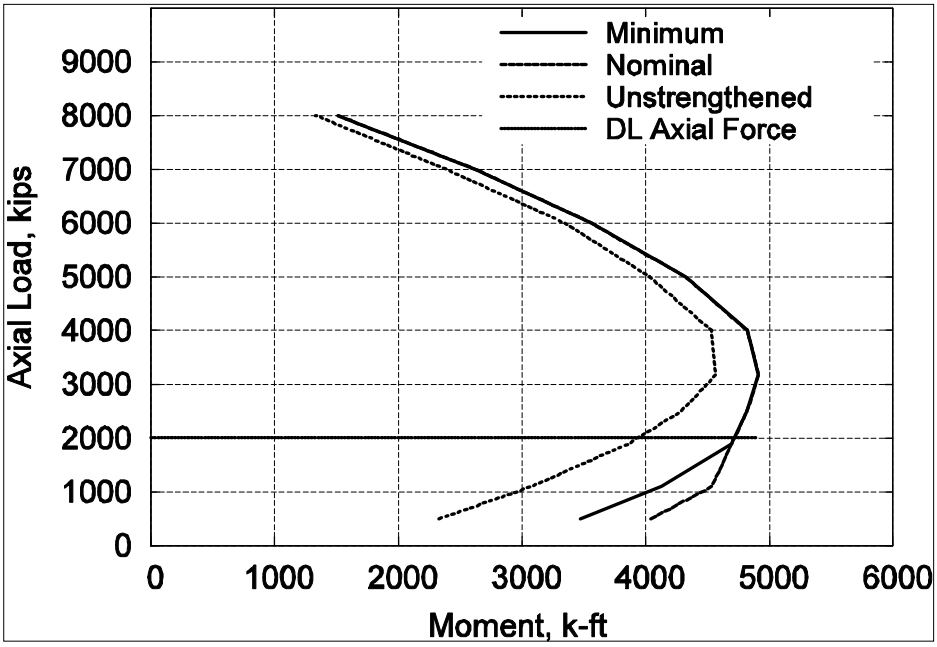

Figure 1-84 Axial load-moment interaction diagrams for arch at third column subjected to positive bending

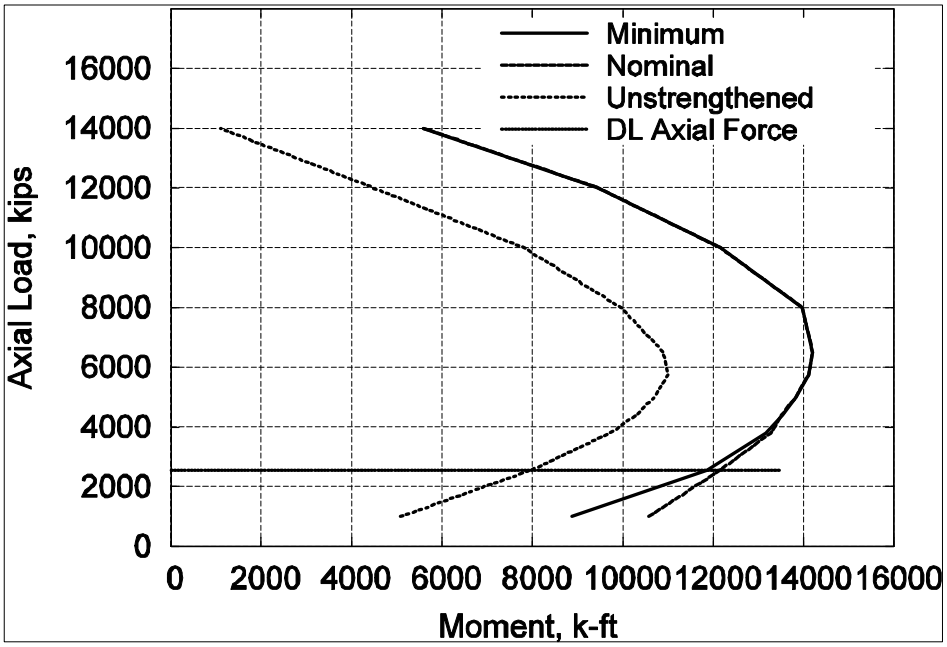

Figure 1-85 Axial load-moment interaction diagrams for arch-foundation connection subjected to negative bending

1.8 Summary

This study evaluates the strength of the arch ribs in the Castlewood Canyon Bridge which were retrofitted with externally bonded CFRP fabric and CFRP rods. Four quarter-scale beams were tested to model the arch ribs before and after the retrofit. Two of the beams were modeled after the arch regions underneath the third spandrel columns in order to evaluate the behavior of an arch rib below a heavily loaded column. The remaining two beams were modeled after the arch-foundation moment connections.

Two of the beams were control beams and the other two were strengthened with FRP. Of the two beams that were strengthened with FRP, one was strengthened with a scheme similar to that used around the spandrel column-arch rib connections. This was accomplished using Fibrwrap, an externally bonded CFRP fabric. The other was wrapped with Fibrwrap and reinforced with CFRP Leadline rods in a scheme similar to that used in the actual arch-foundation connections.

The beams were simply supported and tested to failure under a combination of axial load and bending moment. The test results were used to calibrate analytical models which were used later on to evaluate the strength of the arch ribs in the actual bridge before and after retrofit.

The conclusions of this chapter are as follows:

1. The retrofitted test specimens were between 22% and 30% stronger in bending than the control specimens. The greater strength increase was for the arch-foundation connection specimen. The stiffness of the specimens was also slightly increased by the FRP. The retrofitted specimens lost strength after the FRP rupture or bond failure. However, they still exhibited higher strengths than the control specimens throughout the tests.
2. Structural analyses indicate that the bridge arches are much stronger than necessary to meet the required traffic loads. The retrofitting scheme increased the strength of the arches significantly. Based on the SAP2000 analysis described in Section 1.4,

the strength of the arch to resist a concentrated load on the third spandrel column was increased by 30% compared to the original arch (prior to retrofit). The strength of the arch-foundation section to resist a concentrated load over the second spandrel column was increased by 32%. These increased strengths are due primarily to the transverse FRP wraps which enhance the compressive behavior of the concrete. These values come from a very simple analysis of the arch and are intended to obtain some qualitative idea of how the increased arch strengths may affect the maximum live loads on the arch.

3. The retrofitted arch specimen failed by rupture of the tension Fibrwrap. The average maximum FRP strain reached was 0.0077. This is only 63% of the ultimate strain specified by the manufacturer. In other beam tests, the rupture strain of Fibrwrap in was typically at least 0.01 (personal communication with the manufacturer, 2004). The cause of this premature rupture is unknown.

4. The retrofitted arch-foundation specimen failed due to the peeling of the concrete cover by the lower Fibrwrap in tension, which in turn led to pullout of the Leadline dowels. This peeling effect is common in FRP reinforced RC members and is due to stress concentrations at the end of the Fibrwrap (Teng et al., 2002). This caused a separation of the lower shotcrete from the rest of the specimen along the plane where the Leadline was developed. As this debonding progressed, the effective Leadline development length was shortened. Soon after the Leadline pulled out, the transverse Fibrwrap ruptured along the fracture between the shotcrete and the concrete. Increasing the amount of transverse Fibrwrap might help to prevent or delay this bond failure. However, it would probably be better to avoid terminating all of the Fibrwrap at, especially in a region of high moment. One possible solution might be to extend the Leadline rods farther into the arch and begin the longitudinal Fibrwrap at a point of lesser moment if there is such a place along the arch.

CHAPTER 2 DURABILITY OF BOND STRENGTH OF CARBON FIBER REINFORCED POLYMER SHEETS

2.1 Introduction

According to recent Federal Highway Administration estimates, repairs for corrosion damage to federal bridges are estimated at $50 billion annually and nearly 35% of all bridges are either structurally or functionally deficient. New construction for replacing deficient structures may not be applicable and economically viable because of the high cost and substantial traffic disturbance. Emphasis is being placed on the development of newer, more efficient and more cost effective methods of repair and strengthening for civil infrastructures. Repair and strengthening of reinforced concrete (RC) structures using advanced fiber-reinforced polymer (FRP) composites have become very popular because the use of FRPs provides an attractive alternative to traditional rehabilitation techniques. The installation of these light-weight materials is less labor and equipment intensive. The main advantages of FRPs are its high strength and non-corrosive features.

One of the methods that have been used to strengthen existing concrete structures is the application of FRP sheets wrapping around concrete structural components. The performance of the FRP strengthened structures depends on the bond strength of adhesives between the wrap and the concrete surface. The adhesive deteriorates due to long-term environmental exposure. Much research has been done on mechanical properties of FRP bond. However, the research on long-term durability of the bond is very limited (Toutanji and Balaguru 1999; Karbhari et. al., 2000a; b). Apparently, it is very important to evaluate the durability of the repairing systems in order to ensure that the repaired structures can serve reliably for a long time.

One of the objectives of this study was to assess the durability of the bond. To this end, Castlewood Canyon Bridge was selected, and carbon FRP wrapping was used as the repair

method for the concrete arch of the bridge, and various influencing parameters were examined to investigate the deterioration of the bond strength of carbon FRP wrapping in the service environment.

2.2 Background

In 1946, the Castlewood Canyon Bridge was built in Castlewood Canyon, Franktown, Colorado. The bridge is on State Highway 83 through traffic between Franktown and Colorado Springs.

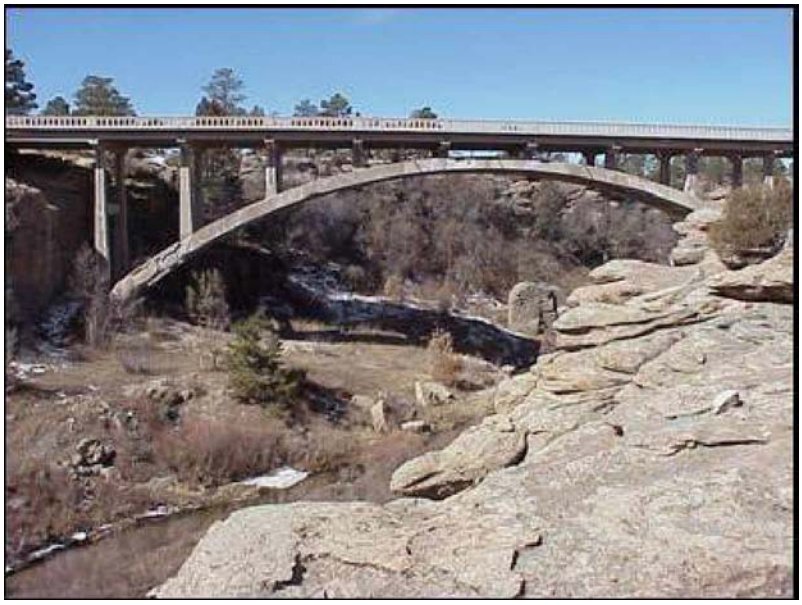

Figure 2-1 Bridge view before repair

This fifty-seven year old bridge had experienced very severe cracking and other distress due to a variety of reasons that it needed a complete rehabilitation. Figure 2-1 shows the bridge before the repair work started. The concrete of the arch and the column had spalling due to the severe corrosion, overstressing, fatigue related cracking etc., shown in Figure 2-2, Figure 2-3 and Figure 2-4.

Figure 2-2 The corrosion-induced spalling in the spandrel column

Figure 2-3 The damaged arch due to corrosion

Figure 2-4 The corrosion in arch

It was imperative that the bridge be repaired. In 2003, the arch of the bridge was first strengthened by wrapping it with Carbon Fiber Reinforced Polymer (CFRP) sheets. To expedite the rehabilitation process, an innovating splicing systems was employed; the concrete deck, girders and spandrel columns were systematically removed and replaced with precast decks, precast girders, precast spandrel columns and precast pier-caps. It was

necessary to stage the demolition and reconstruction work carefully so as not to damage the arch ribs due to excessive unbalanced loads.

The repaired bridge, which was reopened to traffic on October 4, 2003, is shown in Figure 2-5. Systematic tests were performed to assess the durability of the bond between concrete-FRP interface when exposed to several environmental conditions.

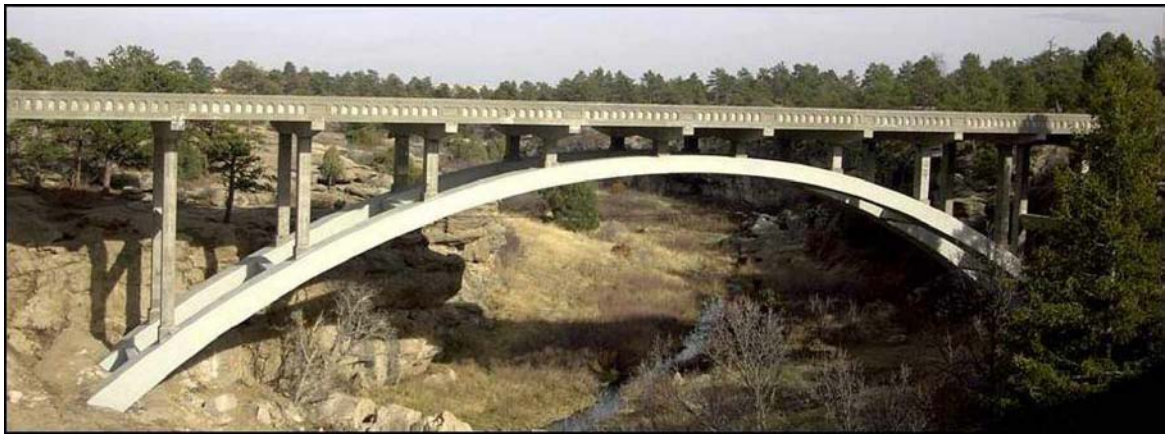

Figure 2-5 Repaired Castlewood Canyon Bridge, Franktown, Colorado

2.3 Strengthening RC Structures Using FRP

FRP composites with higher strength, higher stiffness, and lower density were very expensive in the 1960s and 1970s. However, by the late 1980s and 1990s the cost of FRP started to decline due partly to the technological improvement of the FRP industry and partly to the growth of the market and the public's increasing expectations in terms of infrastructure's quality. The conventional methods for strengthening RC structure damage due to impact or corrosion are steel plate bonding and shotcreting. These techniques have suffered from the deterioration of the bond at the steel-concrete interface caused by the corrosion of steel. Alternatively, FRPs do not have the corrosion problem. FRPs are

combinations of polymer matrix and various types of fibers. A number of different techniques exist for the application of glass, carbon, and aramid fibers, in the form of fiber tow, fabric, and even prefabricated shells, providing confinement against the dilation of concrete and in effect increasing the strength and ductility of RC structural members (Seible and Karbhari 1997). Fiber sheets are impregnated on-site with a saturating resin. The saturating resin is used to provide a binding matrix for the fibers and bond the sheets to the concrete surface. Wet lay-up systems are saturated with resin and cured in place and are therefore analogous to cast-in-place concrete. The procedure for the wet lay-up system is explained below.

Wet-Lay up Installation of FRP Sheet

1. Substrate preparation: The surface of the concrete must be sound, clean, and suitably roughened prior to bonding. There should be no spalling or delamination. The edges must be ground to a minimum radius of 10mm (3/8in). Any unevenness in the concrete is removed with detergent scrubbing, low pressure water cleaning, acid etching, grinding, sandblasting, high-pressure water jetting and mineral-based re-profiling mortar.
2. Prime Concrete Surface: The dust-free surface is coated with a primer.

Figure 2-6 Epoxy undercoating in progress

3. Apply Epoxy (Undercoating): To saturate the sheet and simplify installation, the adhesive/matrix resin is applied to the front and back of the material. Epoxy is mixed and applied onto the surface using a roller or brush (see Figure 2-6). Once material has been wet-out with the liquid resin, the material may be rolled for ease of transport and/or application to the place of application.
4. Place FRP sheet on Structure: Sheet rolls are unrolled onto the structural element being strengthened (see Figure 2-7). Tension is maintained to minimize intrusion of air entrainment behind sheet. Placing one layer at a time, pressure is applied to wrap using a roller. A hard rubber roller with ridges (air relief roller) works well for this application.

Figure 2-7 Placing CFRP sheet on concrete in progress

Figure 2-8 Epoxy overcoating in progress

5. Apply epoxy to sheet surfaces (Overcoating): A top coat of epoxy can now be applied to the sheet to fully saturate the material (see Figure 2-8).
6. Finishing and Painting (see Figure 2-9).

Figure 2-9 Finishing

2.4 Influential Parameters for Durability of the Bond between CFRP Sheet and Substrate

The influence of environmental factors on the degradation of the bond strength between FRP and substrate is of great concern during applications. The FRP bond strength may be deteriorated by environmental factors through mechanism illustrated by Figure 2-10.

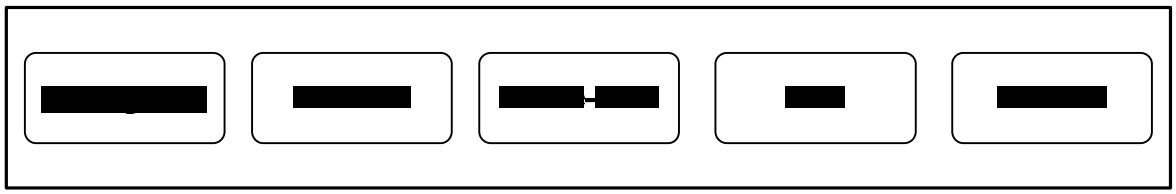

Figure 2-10 FRP bond strength deterioration modes

From cycling environmental exposure, resin cracking strain may develop. Then, fluids can penetrate into the material and accelerate the irreversible chemical reaction that may eventually cause the degradation in the properties of FRP bonding. During the service life of a FRP repaired structure, FRP wrapping encounters many environmental parameters that

can result in severe deterioration. For example, FPR sheets are in direct contact with high pH concrete and exposed to harsh environmental conditions such as elevated temperatures, temperature fluctuations, high humidity levels during rain and snow, corrosive fluids as a result of the use of deicing salts, and freeze-thaw conditions. In this Section, we will provide a literature review on the current status of the research, and identify several major influential parameters for the detailed experimental study.

2.4.1 Freeze-thaw effects

FRP materials are subjected to freeze-thaw cycles in cold region environments. The durability of FRP sheets's bond strength in the low temperature environment is a critical issue. Experimental results on FRP wrapped concrete cylinders exhibited more catastrophic failure after exposure to the freeze/thaw cycles than in other environments (Toutanji and Balaguru 1998).

The thermal expansion of CFRP sheets is only one tenth that of concrete. This difference in thermal expansion induces thermal stresses that may cause deterioration of the repair system. In fact, microcracks and voids in the polymer matrix can occur during a freeze-thaw cycling due to the mismatch of the coefficients of thermal expansion. Thermal fatigue can be induced between the fibers and matrix because of the mismatch and the appearance of cracks (Tannous and Saadatmanesh 1998).

2.4.2 Moisture susceptibility effects

FRP composite components used in civil infrastructure are exposed to rain, humidity, moisture, or diffused solutions through other substrates such as concrete. The FPR components may even be immersed in aqueous solutions that could have ponding or overflow in times of heavy rain or snow.

Mallick (1993) reported that polymer matrix composites absorb moisture by the diffusion through matrix. On the other hand, water absorption causes changes in resin properties and results in swelling and warping in composites (Karbhri et al., 1996).

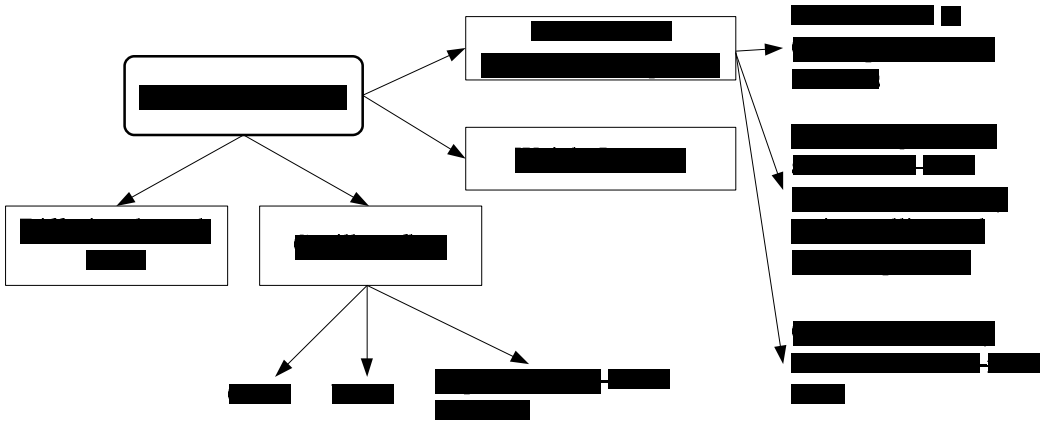

Figure 2-11 Degradation modes due to moisture absorption on FRP (Karbhri et al., 1996; Homan 2000)

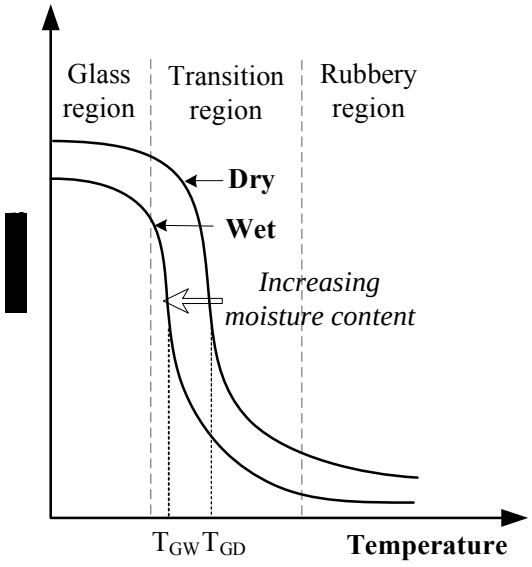

Figure 2-12 Variation of stiffness with temperature for a typical polymer showing the glass transition temperature

The primary effect of the moisture absorption is on the resin itself through some mechanisms like hydrolysis, plasticization, and saponification, which cause both reversible and irreversible changes in the polymer structure (see Figure 2-11). Figure 2-12 shows that the stiffness changes depend on the moisture content in the general polymer materials. The more moisture absorbed, the lower the stiffness of the polymer.

Jones (1999) and Shen et al. (1976) stated that moisture diffusion into an epoxy matrix and the susceptibility of the fibers to water can cause changes in thermophysical, mechanical and chemical characteristics of FRPs. Moisture in the resin weakens the Van der Walls force between the polymer chains and results in a significant degradation of bond strength. The swelling stress induced by the moisture uptake can also cause matrix cracking and fiber-matrix debonding (Hayes et al., 1998).

Mayes et al. (1992) reported that epoxy adhesives are prone to water absorption because they possess polar sites that attract water molecules. Although the absorption of limited amounts of water can be regarded as beneficial in terms of improved toughness and static fatigue resistance, it is generally considered harmful. The water acts as a plasticizer, causing changes in stiffness and glass transition temperature (Shaw 1994).

Malvar et al. (2003) stated that moisture is of concern because water vapor competes with the polyamine or polyamide (part B) to react with the phenolic ether (part A) that forms an epoxy adhesive. The reaction of water, rather than the polyamide, with the phenolic ether will reduce the overall strength of the resultant epoxy adhesive (Novinson 1983). Therefore, epoxy mixing and application are often not allowed if rainfall, dew, or humidity in excess of 85% is present (Warren 1998 2000).

2.4.3 Deicing salt effects

Large amounts of deicing salts are used on bridges during the winter season to control snow and ice. The general impression is that solution of deicing chemical can trigger damage in the resin matrix by diffusing into the resin matrix. But, no systematic research has been reported on the effect.

2.4.4 Alkali effects

During FRP wrapping repair, FRP sheets will be embedded, be bonded to, or be placed adjacent to concrete. Sometimes, FRP sheets will have concrete encapsulated within. Concrete is known to have a pore water with pH level as high as 13.5. The alkaline solutions and ions in pores can cause severe degradation to the polymer systems. The properties of polymers may deteriorate significantly in concrete environments because of the alkali attack, and because of the growth of hydration products between individual filaments (Murphy et al., 1999). The durability of the bond between FRP and concrete in the alkaline environment is another critical issue, which depends on resin types and manufacturing processes. Furthermore, a number of other materials with high alkaline contents could come in contact with FRP, such as soil. The determination of the durability of FRP composite systems in contact with alkali solutions is an essential task.

2.5 Experimental Plan

2.5.1 Specimen preparation

Two types of concrete mix designs were used in the study. One was a regular concrete, and the other was a shotcrete. The regular concrete specimens were designed for testing the bond strength of carbon FRP applied on conventional concrete structures, and the shotcrete specimens were tested in the present study mainly because it was used on Castlewood Canyon Bridge between the existing concrete and carbon FRP thin sheets. The mix designs

for the shotcrete and concrete are shown in Table 2-1 and Table 2-2. The CFRP sheets were Tyfo SCH-41 Composite using Tyfo S Epoxy manufactured by FYFE Co. LLC.
The shape of the specimens was a square block as shown in Fig. 1-14. The dimension of shotcrete specimens is 12 in. x 12 in. x 3 in., and the dimension of concrete specimens is 10 in x 10 in. x 3 in. The top surface of the specimens was used for the bond test. The properties of Tyfo S epoxy are shown in Table 2-3 and Table 2-4.

Mountain Type I/II	652.00 lbs
ISG Type F Fly Ash	100.00 lbs
Master Builders Silica Fume	25.00 lbs
#8 Pea Gravel-Agg. Ind.	687.00 lbs
MB VR Air Entraining Admixture	5.00 ozs
Glenium 3030	50.00 ozs
Sand	2008.00 lbs
Water	310.00 lbs
Water Cement Ratio	0.40

Table 2-1 The mixture design of shotcrete

Cement	700 lbs/yd3s
Water Reducer Agent	16 oz/cwt
Fine aggregate	1360 lbs
Coarse aggregate	1440 lbs
Water	295 lbs

Table 2-2 The mixture design of concrete

Tensile strength	127 ksi
Elongation at Break	1.2 %
Tensile modulus	10,500 ksi
Laminate thickness	0.04 in

Table 2-3 Properties of composites gross laminate (Tyfo SCH 41 Composite)

Tensile strength	10.5 ksi
Tensile modulus	461 ksi
Elongation percent	5.0 %
Flexural strength	17.9 ksi
Flexural modulus	452 ksi

Table 2-4 Properties of composites gross laminate (Tyfo S Epoxy)

Figure 2-13 Tyfo SCH-41 roll sheet

Figure 2-14 Square block specimen

The thickness of the Tyfo SCH 41 is 0.04 inches per layer. It is a pure uni-directional composite with 100% of the carbon fiber in one direction. The tensile modulus of the composite used for the project was 10,000 ksi. The coefficient of thermal expansion in the transverse direction is estimated to be approximately 37 ppm/deg F.

To glue CFRP sheets on substrate, wet lay-up bonded procedure was used. The CFRP sheets were impregnated with a resin during placement. A uniaxial CFRP tow sheet was bonded to the concrete/shotcrete using an epoxy that was impregnated with a resin during placement. The resin serves the dual purpose of impregnating and bonding the fibers together and bonding the composites to the concrete surface. A specimen with the CFRP sheet bonded on its top surface is shown in Figure 2-14.

In addition to the two different types of concrete used in the project (i.e. the concrete and the shotcrete mixes), a special corrosion inhibitor developed by Sika Corp., called Sika FerroGard 903 was used in the shotcrete. The purpose of using this corrosion inhibitor was to enhance the capacity of the corrosion protection of the new shotcrete and FRP wrapping system. On the other hand, there was a concern on the effect of the corrosion inhibitor on bond strength of carbon FRP sheets. To examine the bond strength, two groups of specimens were used; the shotcrete treated by Sika FerroGard 903; and the shotcrete untreated.

The spray method used to repair the Castlewood Canyon Bridge was used in this study to apply Sica FerroGard 903 on the surface of concrete samples. The application rate was 100 sq. ft. per gallon and was applied with two separate coats every 200 sq. ft. per gallon each. Concrete surface preparation prior to application of SicaFerroGard 903 was done by pressure washing with water. The corrosion inhibitor penetrated the surface and then diffused in a vapor or liquid form to the steel reinforcing bars embedded in the concrete. It formed a protective layer on the steel surface to inhibit further chloride impregnation and carbonation of concrete. Table 2-5 shows the properties of Sika FerroGard 903. Based on the data sheet provided by Sika, FerroGard 903 penetrated at least 3 inches in 28 days. This was tested by the Secondary Neuron Mass Spectroscopy.

Density	1.13 (9.4 lbs./gal.)
pH	11 (±1)
viscosity	15 cps
Color	Pale Yellow
Application Rate	100-150 ft^2/gal. total application rate

Table 2-5 Typical data for Sika FerroGard 903 at 73^oF

2.5.2 Conditioning of specimens

Prior to the testing of bond strength of the specimens, they were pretreated by various environmental conditions. This process, referred to as the conditioning of the specimens, was designed to generate similar deterioration of CFRP sheets as would be experienced in a service environment. Some specimens, however, were kept in standard laboratory curing conditions as control specimens and then were exposed to 26^oC and 40% RH. After the specimens were conditioned, the pull-off stress of the conditioned specimens were evaluated and compared to the specimens without the conditioning.

2.5.2.1 Freeze-thaw cycles

ASTM C666 (Standard Test Methods for Resistance of Concrete to Rapid Freezing Thawing) was used in the present study for the freeze-thaw conditioning of specimens, although the testing procedures specified by ASTM C666 were originally designed for the durability of concrete. An environmental chamber manufactured by Russells Technical Products was used for the freeze-thaw conditioning. It is shown in Figure 2-15. Based on ASTM C666 Procedure A (Rapid Freezing and Thawing in water), the specimens were subjected to a temperature variation ranging from 0°F(-29°C) to 40°F(20°C), with an one and half hour hold at 40°F and a two and half hour hold at 0°F until it was subjected to 300 cycles. Figure 2-16 shows the temperature cycles graphically for a 4.41-hour period. The specimens were exposed to 300 total freeze-thaw cycles (750 total hours of exposure).

Figure 2-15 The environment chamber used in the project

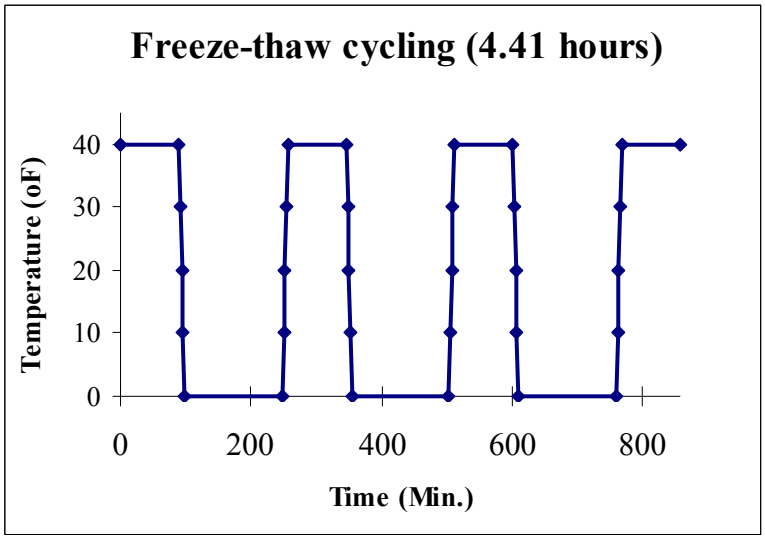

Figure 2-16 Freeze-thaw cycling program for a 4.41-hour period

2.5.2.2 Wetting in water

In order to investigate the effects of moisture susceptibility on the durability of bond strength, six specimens were immersed in water at room temperature for 90 days, as shown in Figure 2-17.

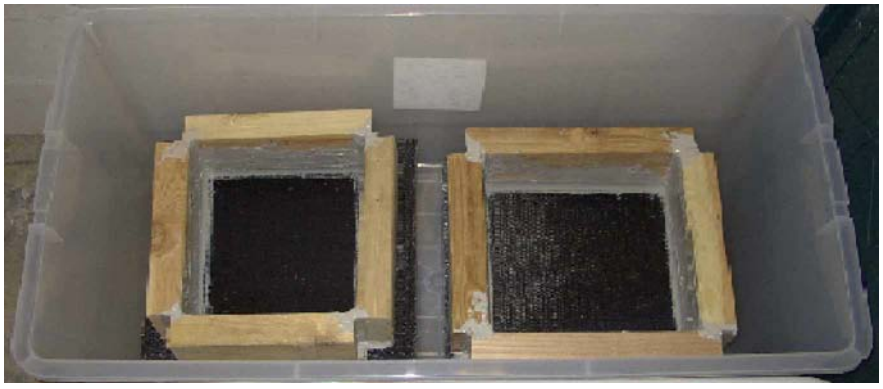

Figure 2-17 The ponded specimens in the bath

2.5.2.3 Wetting and drying cycles in water

In order to investigate the effects of wetting/drying cycles on the durability of bonded joints between CFRP sheets and concrete or shotcrete, six specimens are ponded in water at room temperature for seven days, and then allowed to air dry for seven days. The wetting/drying cycles were repeated over 90 days.

2.5.2.4 Deicing chemicals

The influence of deicing chemicals (sodium chloride, NaCl) on the bond strength was investigated by long-term ponding tests. In this project, 3% NaCl was used for the deicer solution. The ponding tests were continued at room temperature for 90 days, in the same manner as shown in Figure 2-17.

2.5.2.5 Alkaline attack

In order to investigate the effect of aqueous alkali on the bond strength, the specimens were exposed to 0.2M sodium hydroxide solution. Six specimens were ponded in the alkali solution of pH 12.5 and maintained at room temperature for 90 days in the same manner as shown in Figure 2-17. pH 12.5 was used in the test because it is close to the pH value of the pore solution in regular concrete.

The experimental parameters and specimen types are summarized in Figure 2-18.

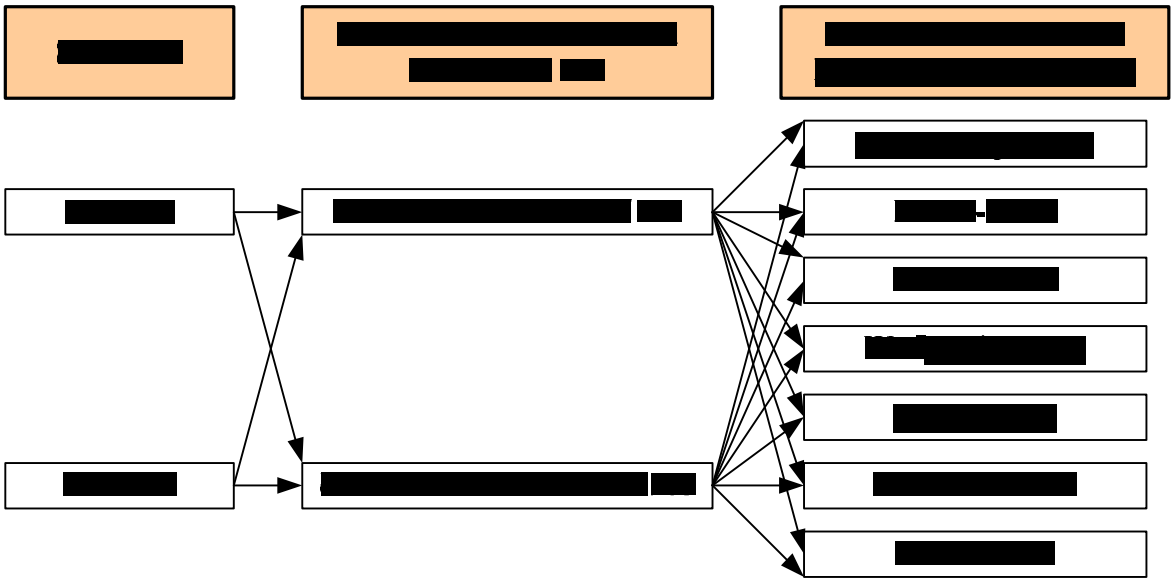

Figure 2-18 Schematic diagram for pull-off bond testing conditions

2.6 Direct Pull-Off Test

The tensile adhesion test was performed in accordance with ASTM D4541-89 (Standard Test Method of Pull-Off Strength of Coatings Using Portable Adhesion Testers). The fixed alignment adhesion tester, Elcometer 106 as shown in Figure 2-19 was used in the study. This test was specifically designed for estimating the adhesive strength of a coating to a substrate, and it was used in the project for determining CFRP bond strength. It was also used for evaluating concrete tensile strength and studying the effect of contamination on the adhesion of a coating to the surface (Beran 1998; Malvar et al., 2003).

Figure 2-19 The pull-off test apparatus

In an actual test, the test apparatus is attached to the loading fixture and aligned to apply lift off force perpendicular to the CFRP sheet surface. It is required to pull a small area of coating away from the base material. Before pulling off, a loading fixture was attached by adhesive to the CFRP sheet under examination. After curing, the CFRP sheet was cut through and the instrument claw engaged. The force was applied and recorded by means of a dragging indicator on an engaged scale. The indicator retains the value when the dolly and coating separate from the surface and is re-set prior to each test. The testing procedure follows in detail.

Experimental Procedures

1. The surface of the aluminum dolly (diameter: 0.787 in., area: 0.487 in^2) and the CFRP sheet were blasted to improve the bonding surface by roughening with abrasive paper, and then degreased by using a solvent to clean both surfaces with alcohol.
2. A small quantity of adhesive, 3M 1838 B/A Green, recommended by ASTM was mixed and applied with an even film to the conical end of the dolly.
3. The dolly was placed on the prepared test surface, and the excessive adhesive was removed. Then, the adhesive was allowed to cure overnight.
4. After curing, the CFRP sheet was needed to core drill down 3-6mm into the concrete substrate by means of an electric core bit. This gave the appearance of a small island of the specimens.
5. The instrument was placed over the dolly to ensure that it laid flat.
6. The hand wheel or nut of the adhesion tester was slackened. The dragging indicator on the scale was set to '0', and the claw with the dolly was carefully engaged.
7. The adhesion tester hand wheel/nut was rotated clockwise slowly and uniformly to apply a pull-off force to the test dolly. Until the CFRP sheet failed or dolly moved from the surface, it continued. The pull-off force could be read from the instrument barrel by observing the position of the dragging indicator.

8. Any pressure from the instrument springs created by rotating the adhesion tester hand wheel nut counter clockwise slowly was removed.

As the requirement of ASTM, a commercial epoxy adhesive (1838 B/A Green) supplied by 3M was used between FRP and dollies. The glass transition temperature (Tg) of the epoxy was higher than the standard room temperature (that is 23^{o}C). This implies that the mechanical and bond properties of the adhesive are affected little by temperature.

Color	Green
Shore D Hardness	80-85
Elongation	2-3%
Ultimate Tensile strength	4290 psi
Modulus of Elasticity	344,400 psi
Thermal conductivity (Btu/Hr/Ft2/oF/Ft)	.169
Coefficient of Thermal Expansion (in/in/^{o}C)	$79x10^{-6}$ between 32-40^{o}F (0-40^{o}C)
Glass Transition Temperature	131^{o}F

Table 2-6 Physical properties of 3M Scotch-Weld Epoxy Adhesive

Figure 2-20 View of pull-off testing in progress

2.6.1 Failure Modes

Causes of bond failure are divided into glue, adhesive, cohesive, substrate, or mixed failure.

1. Glue Failure – The tensile force exerted exceeds the strength of the adhesive used to attach the pull stub.

2. Adhesive Failure – A failure between two distinct layers or between the substrate and the first layer of coating.

3. Cohesive Failure – The adhesive layer breaks into two portions, one remaining attached to the substrate and the other attached to the dolly.

4. Substrate Failure – A breaking of concrete.

5. Mixed Failure – A cohesive and substrate failure simultaneously.

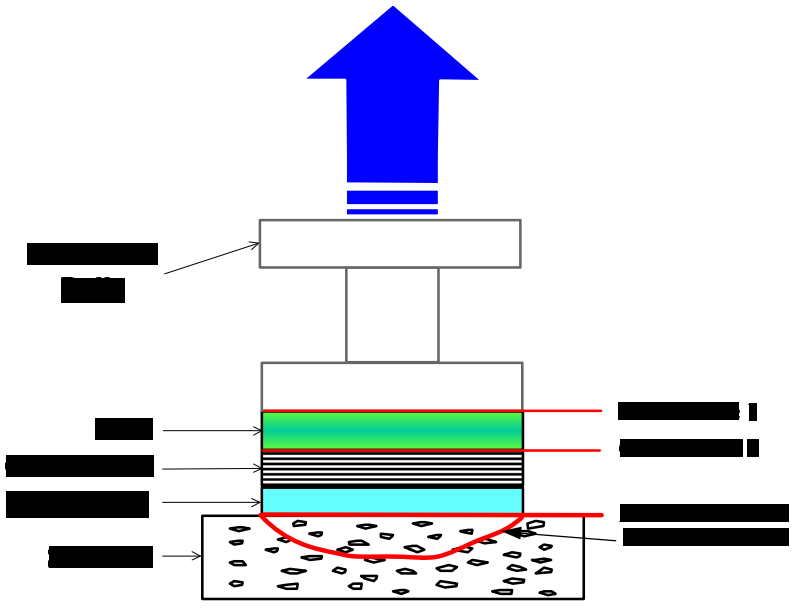

Figure 2-21 Types of failures

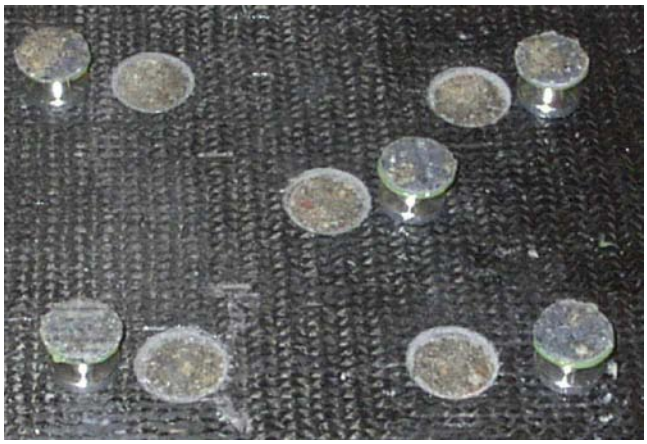

Figure 2-22 CFRP surface after a pull-off test

The tensile strength of the epoxy used between CFRP and the shotcrete is 10,500 psi based on the manufacturer's data sheet, and the tensile strength of the epoxy used to bond a circular aluminum dolly to CFRP surface is 4290 psi. The tensile strengths of the two epoxies are much higher than the tensile strength of the substrate shotcrete (210 psi). Therefore, the ideal failure mode should be the substrate fail in the shotcrete.

The ACI Committee 440 on FRP Reinforcement states that the minimum bond strength of 1.38 MPa (200 psi) is required and the substrate should fail (ACI 503R). The U.S. Navy has required both minimum bond strength of 2.07 MPa (300 psi), and failure in the substrate. Failure in the substrate is the most important requirement because the bond strength is a reflection of the concrete tensile strength. For this reason, repairing low strength concrete with FRP sheets or FRP laminates is not recommended if the concrete compressive strength is below 17.2 MPa (2,500 psi), corresponding to a tensile strength of about 1.7 MPa (250 psi) (Malvar et. al., 2003).

2.7 Experimental Results

2.7.1 Room temperature without any conditioning

1) Substrate: Shotcrete, Corrosion inhibitor: Applied

Average failure stress: 463 psi. (Standard deviation = 158 psi)

Failure mode: 9 mixed failures (mainly substrate failure, with some adhesive failure). In the case of mixed failure, the area ratio of substrate and adhesive failure was observed as 6.11:3.89, and the area ratio was estimated by visual observation (see Figure 2-23).

Figure 2-23 The mixed failure mode (substrate and adhesive failure)

2) Substrate: Shotcrete, Corrosion inhibitor: Unapplied

Average failure stress: 443 psi. (Standard deviation = 99 psi)

Failure mode: 1 cohesive failure and 7 mixed failures (mainly substrate failure, with some adhesive failure). In the case of mixed failure, the area ratio of substrate and adhesive failure was 6.00:4.00.

3) Substrate: Concrete, Corrosion inhibitor: Applied

Average failure stress: 494 psi. (Standard deviation = 193 psi).

Failure mode: 8 mixed failures (mainly substrate failure, with some adhesive failure). In the case of mixed failure, the area ratio of substrate and adhesive failure was observed as 6.00:4.00.

4) Substrate: Concrete, Corrosion inhibitor: Unapplied

Average failure stress: 588 psi. (Standard deviation = 155 psi)
Failure mode: 1 adhesive and 7 mixed failure (mainly substrate failure, with some adhesive failure). In the case of mixed failure, the area ratio of substrate and adhesive failure was observed as 6.29:3.71.

Pull-off strength of all samples exposed to room temperature was in excess of the 200 psi acceptance value.

2.7.2 Freeze-thaw

1) Substrate: Shotcrete, Corrosion inhibitor: Applied

Average failure stress: 365 psi. (Standard deviation = 89 psi)
Failure mode: 2 adhesive and 7 mixed failures. In the case of mixed failure, the area ratio of substrate and adhesive failure was observed as 5.43:4.57.

2) Substrate: Shotcrete, Corrosion inhibitor: Unapplied

Average failure stress: 423 psi. (Standard deviation = 130 psi)
Failure mode: 8 mixed failures. In the case of mixed failure, the ratio of substrate and adhesive failure was observed as 7.13:2.88.

3) Substrate: Concrete, Corrosion inhibitor: Applied

Average failure stress: 392 psi. (Standard deviation = 128 psi)

Failure mode: 1 substrate and 7 mixed failures. In the case of mixed failure, the ratio of substrate and adhesive failure was observed as 6.86:3.14

4) Substrate: Concrete, Corrosion inhibitor: Unapplied

Average failure stress: 454 psi. (Standard deviation = 119 psi)
Failure mode: 2 substrate and 5 mixed failures. In the case of mixed failure, the ratio of substrate and adhesive failure was observed as 8.2:1.8.

Pull-off strength of all samples exposed to the condition of "Freeze-thaw" was in excess of 200 psi acceptance value and confirmed the behavior assessment.

2.7.3 3% NaCl

1) Substrate: Shotcrete, Corrosion inhibitor: Applied

Average failure stress: 395 psi. (Standard deviation = 133 psi)
Failure mode: 8 mixed failures. In the case of mixed failure, the ratio of substrate and adhesive failure was observed as 2.00:8.00.

2) Substrate: Shotcrete, Corrosion inhibitor: Unapplied

Average failure stress: 444 psi. (Standard deviation = 168 psi)
Failure mode: 1 adhesive and 8 mixed failures. In the case of mixed failure, the ratio of substrate and adhesive failure was observed as 6.38:3.63.

3) Substrate: Concrete, Corrosion inhibitor: Applied

Average failure stress: 329 psi. (Standard deviation = 100 psi)

Failure mode: 2 adhesive and 7 mixed failures. In the case of mixed failure, the ratio of substrate and adhesive failure was observed as 2.86:7.14.

4) Substrate: Concrete, Corrosion inhibitor: Unapplied

Average failure stress: 328 psi. (Standard deviation = 70 psi)
Failure mode: 1 substrate, 2 adhesive and 7 mixed failures. In the case of mixed failure, the ratio of substrate and adhesive failure was observed as 4.50:5.50.

Pull-off strength of all samples exposed to the condition of "3% NaCl" was in excess of 200 psi acceptance value.

2.7.4 Wet in water

1) Substrate: Shotcrete, Corrosion inhibitor: Applied

Average failure stress: 323 psi. (Standard deviation = 36 psi)
Failure mode: 3 adhesive and 5 mixed failures, two mixed failure. In the case of mixed failure, the ratio of substrate and adhesive failure was observed as 2.2:7.8.

2) Substrate: Shotcrete, Corrosion inhibitor: Unapplied

Average failure stress: 322 psi. (Standard deviation = 42 psi)
Failure mode: 2 adhesive and 6 mixed failures. In the case of mixed failure, the ratios of substrate and adhesive failure were observed as 4.33:5.67.

3) Substrate: Concrete, Corrosion inhibitor: Applied

Average failure stress: 429 psi. (Standard deviation = 128 psi)

Failure mode: 3 adhesive and 6 mixed failures. In the case of mixed failure, the ratio of substrate and adhesive failure was observed as 5.33:4.67.

4) Substrate: Concrete, Corrosion inhibitor: Unapplied

Average failure stress: 392 psi. (Standard deviation = 79 psi)
Failure mode: 1 substrate, 2 adhesive and 6 mixed failures. In the case of mixed failure, the ratio of substrate and adhesive failure was observed as 5.17:4.83.

Pull-off strength of all samples exposed to the condition of "wet in water" was in excess of 200 psi acceptance value.

2.7.5 Wet/dry in water

1) Substrate: Shotcrete, Corrosion inhibitor: Applied

Average failure stress: 227 psi. (Standard deviation = 91 psi)
Failure mode: 1 substrate and 8 mixed failures. In the case of mixed failure, the ratio of substrate and adhesive failure was observed as 7.00:3.00.

2) Substrate: Shotcrete, Corrosion inhibitor: unapplied

Average failure stress: 360 psi. (Standard deviation = 58 psi)
Failure mode: 1 substrate, 4 adhesive and 4 mixed failures. In the case of mixed failures, the ratio of substrate and adhesive failure was observed as 7.75:2.25.

3) Substrate: Concrete, Corrosion inhibitor: Applied

Average failure stress: 457 psi. (Standard deviation = 89 psi)

Failure mode: 2 substrate and 7 mixed failures. In the case of mixed failure, the ratio of substrate and adhesive failure was observed as 5.71:4.29.

4) Substrate: Concrete, Corrosion inhibitor: Unapplied

Average failure stress: 442 psi. (Standard deviation = 91 psi)
Failure mode: 1 substrate and 7 mixed failures. In the case of mixed failures, the ratio of substrate and adhesive failure was observed as 6.43:3.57.

Pull-off strength of all samples exposed to the condition of "wet/dry in water" was in excess of 200 psi acceptance value.

2.7.6 0.2M NaOH

1) Substrate: Shotcrete, Corrosion inhibitor: Applied

Average failure stress: 419 psi. (Standard deviation = 193 psi)
Failure mode: 1 substrate, 2 adhesive and 6 mixed failures. In the case of mixed failure, the ratio of substrate and adhesive failure was observed as 1.67:8.33.

2) Substrate: Shotcrete, Corrosion inhibitor: Unapplied

Average failure stress: 348 psi. (Standard deviation = 84 psi)
Failure mode: 1 cohesive, 3 adhesives and 5 mixed failures. In the case of mixed failure, the ratio of substrate and adhesive failure was observed as 3.6:6.4.

3) Substrate: Concrete, Corrosion inhibitor: Applied

Average failure stress: 424 psi. (Standard deviation = 144 psi)

Failure mode: 2 substrates, 3 adhesives and 4 mixed failures. In the case of mixed failure, the ratio of substrate and adhesive failure was observed as 5.75:4.25.

4) Substrate: Concrete, Corrosion inhibitor: Unapplied

Average failure stress: 353 psi. (Standard deviation = 107 psi)
Failure mode: 1 substrate, 4 adhesives and 4 mixed failures. In the case of mixed failure, the ratio of substrate and adhesive failure was observed as 5.5:4.5.

Pull-off strength of all samples exposed to the condition of "3% NaCl" was in excess of 200 psi acceptance value.

2.7.7 Summary of test results

Concrete without Sika FerroGard 903

The variations of the bond strength are calculated based on the specimens exposed to the room temperature without any conditioning. The effect of each conditioning parameter on the bond strength is shown in Figure 2-24 and Table 2-7. One can see that although all bond strengths of the specimens satisfy the 200 psi acceptance criterion, the conditioning parameters severely reduce the average pull-off bond strength. The worst case is the 44% reduction under the condition of 3% NaCl.

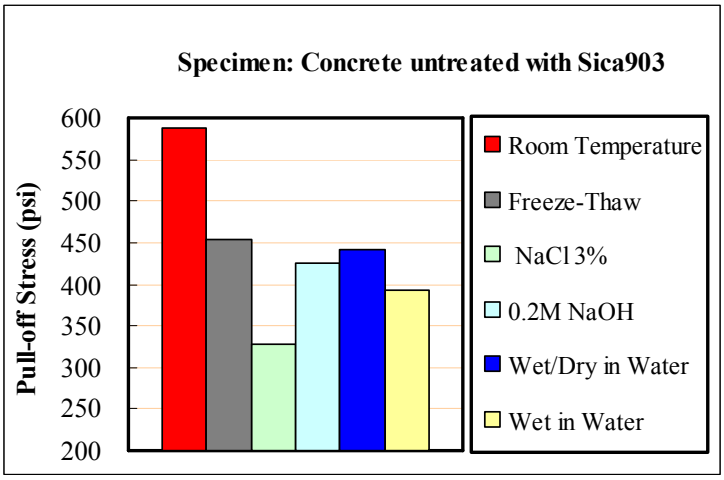

Figure 2-24 Average pull-off stress of concrete untreated with corrosion inhibitor

Influencing Parameters	Reduction (%)
Freeze-thaw	23
3% NaCl	44
0.2 M NaOH	28
Wetting/Drying in water	25
Wet in water	33

Table 2-7 Comparison of deduction of average pull-off strength

Concrete with Sika FerroGard 903

The average pull-off test results is shown in **Figure 2-25** and Table 2-8. The 33% and 28% reduction were measured in the conditions of 3% NaCl and 0.2 M NaOH compared with the specimens in the room temperature without any conditioning.

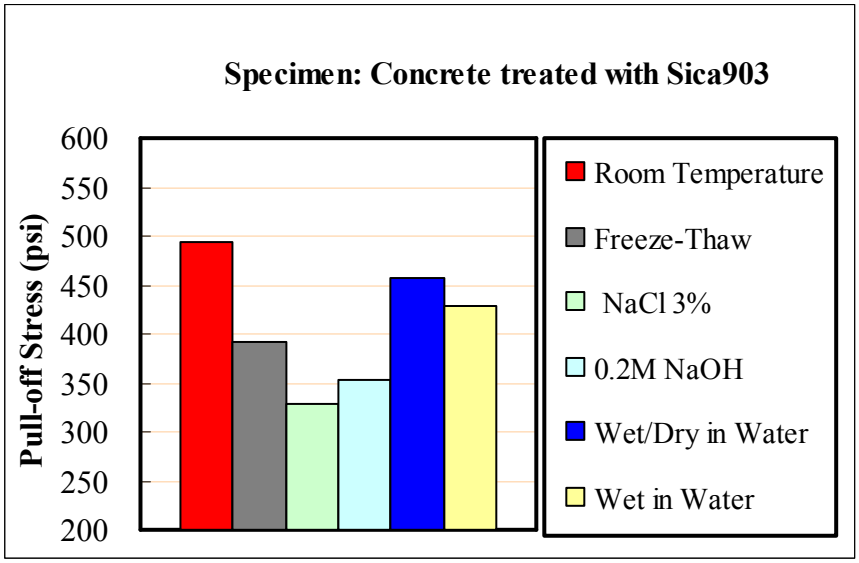

Figure 2-25 Average pull-off stress of concrete untreated with corrosion inhibitor

Influencing Parameters	Reduction (%)
Freeze-thaw	21
3% NaCl	33
0.2 M NaOH	28
Wetting/Drying in water	7
Wet in water	13

Table 2-8 Comparison of reduction of average pull-off strength

Shotcrete with Sika FerroGard 903

The average pull-off stress is shown in Figure 2-26 and Table 2-9. The worst degradation was observed under the condition of wetting/drying in water. A very small reduction (9 %) was measured in the condition of 0.2M NaOH.

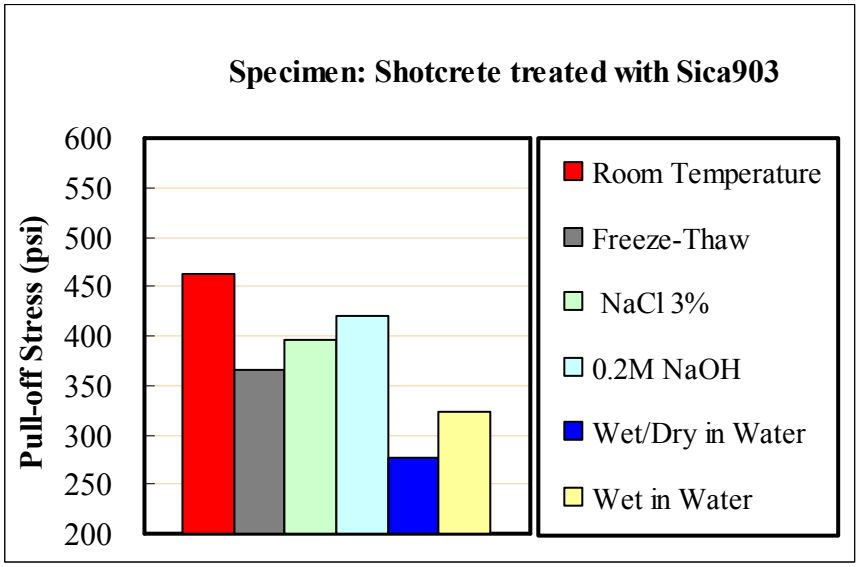

Figure 2-26 Average pull-off stress of concrete untreated with corrosion inhibitor

Influencing Parameters	Reduction (%)
Freeze-thaw	24
3% NaCl	15
0.2 M NaOH	9
Wetting/Drying in water	40
Wet in water	30

Table 2-9 Comparison of reduction of average pull-off strength

Shotcrete without Sika FerroGard 903

The average pull-off stress from test results is shown in Figure 2-27 and Table 2-10. A 27% reduction was assessed under the condition of wet in water. No reduction was observed under the condition of 3 % NaCl exposure.

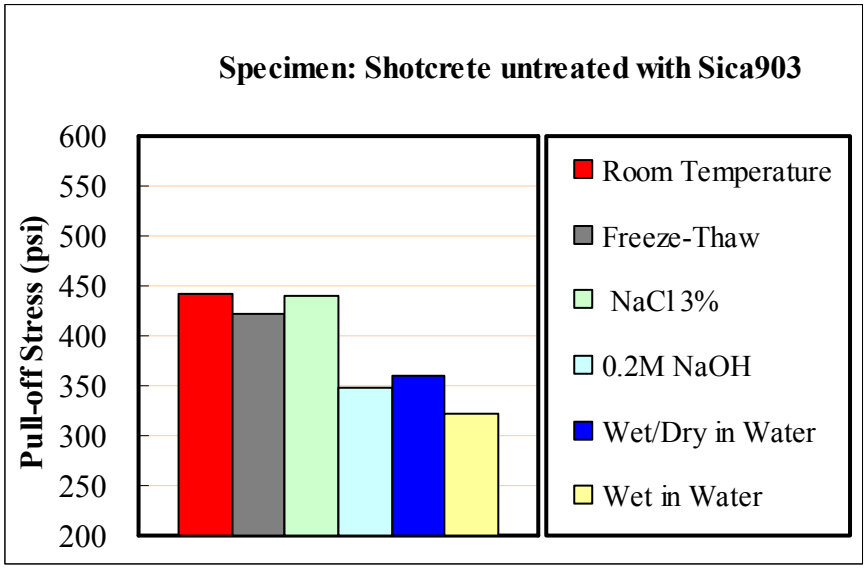

Figure 2-27 Average pull-off stress of concrete untreated with corrosion inhibitor

Influencing Parameters	Reduction (%)
Freeze-thaw	4
3% NaCl	0
0.2 M NaOH	21
Wetting/Drying in water	19
Wet in water	27

Table 2-10 Comparison of reduction of average pull-off strength

2.7.7.1 Effect of substrate on the bond strength

Table 2-11 summarizes the effects of the substrates (concrete or shotcrete) on the pull-off bond strength. In Table 2-11, Table 2-11the two columns of "difference" were calculated by subtracting the pull-off stress of shotcrete substrate from the pull-off stress of concrete. As one can see, the concrete substrate has higher pull-off stress except for the 3% NaCl

conditioning. Therefore, the concrete used in the present study can be considered as a better substrate than the shotcrete used in Castlewood Canyon Bridge.

For the specimens untreated with Sika FerroGard 903, the difference in the condition of room temperature is about 25%. In the case of specimens treated with SicaFerroGard 903, the difference in the condition of wet/dry in water is as high as 50%. When the specimens were exposed to 3% NaCl, shotcrete performed better than concrete as a substrate: 35% higher pull-off stress for untreated specimens, and 20% higher for the treated specimens.

Unit: psi	Untreated with Sika FerroGard 903			Treated with Sika FerroGard 903		
Influencing Factors	Concrete	Shotcrete	Difference	Concrete	Shotcrete	Difference
Room temperature	588	443	+145	494	363	+31
Freeze-thaw	454	423	+31	392	365	+27
3% NaCl	328	444	-116	329	395	-66
Wet in Water	392	322	+70	429	323	+106
Wet/Dry in water	442	360	+82	457	227	+230
0.2M NaOH	353	348	+5	424	419	+5

Table 2-11 Comparison of pull-off strength for different substrates

Unit: psi	Concrete			Shotcrete		
	Sika FerroGard 903			Sika FerroGard 903		
Influencing Factors	Untreated	Treated	Difference	Untreated	Treated	Difference
Room temperature	588	494	+94	443	463	-20
Freeze-thaw	454	392	+62	423	365	+58
3% NaCl	328	329	-1	444	395	+49
Wet in Water	392	429	-37	322	323	-1
Wet/Dry in water	442	457	-15	360	227	+133
0.2M NaOH	353	424	-71	348	419	-71

Table 2-12 The effect of Sika FerroGard 903 on the pull-off strength

2.7.7.2 Effect of the corrosion inhibitor on bond strength

The effect of the corrosion inhibitor on the pull-off strength is shown in Table 2-12. For the concrete substrate, the difference of the pull-off strength between untreated and treated samples ranges from -71 psi (-17%) ~ + 94 psi (+19%). For the shotcrete substrate, the difference ranges from -71 psi (-17%) ~ +133 psi (+59%). Based on the observation of test results, there is no consistent influence of the corrosion inhibitor on the bond strength. Therefore, it may be concluded that the corrosion inhibitor, Sica FerroGard 903, does not affect the pull-off strength.

2.8 Fire Endurance Test

Due to the World Trade Center tragedy, fire resistance of construction materials becomes a major concern. The resin in FRP is a flammable element and it has potential risk under fire. Understanding the characteristics of fire resistance of CFRP sheets is a very important issue. In order to investigate the burning characteristics of CFRP sheets and resin, the fire endurance test was performed.

Thermogravimetry (TG) analysis is a relatively rapid test. Dubberke and Marks (1994) states that TG analysis is a good indicator for evaluating the fire durability of concrete. TG determines the mass change of a sample as a function of temperature or time. It is an ideal tool, especially for quality control and assurance, as well as for failure analysis of complex polymer mixtures and blends. In this project, a TG technique was used to analyze the CFRP sheet and resin through heating the specimen to the temperature above 600 ^{o}C and recording the weight loss and the change of weight loss as a function of temperature.

2.8.1 Experimental Work

Materials

The experimental work was designed to analyze the fire endurance of SCH 41 and composite and Typo S epoxy using TG analysis. To perform TG experiments, a representative portion of the FRPs was obtained from the specimen, and then the specimen was chopped to a less than 0.2 in^2 area, as it is found at the start of the experimental work that the finer the particle, the smoother the TG analysis (Dubberke and Marks 1994). Total area is 0.5177 in^2 and the weight is 606.6mg.

Testing procedure

During heating, gas liberation usually takes place. This can lead to a gas back-diffusion and possible condensation on the meter movement (Brown 1994). To avoid this, carbon dioxide was used as a purge gas and was admitted onto balance housing at an adequate rate to fill the control chamber. A balance of 0.1mg accuracy was used to weigh 606.6 mg specimen in the platinum tray. In this experiment, the specimen was heated at a rate of 4^{o}C/min up to a temperature of 700^{o}C. Thus, the total duration of the heating was 180 min. Figure 2-28 shows a TG analyzer which was used in this project.

Figure 2-28 The fire endurance apparatus

2.8.2 Results

The principal data obtained from TG curves were: (1) decomposition curves; (2) rate weight loss; (3) slope of curve. As represented in Figure 2-29, the results show that the CFRP sheet and epoxy yields a TG curve with three-stage weight loss. The first stage is one in which the specimen does undergo a sudden, sharp drop in weight starting around 200 ^{o}C. In the second stage, a gradual increase in slope is witnessed. During the third stage the carbon fabric decomposition occurs around 450 ^{o}C. At 600 ^{o}C, a full decomposition of the composite takes place.

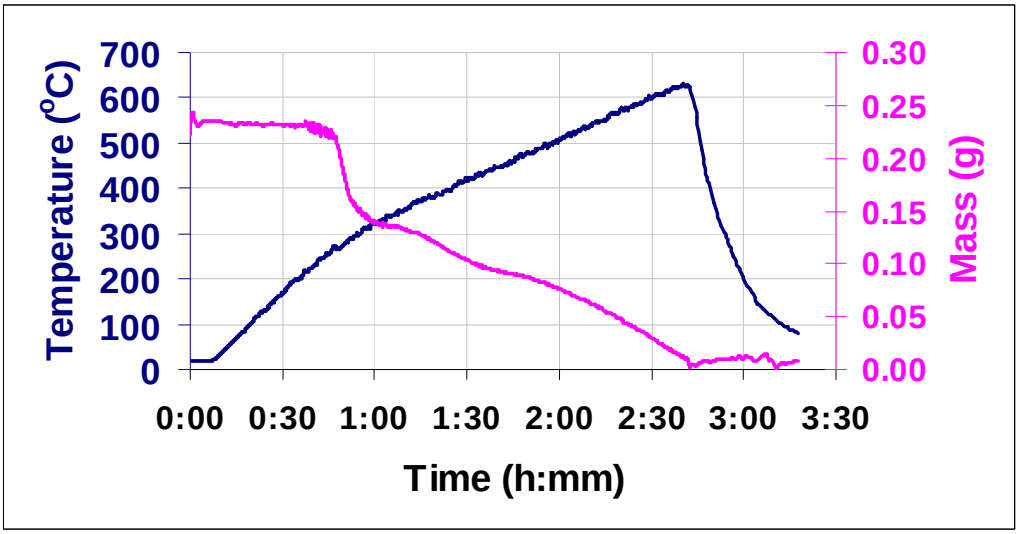

Figure 2-29 TGA Thermograms for Tyfo SCH 41 with S Epoxy

Figure 2-30 shows the relation between weight loss and temperature. The slope prior to the transition in TG curves indicated the fire durability of the composite. The maximum useable temperature was 230 ^{o}C based on the epoxy loss at that temperature.

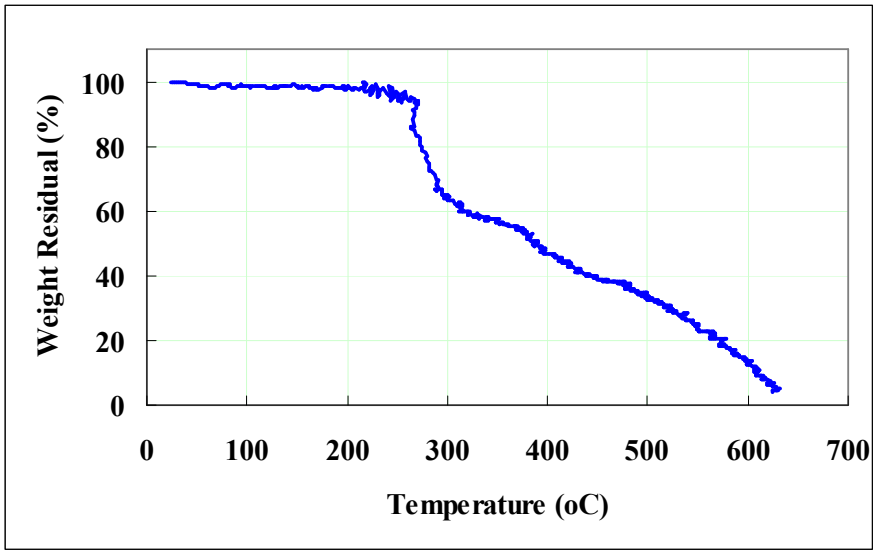

Figure 2-30 TG curve for Tyfo SCH 41 with S Epoxy

CHAPTER 3 WIRELESS REAL-TIME REMOTE MONITORING OF THE ARCH BRIDGE

3.1 Introduction

The Castlewood Canyon Bridge is 404'-5" long and 43' wide. Figure 2-1 shows the view of the bridge before repairs were done. Funded by the Innovative Bridge Research and Construction (IBRC) Program of FHWA, the rehabilitation project was conducted in 2003. This rehabilitation project was unique in that the superstructure of the arch bridge was completely replaced while leaving the arch ribs. The arch rib of the bridge was strengthened by carbon fiber reinforced polymer surface reinforcing with the wet lay-up technique. The repaired bridge is shown in Figure 3-1.

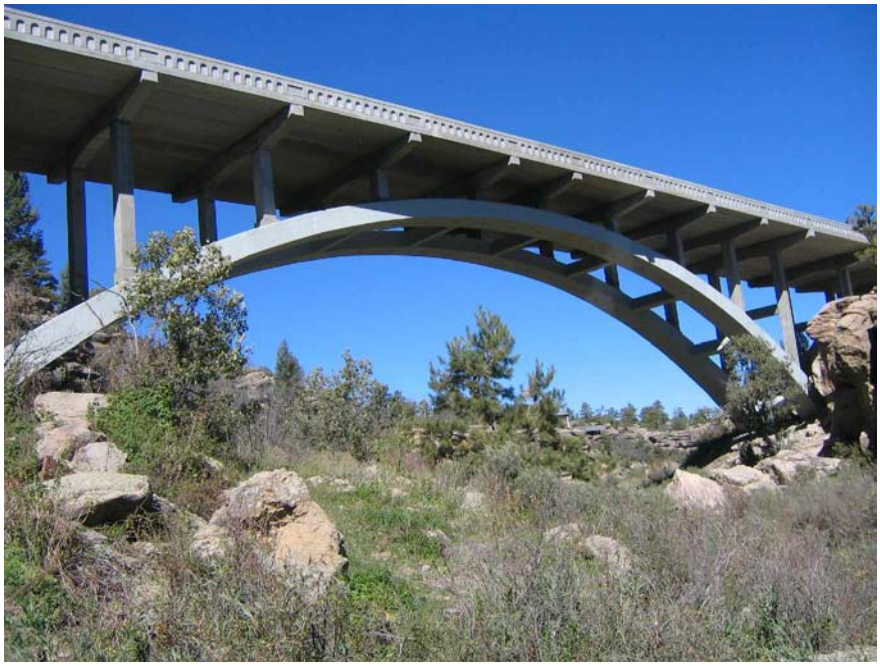

Figure 3-1 The repaired Castlewood Canyon Bridge

In order to monitor the performance of the repaired bridge, a wireless remote structural monitoring system was installed on the bridge. The conventional methods for bridge health

monitoring are usually time consuming and expensive. This state-of-the-art monitoring system utilizes wireless data transfer technology, and it is primarily designed to access a remote data acquisition system and download the data from control office. Our experiences show that the system is very cost effective because site visits to collect data can be greatly reduced.

3.2 In-Situ Health Monitoring System

3.2.1 Datalogging system

The datalogger (CR10X) was installed to record and store data from corrosion-monitoring instruments (ECI-1) and strains from each gage location with 128K of memory. 20 sensors were multiplexed by a two AM 16/32 Multiplexer. A solar panel (MSX20R) was install on the site to converted sunlight to electricity in order to recharge the battery of the system. The SC932A was used to interface a datalogger to a CDMA modem that was configured with an RS-232 DCE (Data Communication Equipment) serial port. Communication between this remote unit and the host computer was maintained via the wireless modem, which could be utilized for downloading the stored data, as well as, programming the remote micro-processor for various data acquisition takes. Using a Yagi cellular antenna, the CDMA, a full-duplex digital cellular modem, communicated with the base station computer via a CDMA network and the PSTN (Public Switched Telephone Network). The speed of data transfer was dependent on the lower of the two speeds, the baud rate of modem and the baud rate of the serial port. The Loggernet software was used to set up, configure, and retrieve data from a datalogger over wireless communication. The controller equipment is shown in Figure 3-3.

Data acquisition and processing functions should be controlled as per instructions. In this project, the programming was divided into two tables; the first table calculates strains and the second table measures corrosion related parameters. Self-monitoring functions such as

alarm warnings to a central computer and the loss of a solar panel is described in the datalogging program. A third table is used for programming subroutines which are called by instructions in *Table 1* and *Table 2*. The schematic procedure of the program is shown in Figure 3-2. The datalogging program coding is described in the Appendix G.

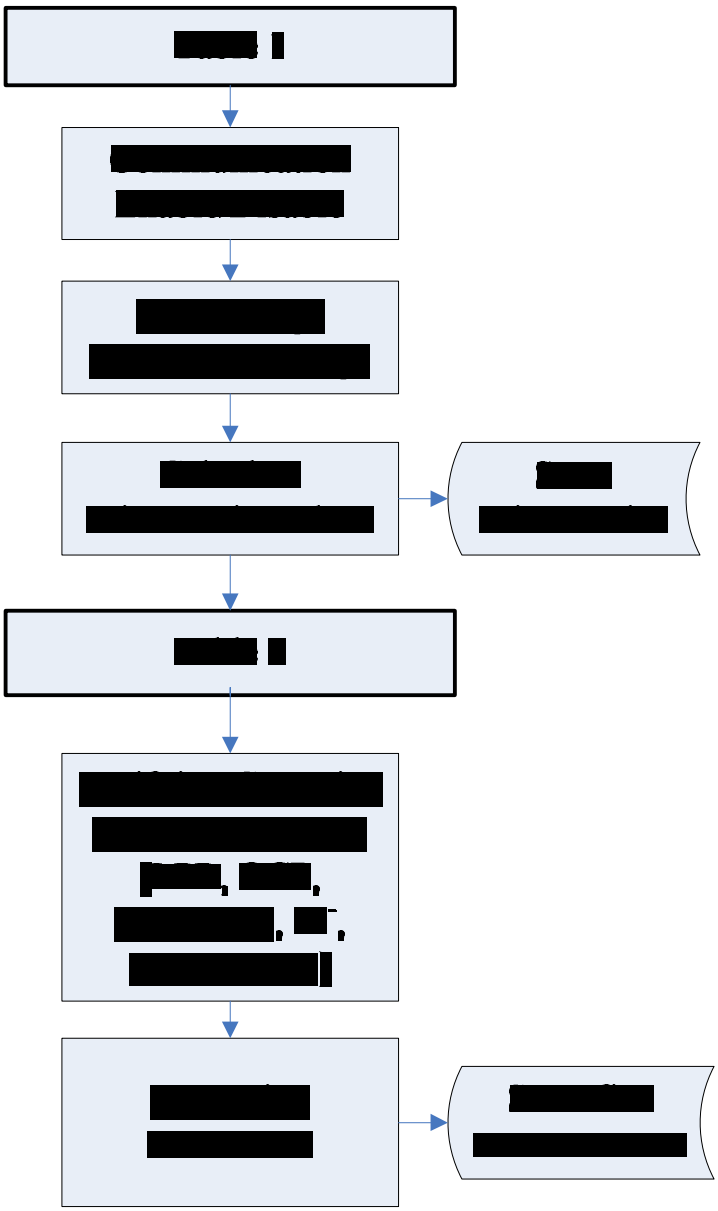

Figure 3-2 Schematic Datalogging Programming Procedures

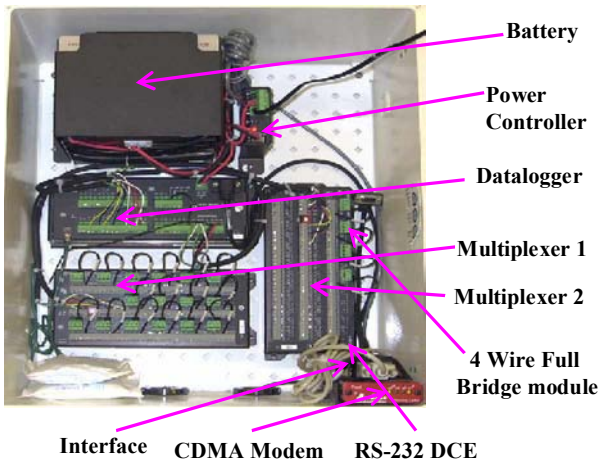

Figure 3-3 Equipment for long-term structural monitoring system

The wireless remote datalogging system was installed in the site near the bridge shown in Figure 3-4.

Figure 3-4 In-situ health monitoring system in Castlewood Canyon Bridge

3.2.2 Sensors

3.2.2.1 Strain gages

The type of strain gage used in this project was EA-06-250AE-350 manufactured by Vishay Micro-Measurements. The gage factor was 2.100±0.5%. Eighteen strain gages were installed at the top, bottom and side surface of the arch in the spring of 2004. The locations of strain gages are shown in Figure 3-5, Figure 3-6 and Figure 3-8. The sensors were tested after installation and baseline strains were recorded.

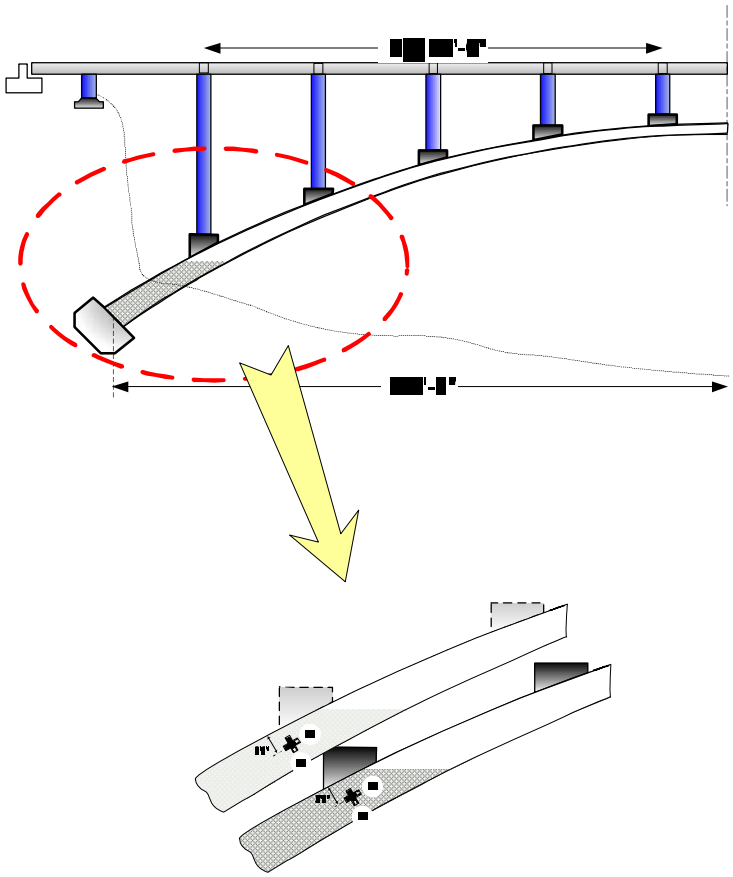

Figure 3-5 Strain gage locations (Side view)

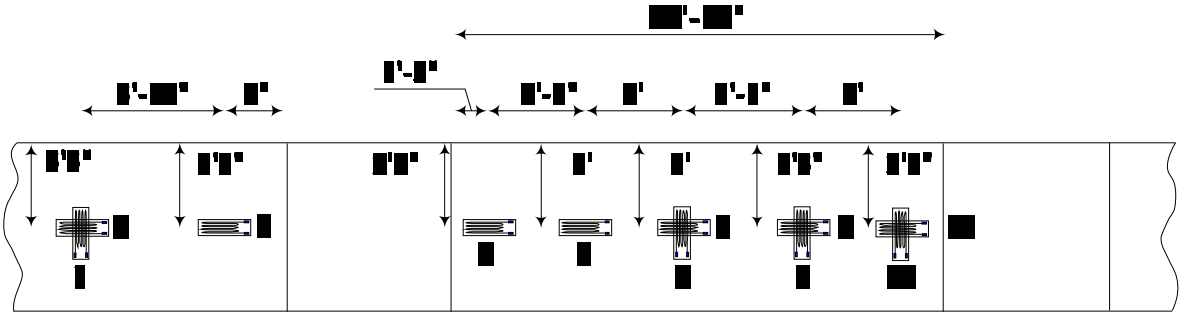

Figure 3-6 Strain gage locations - Extrados (Back)

Figure 3-7 Wiring of strain gages - Extrados (Back)

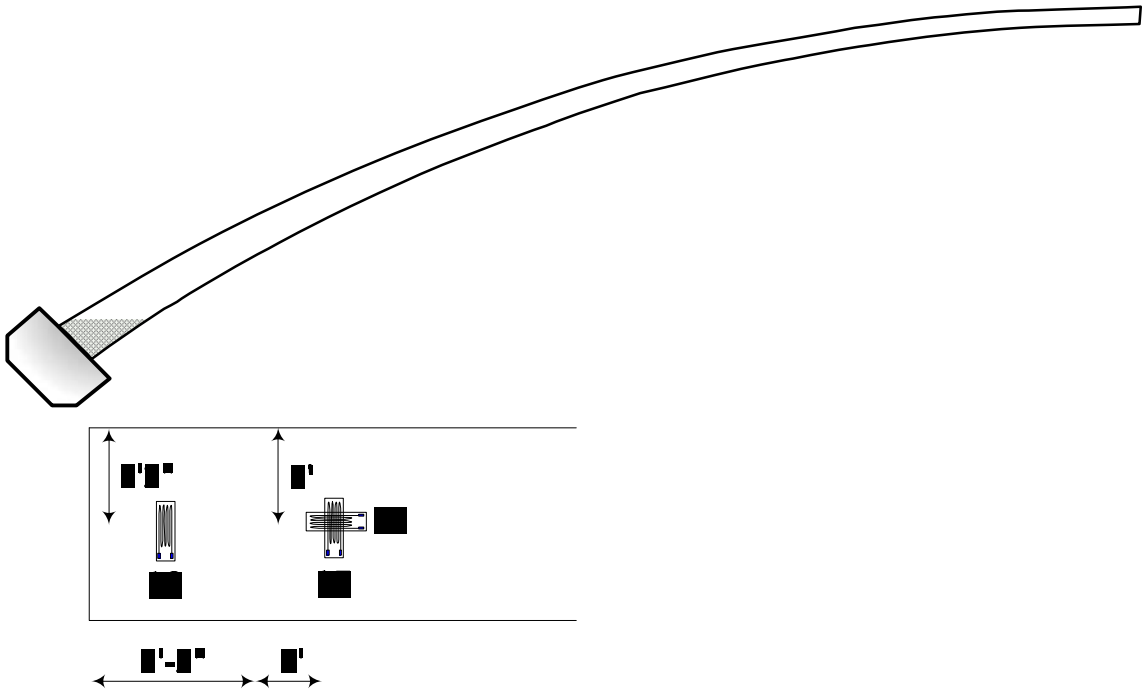

Figure 3-8 Strain gage locations - Intrados (Soffit)

3.2.2.2 Corrosion sensors

The corrosion sensor, ECI-1 was used in the project. It is an embeddable non-destructive evaluation corrosion monitoring instrument. It is capable of measuring parameters important for long term corrosion monitoring, including linear polarization resistance (LPR), open circuit potential (OCP), resistivity, chloride ion concentration and temperature in the concrete. In this project, the ECI-1 sensor is used as a digital peripheral device connected to an embedded local area network. The instrument communicates with an external datalogger using SDI-12 industry standard protocol. The instrument stored in the datalogger can be downloaded to a computer. The ECI-1 monitors five parameters related to the corrosion of reinforcement rebar in concrete structures (Virginia Technologies 2003)

1) Linear Polarization Resistance (LPR)

LPR, measured in KΩ-cm^2, is basically a resistance measurement of the interface between the sacrificial working electrode and the surrounding concrete. It is the measurement that is most closely related to the "Corrosion Rate" of the reinforcement steel, which is typically measured in mm/yr. Polarization resistance in concrete is measured using the three electrode arrangement; steel working electrode (WE, rebar), a stainless steel counter electrode (CE, inert stainless steel), and a MnO_2 reference electrode (RE, half-cell). The WE is a sacrificial electrode made of black steel and is meant to corrode at the same rate as the ASTM 615/A compliant steel.

2) Open circuit potential (OCP)

OCP, measured in volts, is the electrochemical potential between the sacrificial black steel working electrode and the MnO_2 reference electrode. As the corrosion rate increases, OCP typically becomes more negative. Similar to the LPR measurement, the ECI-1 accomplishes OCP measurements using a sacrificial black steel working electrode and a MnO_2 reference electrode.

3) Chloride Level

Chloride level is measured in volts. The chloride ion concentration is measured by recording the potential of a calibrated Ag/AgCl electrode versus a MnO_2 reference electrode. ECI-1 accomplishes chloride level measurements by measuring the potential between an ion specific Silver/Silver Chloride (Ag/AgCl) wire electrode and the instrument's MnO_2 reference electrode. As the concrete chloride concentration increases, this voltage becomes more negative.

4) Resistivity

Resistivity of the concrete is measured with a four pin Au probe. Resistivity, measured in KΩ-cm or 1/ conductivity is used as an indicator of the moisture content of the concrete. For corrosion to take place, the concrete must contain sufficient amount of moisture and chloride. The ECI-1 uses four stainless steel wire electrodes to accomplish resistivity measurements.

5) Temperature:

Temperature is measured in degrees Celsius. The ECI-1 measures temperature using an internal semiconductor temperature sensor.

Figure 3-9 shows the installation of the ECI-1 corrosion sensors. The corrosion sensors were tied on rebars as necessary to keep them in place, shown in Figure 3-10.

Figure 3-9 Installation of corrosion sensors during construction

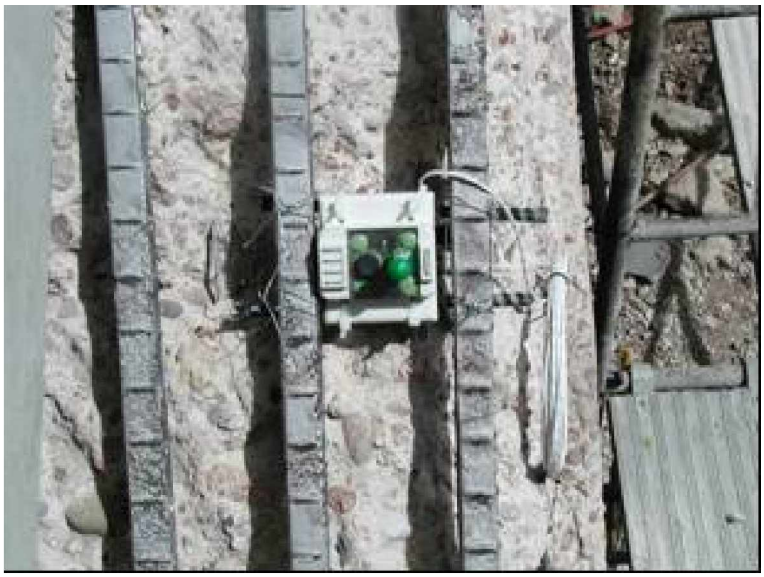

Figure 3-10 An installed corrosion sensor (ECI-1)

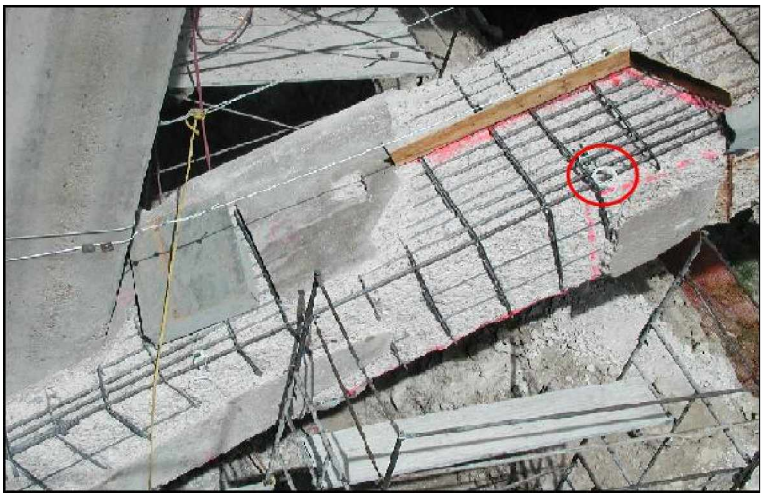

Figure 3-11 Locations of ECI-1 corrosion sensors installed in Castlewood Canyon Bridge

During the concrete pouring, as shown in Figure 3-12, the sensors were protected from mechanical damage. Direct contact between tools such as vibrators and the sensors were avoided. The mix design of the shotcrete is shown in Table 2-1. Figure 3-13 shows the embedded corrosion sensors after shotcreting. This work was performed on May 23, 2003.

Figure 3-12 Shotcreting over corrosion instrument

Figure 3-13 The embedded corrosion instrument (ECI-1)

3.3 Monitoring Results

3.3.1. Monitoring of strains

The strain gages were installed on May 6, 2004. The baseline strains were recorded on May 7, 2004. Data were collected with an execution interval of 10 seconds and stored every 5 minutes for 24 hours from May 7, 2004 to October 7, 2004. All collected monthly data are provided in Appendix E.

Comparing the profiles of temperature changes and strain variations shown in Figure 3-14 through 2-17, one can see that the temperatures and the strains at most of the locations were cyclic, and more importantly, they vary at the same frequency and same phase angle. This simply means that the strain variations are due to the temperature variation. Therefore, the temperature variation is more important than the mechanical loading applied on the structure (i.e. the traffic loading). This phenomenon was also observed during the monitoring of the FRP bridge deck in O'Fallon park bridge (Xi, Y. et al., 2004).

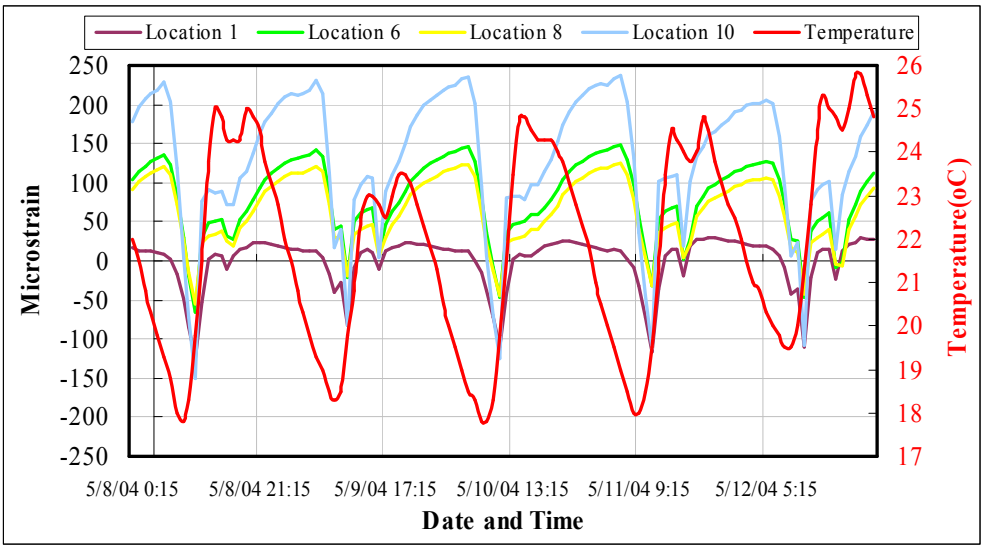

Figure 3-14 The transverse microstrain distributions at the Extrados of the arch and the corresponding temperature variation (Location 1, 6, 8 and 10)

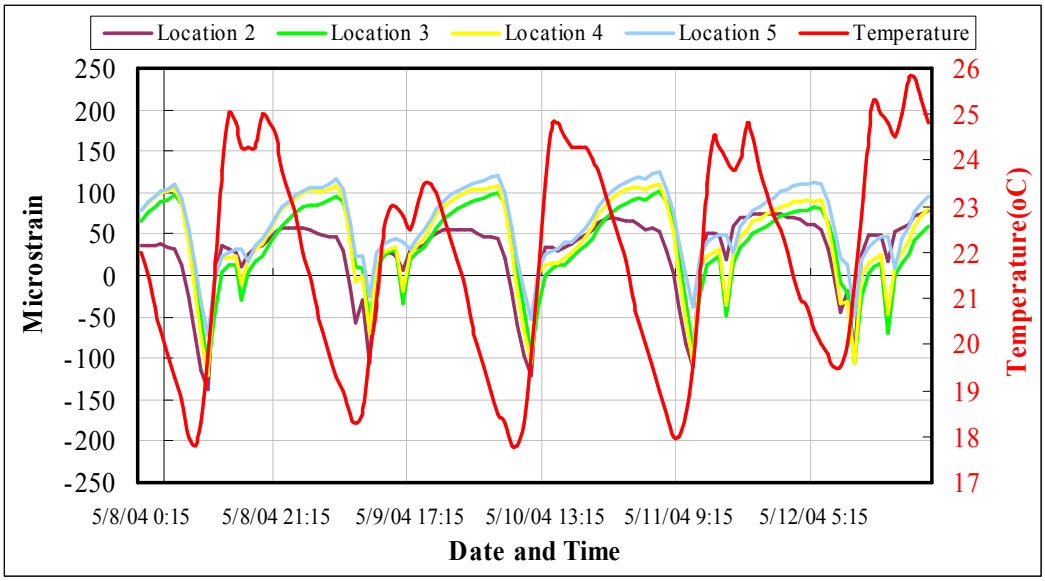

Figure 3-15 The longitudinal microstrain distributions at the Extrados of the arch and the corresponding temperature variation (Location 2, 3, 4 and 5)

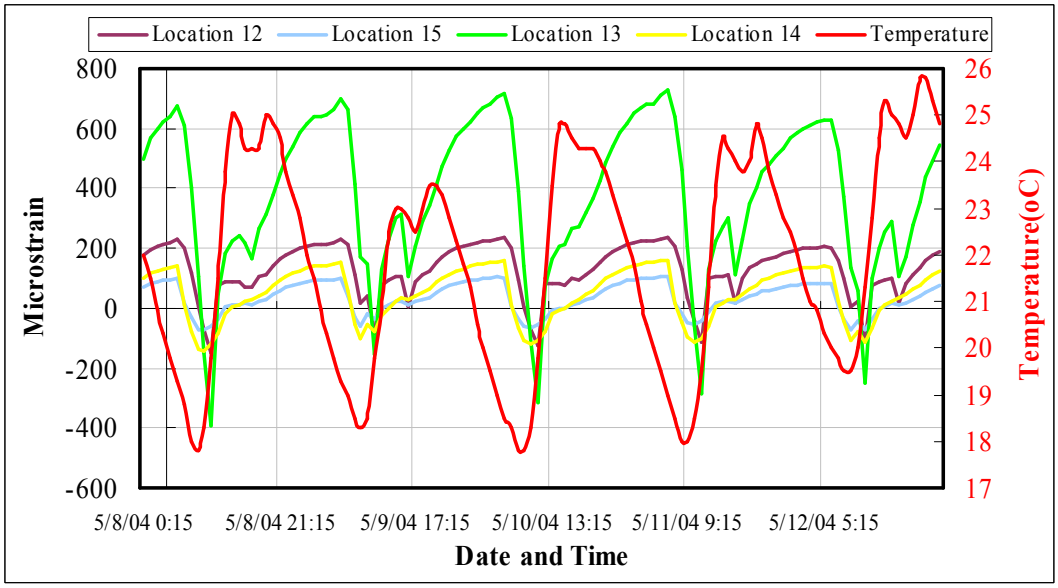

Figure 3-16 The longitudinal (Location 12 &15) and transverse (Location 13 & 14) microstrain distributions at the Intrados of the arch and the corresponding temperature variation

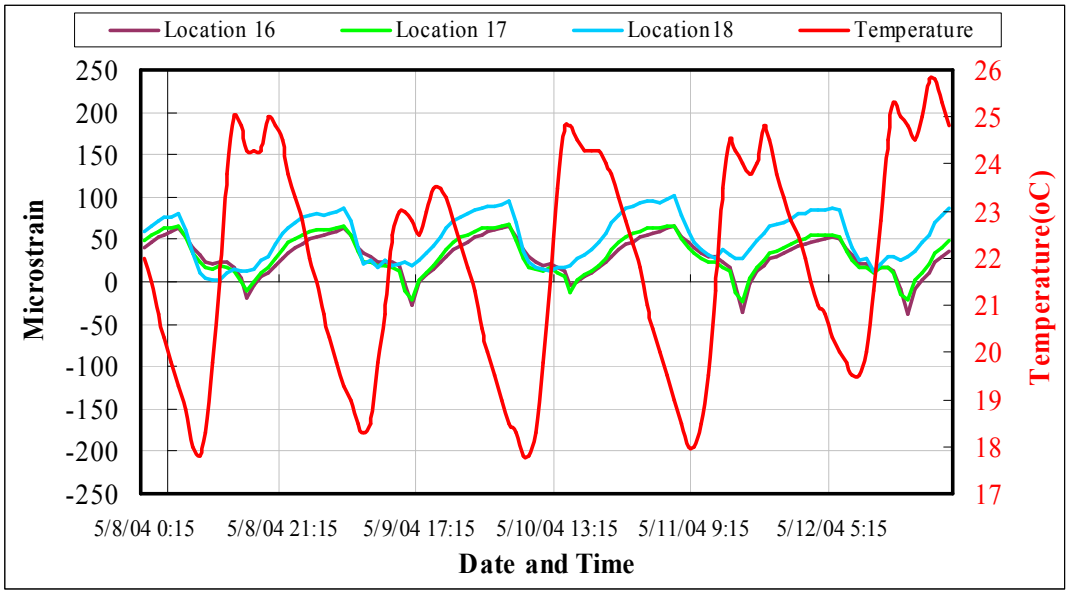

Figure 3-17 The longitudinal (Location 16) and transverse (Location 17 & 18) microstrain distributions at the Intrados of the arch and the corresponding temperature variation

The temperature was measured at 3 in. deep from the surface of the Extrados of the arch rib. From above figures, one can see that the strains were usually within the range of ±200 με, except the strain at location 13 which is about 600 με. The maximum strain recorded was up to 1400 με (0.14 %) at the Location 5 in August, as shown in Figure 3-18.

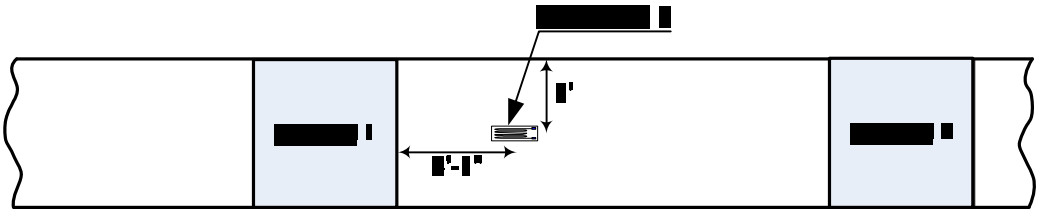

Figure 3-18 The top view of the Extrados of the arch

The minimum ultimate rupture strain was 0.006 inch/inch (Colorado Project No. BR 0831-085, Subaccount No. 13398). Using the ultimate strain of 0.6 %, the maximum strain of 0.14 % was about 23 % of the minimum ultimate rupture strain. At this moment, we do not know why such a high strain was recorded at the Location 5. More readings need to be taken in the future to evaluate the long-term performance of the arch of this bridge.

3.3.2 Monitoring of corrosion related parameters

Using ECI-1 corrosion sensors, the data of five parameters were collected with an execution interval of 30 minutes and stored values every hour.

Temperature (^{o}C)

Figure 3-19 shows the history of temperature inside the concrete. The temperature was measured at 3 in. deep from the Extrados of the arch rib. The temperature profile basically represents daily temperature variation.

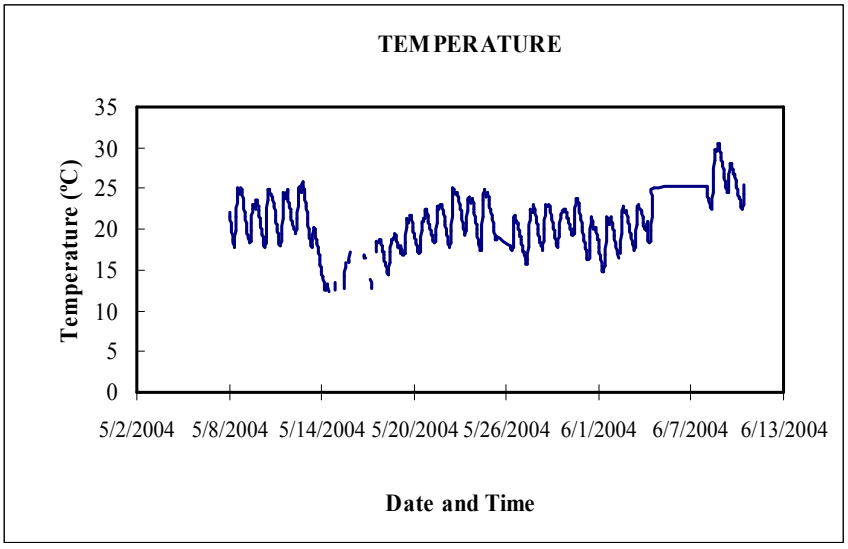

Figure 3-19 Temperature history (^{o}C)

Resistivity (Ω· cm)

The concrete resistivity was performed at the same collecting and store rate as the temperature measurements. Concrete resistivity measurement was taken in a range of 15,000 to 1,000 Ω-cm. The concrete resistivity can be used as a measure of corrosion rate, the permeability, and the moisture content of concrete. Since the rate of oxidation is directly related to the amount of heat energy available, the temperature affects the corrosion rate. On the other hand, the temperature has direct effect on the resistivity, because relative humidity decreases with increasing temperature and resistivity increases with increasing temperature. From the resistivity, the electrical conductivity of concrete can be determined (the conductivity = 1/resistance), which is related to ionic movement in the aqueous pore solution of the concrete. The general trend is that high permeable concrete may have a high conductivity (low electrical resistance).

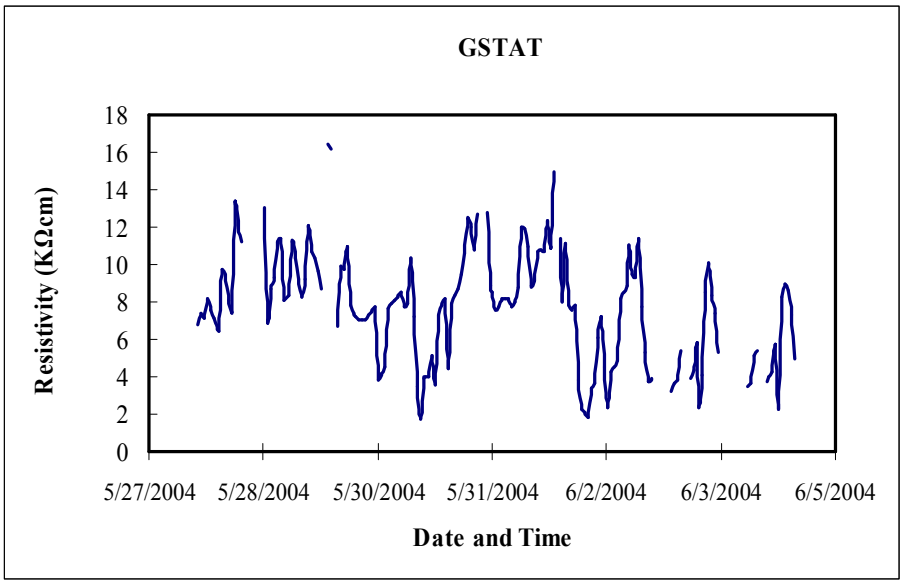

Figure 3-20 Measurement history of resistivity

Figure 3-20 shows the profile of concrete resistivity. At the current measurement from May 27, 200 to June 5, 2004 for 9 days, the data value represents 14917 Ω-cm (maximum) and

1762 Ω-cm (minimum), and 7605 (average). Based on Table 3-1, the average value of resistivity is not a good indicator to determine the current corrosion representation.

Resistivity (Ω· cm)	Corrosion risk
> 100,000 to 200,000	very low corrosion rate even with high chloride concentration or carbonation
50,000 – 100,000	Low corrosion rate
10,000 – 50,000 Ω· cm	Moderate to high corrosion rate where rebar is active
< 10,000	Resistivity is not the controlling parameter of the corrosion rate

Table 3-1 Interpretation of corrosion potential measurements (Non-destructive corrosion rate monitoring for reinforced concrete structures (Feliu, S., et al. 1996)

As explained earlier, resistivity can significantly vary by moisture content and temperature. The resistivity profile fluctuates significantly with temperature, as shown in Figure 3-21. Apparently, it does not provide reliable information to determine the rate of rebar corrosion.

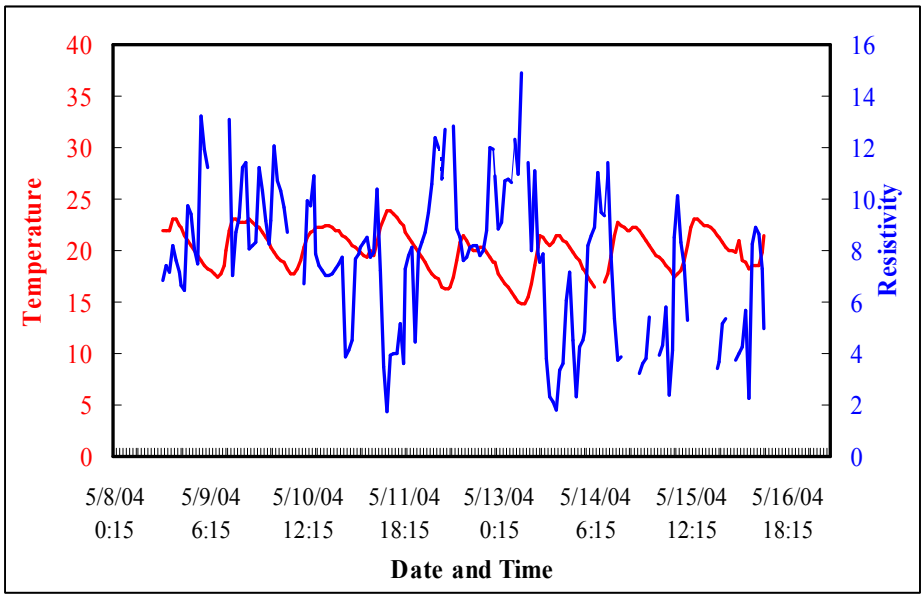

Figure 3-21 Comparison of both resistivity (Ω-cm) and temperature (^{o}C) profile Chloride Level (volts)

Corrosion of reinforcing steel bars embedded in cementitious materials is a complex phenomenon. Chloride ions in cementitious do not directly cause sever damage to the cementitious materials, it penetrates into the cementitious materials and towards the reinforcing rebars. Once the chloride concentration reaches a certain critical value, the passive protective film on the surface of rebar will be broken and the corrosion process starts. Therefore, monitoring the level of chloride concentration in concrete becomes an important research topic. The mechanism of chloride penetration and the rate of penetration can be significantly different depending on water-cement ration, curing time, types of cement, and aggregate content. In order to identify the level of the chloride in the embedded reinforcing bars and to determine the effectiveness of the corrosion inhibitor, the chloride level in the concrete was measured by the corrosion sensor. Figure 3-22 shows the chloride variation and the chloride levels increase positively with time (Note: the manufacturer is currently working on a conversion chart to correlate the voltage reading to total chloride concentration in percentage in concrete).

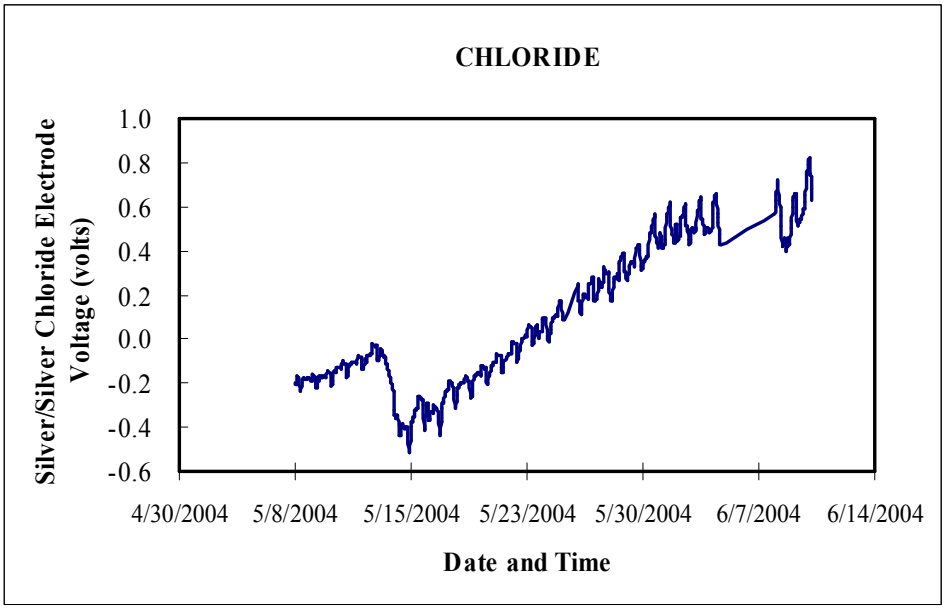

Figure 3-22 History of chloride concentration

The increase of the chloride content is not due to the penetration of chloride from outside of the concrete arch. The carbon FRP wrapping and the shotcrete are brand new, it will take some time for the chloride to penetrate into the concrete. The increase of the chloride concentration may be due to the redistribution of the internal chloride. Since the internal chloride concentration of existing concrete is higher than that of the new shotcrete, the chloride will diffuse from the existing concrete to the new shotcrete, which makes the chloride level increases. The same phenomenon occurs in new concrete patches applied on existing concrete with high chloride concentration.

Open Circuit Potential (= Corrosion Potential, volts)

The corrosion potential can give a fundamental indication of the corrosion risk. The open circuit potentials were monitored using a sacrificial black steel working electrode and a MnO_2 reference electrode. The potentials are more negative and ranged from 157 to -755 mV, as compared to the MnO2 reference electrode, shown in Figure 3-23. As the corrosion rate increases, corrosion potentials typically become more negative signaling that the corrosion of embedded reinforcing rebar may be active.

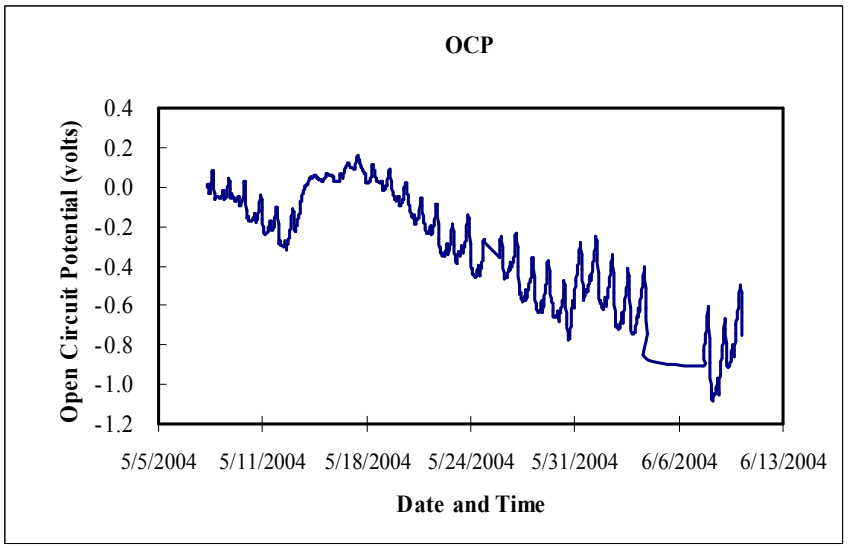

Figure 3-23 History of open circuit potential

In Figure 3-23, the potential is moving towards the negative side. This is consistent with the readings of chloride concentration. This is actually not a surprising result. One of the major concerns for concrete patching is that the corrosion can take place right at the interface between the new and existing concrete, because of the large concentration difference in chloride levels and the high moisture content in the new concrete.

Linear Polarization Resistance ($k\Omega.cm^2$)

The polarization resistance is an indication of the corrosion rate. The corrosion current is linearly related to polarization resistance. This gives a direct quantitative measurement of the amount of steel turning into oxide at the time of measurement. From Faraday's equation, the corrosion current can be extrapolated to direct metal sectional loss. In this project, the conductivity in unit $\mu S/cm^2$of is determined as the inverse of the linear polarization resistance. Therefore, the conductivity is directly proportional to the corrosion rate. If the conductivity is larger than 15 $\mu S/cm^2$, the reinforcing rebar is considered to have active corrosion (Aldykiewicz 1998). If the polarization conductance is larger than 20 $\mu\Omega/cm^2$, rusting of the rebar has occurred. If the polarization conductance is less than 15 $\mu\Omega/cm^2$, the reinforcing rebars embedded in concrete are non-corroded and rust-free (Berke 1987).

The conductivity curves measured from May 8, 2004 to May 21, 2004 are summarized in Figure 3-24 as the average, minimum and maximum values. For the aspect of average conductance values obtained from the sensor, the reinforcing rebars embedded in the concrete may be considered to have active corrosion. Again, this is consistent with the readings of chloride levels and open circuit potential. After about one year of the repair work, the corrosion of the rebars may be re-activated.

Now, we expect that the corrosion of the rebars would be slowed down if the corrosion inhibitor in the shotcrete can penetrate onto the surface of the rebars and form a protective layer on the surface of the rebars. In order to confirm the speculation, the monitoring process for the arch should be continued.

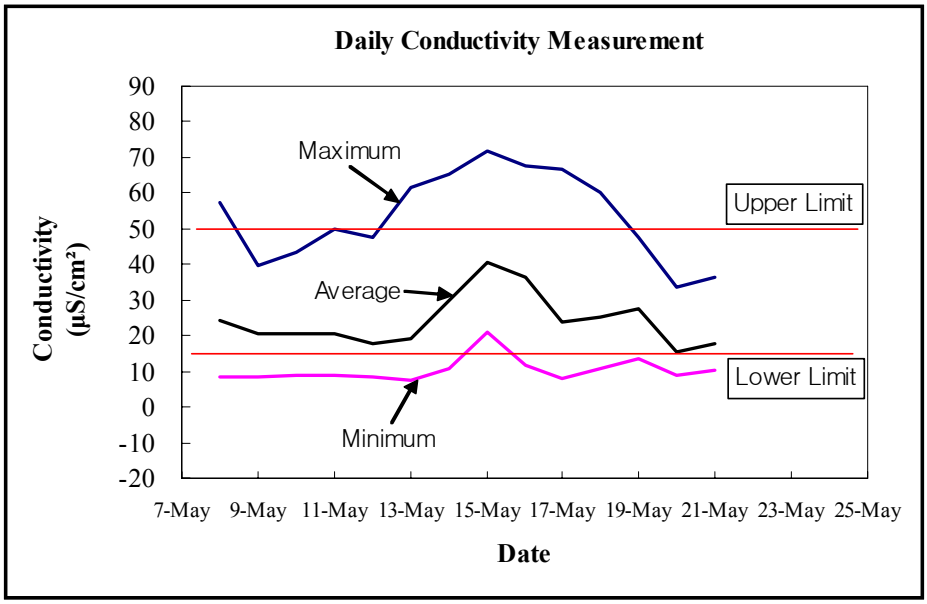

Figure 3-24 The profiles of the conductivity

CHAPTER 4. CONCLUSIONS AND RECOMMENDATIONS

4.1 Strength Evaluation of the Arch Ribs

The conclusions of the strength evaluation are as follows:

1. The retrofitted test specimens were between 22% and 30% stronger in bending than the control specimens. The greater strength increase was for the arch-foundation connection specimen. The stiffness of the specimens was also slightly increased by the FRP. The retrofitted specimens lost strength after the FRP rupture or bond failure. However, they still exhibited higher strengths than the control specimens throughout the tests.
2. Structural analyses indicate that the bridge arches are much stronger than necessary to meet the required traffic loads. The retrofitting scheme increased the strength of the arches significantly. Based on the SAP2000 analysis described in Section 1.4, the strength of the arch to resist a concentrated load on the third spandrel column was increased by 30% compared to the original arch (prior to retrofit). The strength of the arch-foundation section to resist a concentrated load over the second spandrel column was increased by 32%. These increased strengths are due primarily to the transverse FRP wraps which enhance the compressive behavior of the concrete. These values come from a very simple analysis of the arch and are intended to obtain some qualitative idea of how the increased arch strengths may affect the maximum live loads on the arch.
3. The retrofitted arch specimen failed by rupture of the tension Fibrwrap. The average maximum FRP strain reached was 0.0077. This is only 63% of the ultimate strain specified by the manufacturer. In other beam tests, the rupture strain of Fibrwrap in was typically at least 0.01 (personal communication with the manufacturer, 2004). The cause of this premature rupture is unknown.

4. The retrofitted arch-foundation specimen failed due to the peeling of the concrete cover by the lower Fibrwrap in tension, which in turn led to pullout of the Leadline dowels. This peeling effect is common in FRP reinforced RC members and is due to stress concentrations at the end of the Fibrwrap (Teng et al., 2002). This caused a separation of the lower shotcrete from the rest of the specimen along the plane where the Leadline was developed. As this debonding progressed, the effective Leadline development length was shortened. Soon after the Leadline pulled out, the transverse Fibrwrap ruptured along the fracture between the shotcrete and the concrete. Increasing the amount of transverse Fibrwrap might help to prevent or delay this bond failure. However, it would probably be better to avoid terminating all of the Fibrwrap at, especially in a region of high moment. One possible solution might be to extend the Leadline rods farther into the arch and begin the longitudinal Fibrwrap at a point of lesser moment if there is such a place along the arch.

4.2 Long-Term Durability of Bond Strength between Carbon Fiber-Reinforced Polymers (FRPs) Sheets

Durability tests for investigating a long-term durability of bond strength between CFRP sheets and concrete/shotcrete under the various accelerated environment conditions were performed. The influence of environmental conditions was evaluated as a measure of pull-off strength. This information is very important for bridge design engineers, contractors and state transportation agencies for the selection, construction and maintenance of FRP materials used in FRP structures. The accelerated testing environments should be correlated with actual environmental conditions. For example, the testing environment should be created so that the number of months or years of applications of deicing salts is equivalent to a one-month period of 3% NaCl solution cyclic wetting/drying conditioning. This is not an easy task, but will be very useful for practical applications.

There are several important conclusions to be drawn from this research:

1. Pull-off test results of CFRP sheet-to-Concrete/Shotcrete under exposure to the influenced environmental parameters are satisfactory based on the recognized acceptance criterion (Minimum bond strength = 200psi). Good protection against aggressive environmental conditions is observed in CFRP composite material. However, resulting failure modes are unsatisfactory based on the ACI criterion that the ideal failure mode is to have 100% failure in substrate.
2. The corrosion inhibitor which is applied on the substrates through a standard pump sprayer does not affect pull-off bond strength.
3. For the case of concrete substrate, the most influential parameter on pull-off bond strength is "3% NaCl". The pull-off strength decreased significantly, up to 44%.
4. For the case of shotcrete substrate, the most influential parameters on bond strength are "Wet/Dry in Water". The pull-off strength decreased significantly, up to 40%.
5. Based on TG analysis, the bond strength may significantly decrease because the epoxy starts decomposing at the temperature 230 ^{o}C. Thus, for the application of CFRP sheet to use strengthening concrete structures the maximum useable temperature is 230 ^{o}C.

The bond between CFRP and substrate is critical in order to increase load carrying capacity of structures and effectiveness of strengthening systems. Construction processes such as handling, installation and curing of the material are also important parameters for strengthening/repairing concrete structures because ambient temperature, relative humidity, substrate moisture and substrate surface contamination can be affected by the adhesion.
For use in civil infrastructure applications, a FRP sheet is required with a surface treatment or addictive to enhance the fire endurance due to their potential as a fire hazard.

4.3 Wireless Real-Time Remote Structural Monitoring of the Arch Bridge

The data acquisition system, which uses wireless remote technology, performed quite well. The maximum strain was recorded up to 1400 με (0.14 %) for the service conditions. Based on the overall measurement at the arch, the temperature variation currently governs the

performance of the arch. According to the design specification, a 0.14 % of the maximum strain reached 23 % of the minimum ultimate rupture strain.
The corrosion related parameters such as resistivity, chloride level, open circuit potential and linear polarization resistance in the reinforcing steels embedded in the arch of Castlewood Canyon Bridge were monitored. The effectiveness of the corrosion inhibitor was evaluated.

The monitoring result can be misunderstood as the corrosion of the reinforcing steels is still active since the measured values are shown as the increase of corrosion. However, the increase of corrosion is not due to the increase of chloride but due to redistribution of the internal chloride. Since the internal chloride concentration of existing concrete is higher than that of the new shotcrete, the chloride will diffuse from the existing concrete to the new shotcrete, which makes the chloride level increases.

More readings are needed in the future to evaluate the long-term performance of the arch of this bridge. The monitoring process of the arch of the bridge should be continued. The results obtained so far provide valuable information and can be used to compare with the strains and the corrosion data collected in the future for evaluating the long-term performance of the arch in the Castlewood Canyon Bridge.

To evaluate long-term monitoring of corrosive conditions of reinforcement steel in concrete structures more accurately, several corrosion instruments should be installed at the overall locations of the arch.
Both the corrosion sensors and wiring of the datalogger should be red-flagged during installation to alert construction workers to the presence of the device and wires to avoid damage to the device and the wires prior to pouring concrete or shotcreting.

REFERENCES

[1] AASHTO, *Standard Specifications for Highway Bridges, LRFD, US Customary Units*, 2nd ed. (1998). American Association of State Highway and Transportation Officials, Washington D.C.

[2] Ababneh, A., Benboudjema, F., and Xi, Y., (2003) "Chloride Penetration in Nonsaturated Concrete," *Journal of Materials in Civil Engineering*, ASCE, 15, 183-191.

[3] ACI Committee 318 (2002) "*Building Code Requirements for Reinforced Concrete" (ACI 318-02),* American Concrete Institute, Farmington Hills, MI.

[4] ACI Committee 440 (1996). "State-of-the-Art Report on Fiber Reinforced Plastic (FRP) Reinforcement for Concrete Structures," ACI 440R-96, American Concrete Institute, Farmington Hills, MI.

[5] ACI 503R. (1994) "*Appendix* A: Manual of Concrete Practice," Part 5 and AS/NZS 580.408.5.

[6] Aldykiewicz, A. J. (1998) "Corrosion Measurements of Steel Reinforcement in the Kettle Creek Bridge (Rt 83), Colorado Springs, Colorado," *Grace Construction Products*.

[7] Alkhrdaji, T., Nanni, A., Chen, G., and Barker, M. (1999). "Solid RC Decks Strengthened with FRP," *Concrete International*, 21(10), 37-41.

[8] Banthia, N., Nandakumar, N., and Boyd, A. (2002). "Sprayed Fiber-Reinforced Polymers: *From Laboratory to a Real Bridge*," Concrete International, 24(11), 47-52.

[9] Beran, J. A. (1998) "Correlation of surface chloride concentration of a pile exposed to the marine environment to the adhesiveness of a commercially available epoxy," *Contract Report CR-98. 19-SHR, Naval Facilities Engineering Service Center*, Port Hueneme, California.

[10] Berke, N. S. (1987) "The Effects of Calcium Nitrite and Mix Design on the Corrosion Resistance of Steel in Concrete," *Part I: Paper #273 in Corrosion '85, Boston, 1985 Part II: Paper #132 in Corrosion '87*.

[11] Bizindavyi, L., Demers, M., Martel, S., Neale, K. W., Tadros, G. (2000). "Strengthening Reinforced Concrete Structures with Externally-Bonded Fibre Reinforced Polymers," ISIS-M05-00, ISIS Canada, Winnipeg, Manitoba.

[12] CRIEP News 356, "Development of remote monitoring system for civil engineering structures at power plants."

[13] Feliu, S., Gonzalez, J. A., and Andrade, C. (1996) "Electrochemical Methods for on-site determinations of corrosion rates of rebars," Techniques to Asses the Corrosion Activity of Steel Reinforced Concrete Structures, *ASTM STP* 1276.

[14] Grace, N. F., Roller, J. J., Navarre, F. C., Nacey, R. B., Bonus, W. (2004). "Load Testing a CFRP-Reinforced Bridge,", Concrete International, 26(7), 51-57.

[15] Hag-Elsafi, O., Kunin, J., Alampalli, S., Conway, T. (2001). "Strengthening of Route 378 Bridge Over Wynantskill Creek in New York Using FRP Laminates," Special Report 135, New York State Department of Transportation.

[16] Hayes, M. F., Bisby A., Beaudoin Y., Labossiere P. (1998) "Effects of Freeze-Thaw Action on the Bond of FRP Sheets to Concrete," *Proceedings from the First International Conference on Durability of Fiber Reinforced Polymer (FRP) Composites for Construction*, 179-190.

[17] Homam, S. M., Sheikh, S., Pernica, G., and Mukherjee, P. K., (2000) "Durability of Fiber reinforced polymers (FRP) used in concrete structures," Research Report:HS-01-00, *Department of Civil Engineering, University of Toronto*, 38-39.

[18] Jones, F. R. (1999) "Durability of Reinforced Plastics in Liquid Environments," Reinforced Plastics Durability, G. Pritchard, Ed., *Woodhead Publishing Company*, 70-110.

[19] Karbhari, V. M., Chin, J. W., and Reynaud, D. (2000a). "Critical gaps in durability data for FRP composites in civil infrastructure," *Proc., 45th Int. SAMPE Symposium*, Long Beach, Calif., 549-563.

[20] Karbhari, V. M., and Heigemier, G. A., (1996) "On the Use of Fiber Reinforced Composites for Infrastructure Renewal-A System Approach," Materials for the New Millennium, Edited by Ken P. Chong, 1091.

[21] Karbhari, V. M., Rivera, J., and Dutta, P. K. (2000b). "Effects of short-term freeze-thaw cycling on composite confined concrete," *Journal of Composite Construction*, 4(4), 191-197.

[22] Keller, T., (2003). *Use of Fibre Reinforced Polymers in Bridge Construction*, International Association for Bridge and Structural Engineering, IABSE-AIPC-IVBH, Zurich, Switzerland.

[23] Khalifa, M. A., Kuska, S. S. B., Krieger, J. (1993). "Bridges Constructed Using Fiber Reinforced Plastics," Concrete International, 15(6), 43-47.

[24] Lam, L., Teng, J. G. (2003). "Design-oriented Stress-Strain Model for FRP-confined Concrete in Rectangular Columns", Journal of Reinforced Plastics and Composites, 22(13).

[25] Mander, J. B., Priestley, M. J. N., Park, R. (1988). "Theoretical Stress-strain Model for Confined Concrete," Journal of Structural Engineering, ASCE, 114(8), 1804-1826.

[26] Mays, G. C., and Hutchinson, A. R. (1992). "Adhesives in Civil engineering, Chapter 2," *Cambridge University Press*, Cambridge, U.K.

[27] Measurement of Corrosion Rate of Steel in Concrete, *http://www.khdesign.co.uk/bgb/concrete.htm,*

[28] Mirmiran, A., Shahawy, M., Samaan, M., El Echary, H. (1998). "Effect of Column Parameters on FRP-confined Concrete," Journal of Composites for Construction, ASCE, 2(4), 175-185.

[29] Murphy, K., Zhang, S., and Karbhari, V. M. (1999) "Effects of concrete based alkaline solutions on short term response of composites," *Proceedings of the44th Int. SAMPE Symposium and Exhibition*, Society for the Advancement of Material and Process Engineering, 2222-2230.

[30] Nilson, A. H., Darwin, D., Dolan, C. W., (2004). *Design of Concrete Structures, 13th Edition*, McGraw-Hill, New York, NY.

[31] Novinson, T. (1983). "Adhesives for naval shore construction, repair and maintenance." Technical Memorandum TM 52-83-12, Naval Facilities Engineering Service Center, Port Hueneme, California.

[32] Park, R., Paulay, T., (1975). *Reinforced Concrete Structures*, John Wiley & Sons, Inc., New York, NY.

[33] Ray, J. C., Velazquez, G. I., Lamanna, A. J., Bank, L. C. (2004). "Rapidly Installed Fiber-Reinforced Polymer (FRP) Plates for Upgrade of Reinforced Concrete Bridges for the Military," ASCE Conf. Proc., 122, 359-373.

[34] Rizkalla, S., Labossiere, P. (1999). "Structural Engineering with FRP—*in Canada*," Concrete International, 21(10), 24-28.

[35] Saadatmanesh H., and Tannous F. (1997) "Durability of FRP Rebars and Tendons," Non-Metallic (FRP) Reinforcement for Concrete Structures," *Proceedings of the Third International Symposium*, 2, 147-154.

[36] Seible, F., and Karbhari, V. M. (1997). "Seismic retrofit of bridge columns using advanced composite materials," *Proc. National Seminar on Advanced Composite Materials Bridges*, Washington D.C.

[37] Shahrooz, B. M., Boy, S. (2004). "Retrofit of a Three-Span Slab Bridge with Fiber Reinforced Polymer Systems—Testing and Rating," Journal of Composites for Construction, ASCE, 8(3), 241-247.

[38] Shen, C. H., and Springer, G. S. (1976) "Moisture Absorption and Desorption in Composite Materials," *Journal of Composite Materials*, 10, 2-20.

[39] Singh R. P., Nakamura T., and Kumar B. G., *http://www.ic.sunysb.edu/stu/bgirishk/Research-QUV.htm*, Department of Mechanical Engineering at SUNY, Stony Brook.

[40] Svecova, D., Rizkalla, S., Tadros, G. (2000). "Reinforcing Concrete Structures with Fibre Reinforced Polymers," ISIS-M04-00, ISIS Canada, Winnipeg, Manitoba.

[41] Tannous F. E., and Saadatmanesh H. (1998) "Durability and Long-Term Behavior of Carbon and Aramid FRP Tendons," Fiber Composites in Infrastructure, *Proceedings of the Second International Conference on Fiber Composites in Infrastructure ICCI'98*, 2, 524-538.

[42] Teng, J. G., Chen, J. F., Smith, S. T., Lam, L. (2002). *FRP Strengthened RC Structures*, John Wiley & Sons, Ltd., Chichester, England.

[43] Toutanji, H. A., and Balaguru, P. (1999). "Effects of freeze-thaw exposure on performance of concrete columns strengthened with advanced composites," *ACI Material Journal*, 96(5), 605-610.

[44] Verghese, N. E., Hayes M., Garcia K., Carrier C., Wood J., and Lesko J. J. (1998) "Effects of Temperature Sequencing During Hygrothermal Aging of Polymers and Polymer Matrix Composites: The Reverse Thermal Effect," Fiber Composites in Infrastructure, *Proceedings of the Second International Conference on Fiber Composites in Infrastructure ICCI'98*, 2, 720-739.

[45] Virginia Technologies Inc. (2003) "Embedded Corrosion Instrument Model ECI-1; Product Manual," *Virginia Technologies.*

[46] Want, M. L., Satpathi, D., and Ren, J. Y. (1998) "Development of Wireless Health Monitoring Systems," *Proceddings of SEWC'98*, San Francisco, July, 19-23.

[47] Warren, G. E. (1998). "Waterfront repair and upgrade, advanced technology demonstration site No. 2:Pier 12, NAVSTA San Diego." Site Specific Rep. SSR-2419-SHR, Naval Facilities Engineering Service Center, Port Hueneme, California.

[48] Warren, G. E. (2000). "Pier upgrade, demonstration site No. 3-Bravo 25, NAVSTA Pearl Harbor, HI." Site Specific Rep. SSR-2567-SHR, Naval Facilities Engineering Service Center, Port Hueneme, California.

[49] White, K. R., Millor, J., and Derucher, K. N. (1992) "Bridge Maintenance Inspection and Evaluation," 2nd Edition, Marcel Dekker, Inc.

[50] Whitney, J. M. (1987) "Structural Analysis of Laminated Plates," Technical Publishing Co., Inc., Lancaster, PA.

[51] Xi, Y., (1995a) "A model for moisture capacities of composite materials: Part I Formulation," *Computational Materials Science*, 4, 65-77.

[52] Xi, Y., (1995b) "A model for moisture capacities of composite materials: Part II Application to concrete," *Computational Materials Science*., 4, 78-92.

[53] Xi, Y., and Asiz., A. (2002) "Field Investigation of Cracking in Newly Constructed Bridge Decks," *CDOT Report*.

[54] Xi, Y., Chang, S., Asiz., A., and Li, Y. (2004) "Long-term durability of fiber-reinforced polymers (FRPS) and In-situ Monitoring of FRP bridge decks at O'Fallon Park Bridge," *CDOT Report*.

[55] Zylstra, R., Shing, P. B., Xi, Y. (2001). "Evaluation of FRP Prestressed Panels/Slabs for I-225/Parker Road Project," *Report No. CDOT-DTD-R-2001-14*, Colorado Department of Transportation, December.